MICROSTRUCTURE, STRESS AND DEFECT EVOLUTION UNDER ILLUMINATION IN HYDROGENATED AMORPHOUS SILICON (*a*-Si:H)

Evariste Minani

A dissertation submitted to the Department of Physics of the University of Cape Town in partial fulfilment of the requirements for the degree of Doctor of Philosophy

University of Cape Town
May 2008

ABSTRACT

The purpose of this study is firstly to investigate the relation between microstructure, stress and hydrogen distribution in as deposited hydrogenated amorphous silicon (*a*-Si:H) layers, and secondly the investigation of the influence of illumination on hydrogen evolution and its relationship with the strain in illuminated layers.

A set of *a*-Si:H layers produced by hot wire chemical vapour deposition, at different temperatures using pure silane, was analyzed using different characterization techniques. UV-Visible absorption spectroscopy was used to investigate the bandgap, refractive index and absorption coefficient. These measurements were also used to determine the film thickness. Hydrogen in the bonded form was investigated using Fourier transform infrared spectroscopy (FTIR), while the total hydrogen was estimated with elastic recoil detection analysis (ERD). Direct diffraction patterns from synchrotron diffraction measurements, and the corresponding pair correlation function, were used to investigate the structure and the strain. To investigate the effect of illumination, a selected set of samples were illuminated for 12 and 48 hrs using a halide lamp with 110 Wm^{-2} illuminance at the sample surface.

The optical measurements combined with diffraction measurements showed that the structure of samples deposited at a temperature of 300 ^{0}C had reached an optimum for electronic and optical properties. Higher temperatures result in only slight changes to the structure, but increase the thermal mismatch stress. The bonded hydrogen concentration decreases continually with deposition temperature, but the decrease in total hydrogen saturates at high temperature. These observations suggest an increase in the relative free hydrogen concentration with deposition temperature. As the compressive extrinsic stress is increased, hydrogen is forced away from bonds into an unknown site as unbound H.

There are no clear changes in the optical properties observed after 48 hrs illumination but hydrogen was seen to migrate in samples deposited above 300 ^{0}C resulting in two clearly defined stress zones. The overall stress becomes more compressive over short illumination, and a general relaxation may be observed on long illumination

Acknowledgements

I would like to extend my sincere gratitude to my Supervisors Profs D.T. Britton and M. Härting for putting me on this project and guiding me throughout. Their long experience in research is highly appreciated and highly beneficiary. Their financial support also made my stay easier. I also would like to thank Dr Chris Theron and iThemba LABS for their financial support, and also for allowing me to perform ERDA and RBS experiments. A special thank you to Prof. Knoesen and Dr Sylvain Harindintwari (and his family) for their patience and help in the production and optical characterization of the samples used in this work. Dr Chris Arendse and Mr Miller are also acknowledged for their help. I would like to extend my gratitude to Dr Bucher and Mr Ntsoane for their help in performing the Xx-ray diffraction measurements at iThemba LABS, Dr Fabio Furlhan at LNLS in Brazil for the Synchrotron measurements. A special thank you to all members of the stress and positron groups at UCT for making my life enjoyable. Schadrack and his family are special to me for the help during my stay in Cape Town and special thank to my office mates Girma Goro and Mecit Yaman for their friendship. The last but not the least are my parents, my wife Charlotte, my son Ghislain and my daughter Joselyne for their understanding and patience during this long period far from them.

TABLE OF CONTENTS

I. INTRODUCTION

1. INTRODUCTION

The work presented in this thesis is focussed on hydrogenated amorphous silicon which is a widely used thin film semiconductor material [1]. The degradation of its optical and electrical properties when exposed to intense light is a major factor limiting the wider use of this material. Over the last three decades, progress has been made in understanding and improving the electronic and optical properties of this material, but the mechanisms of light induced degradation are still incompletely understood. The main objective of this study was the investigation of the interdependence of microstructure, stress and defects, and their evolution under illumination.

The structure of *a*-Si:H is thought to consist of a continuous random network (CRN) with slight changes in the bond length and the bond angle. This structure is highly strained and the most common types of defects expected in this material are broken bonds, which may be terminated by hydrogen. Incorporation of hydrogen into the network structure, therefore, leads to both a passivation of electronically and optically active defects, and a local structural reconfiguration. In the latter case, it may act as either a source of intrinsic stress or as a cause of a stress relaxation mechanism. The role played by hydrogen in shaping the structure and therefore the stress, and other properties of the *a*-Si:H is therefore an important area of study.

The *a*-Si:H samples used in this study were deposited simultaneously on both crystalline silicon (*c*-Si) and Corning glass substrates, at different temperatures, between 150 and 500 ^{0}C using hot wire chemical vapour deposition with pure silane as reactive gas. The optical parameters, band gap, refractive index and absorption coefficient were estimated using UV-Visible absorption spectroscopy. Bonded hydrogen content, and its configuration, in the layers were analysed using Fourier transform infrared spectroscopy, and the total hydrogen concentration was estimated by ion beam analysis. The structure and the stress were investigated using synchrotron radiation diffraction on a selected set of samples. These results were analysed in two approaches using both the direct diffraction patterns, and the pair correlation function after being Fourier transformed.

To investigate the influence of illumination, the selected set of samples was illuminated for periods of 12 and 48 hrs at an intensity of 110 Wm^{-2}. The changes in stress,

hydrogen content and bonding and optical properties were monitored using the above mentioned techniques.

This thesis is divided into six major sections. A brief introduction is followed by section II which is the general background to the study. This section comprises four chapters, of which the first is dedicated to the structure of amorphous solids. This chapter gives a brief description of the structure and structure of defects in *a*-Si:H. The role of hydrogen in passivating dangling bonds and also its contribution in defect formation during light soaking are highlighted. The second chapter discusses the mechanism of layer growth and local relaxation in the amorphous network. In this chapter, the production of silicon radicals and how they contribute to the growth of the layer is discussed. The formation of the network strain and its relaxation are also briefly introduced. Chapter three in this section discusses the microstructural changes under the influence of external influences such as light, and finally in the fourth chapter strain and stress are discussed in the framework of the theory of elasticity. In this chapter an introduction to residual stress in layered systems in general, and *a*-Si:H in particular, is presented.

The third section details the experimental techniques used in this study and comprises three chapters. Each chapter is presented independently, and comprises a background to the material, followed by discussion of the experimental methods, analysis and results. The first chapter first present the technical details about the hot wire CVD process and goes on to describe how the samples were produced. This is followed by a chapter on diffraction and stress determination in amorphous silicon using diffraction methods. Diffraction measurements and stress determination in amorphous materials are explained, and the results presented. The final chapter concern optical and chemical characterisation of the material. In this chapter, the spectroscopic and ion beam techniques used to investigate optical parameters, and hydrogen content and bonding are discussed and the results presented.

Because the main object of this study is the interdependence of microstructure, stress and defects, and their evolution on illumination, section four provides a consolidated discussion of all the results from the different characterisation techniques used in the study. This is divided into two chapters, discussing the mutual relationship between the intrinsic stress and the hydrogen related defects in as deposited material, and the evolution

characteristics under illumination, respectively. In the fifth section a general conclusion is presented together with perspectives of further work pertaining to this subject, and the sixth and final section comprises the appendices with experimental data.

II. GENERAL BACKGROUND

1. STRUCTURE OF AMORPHOUS SOLIDS

All solid materials are formed from discrete basic units, which may be atoms, molecules or ions. In the following discussion, because silicon is a covalently bonded atomic solid, the basic unit will be referred to as atom. In an ideal crystalline solid the positions of the atoms are exactly periodic. The crystal possesses translational symmetry, with a finite unit cell which repeats itself infinitely in three dimensions [2]. In contrast, in an amorphous material, atoms are distributed randomly, and therefore the structure lacks the periodicity and symmetry observed in crystalline solids [3]. At first sight it appears quite absurd to discuss the structure of amorphous materials, particularly when comparing with a crystalline solid, where the specification of the positions of relatively few atoms within the unit cell is sufficient to describe the structure completely. However, the structure of amorphous solids can be described in terms of the degree of order [1]. Conventionally, structural order is divided into three length scales: short range (SRO); medium or intermediate range order (MRO); and long range order (LRO) [4]. The definition of these three length scales is debated, with different authors using different criteria to define them [5]. Of the three, the MRO is the most difficult to define precisely [6,7].

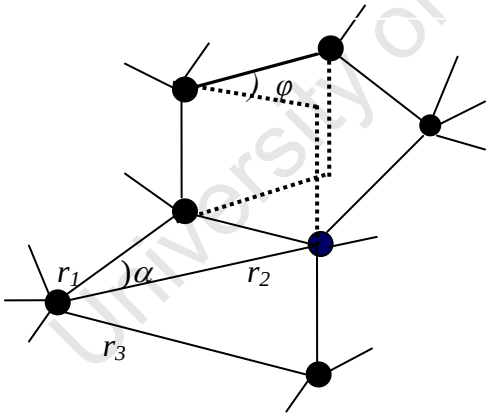

Fig.1: Schematic illustration of the geometrical parameters used to define structural order in tetrahedral amorphous solids: r_1, r_2 and r_3 are the first, second and third nearest neighbour distances, α the bond angle and φ the dihedral angle [1].

In the case of tetrahedrally bonded amorphous solids, five geometrical parameters are conventionally used to define the hierarchy of the structural order, as shown in the figure 1. Short range order (SRO) describes the basic structural unit and the interconnectivity of adjacent structural units. It is therefore defined by the coordination

number, the inter-atomic distance between nearest neighbours r_1, and bond angle α, which also implicitly associates the distance between the second nearest neighbours r_2 [4]. Within this definition, SRO covers distances of the order of 2-3 Å. The MRO takes into account the statistical distribution of the dihedral angle φ between two adjacent structural units, and the third neighbour separation r_3. Finally the long range structure takes into account density fluctuations associated with structural inhomogeneity at a large scale, due to the presence of voids, vacancies or foreign impurities in the structure, and also that the structure may not be completely random [8].

In a more sophiscated way, the short range structural order in an amorphous solid can be represented by a set of pair correlation functions. The pair correlation function $g\left(\vec{r}\right)$ is the relative probability of finding two atoms, each of a particular type, separated by a vector $\vec{r}$. In the case of an isotropic solid, composed only of one type of atom, the pair correlation function reduces to the radial distribution function (RDF)[3]. This function gives the relative probability of an atom being found at a given distance from a reference atom. However, in the literature, the terms pair correlation function and radial distribution function are often used as synonyms.

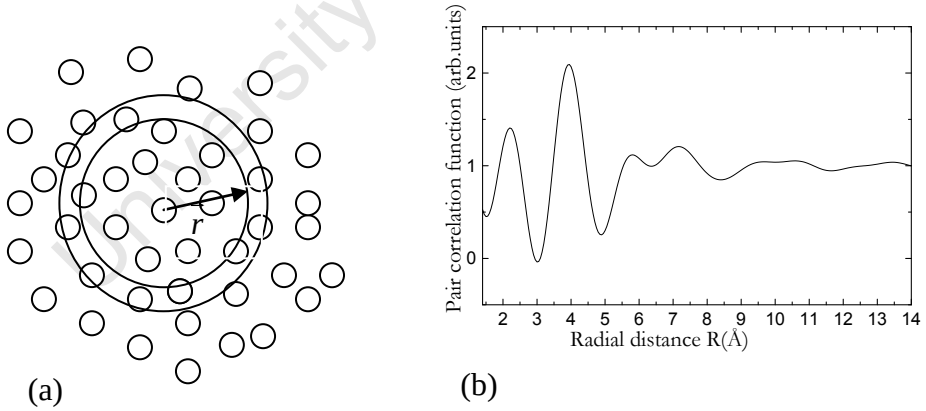

Fig. 2: Schematic illustration of (a) the structural origin of certain features in (b) the radial distribution function for an amorphous solid.

The definition of the RDF is illustrated in figure 2. As shown in fig. 2(a), the number of atoms in spherical shell of radius *r* and the thickness *dr* is counted. After normalizing to the volume of the shell, $4\pi r^2 dr$, a curve like that shown in fig.2(b) is obtained. This curve shows clearly regions of high density, corresponding to preferred interatomic separations.

For very large radii, the distribution of atoms in the shell is effectively continuous, and the RDF approaches the macroscopic atomic density of the solid.

The importance of the radial distribution analysis lies in the fact that samples prepared in almost the same conditions may show differences in the radial distribution function, and thus small details in the structure can be identified [9]. However, it is a one-dimensional representation of three-dimensional structure and can therefore only carry a limited amount of structural information, even if isotropy and homogeneity are assumed. The characteristic features of the pair correlation function are the number and the shape of the peaks observed. The positions of the peaks correspond to the first, second, and even to the third nearest neighbour distances in a particular direction. The width of the peak is an indication on how the bond length and the bond angle fluctuate within the material. From the estimated first and second neighbour distances, r_1 and r_2, the average bond angle α can be estimated using the following equation

$$\alpha = 2\arcsin\left(\frac{r_2}{2r_1}\right). \tag{1.1}$$

The area under the peak gives the number of atoms within the shell, and therefore, for the first peak, the coordination number. It can also be noted that at a large distance the RDF tends to a constant value equal to the macroscopic density.

1.1 Structure of *a*-Si:H

The atomic structure of hydrogenated amorphous silicon has been investigated by many authors by different means ranging from X-ray [9], electron [10] and neutron [11] diffraction. It has been shown that the first peak of the radial distribution function almost coincides with that of crystalline silicon [9], although slight elongation (1%) can be detected. The area under the first peak was found to be the same for amorphous and crystalline silicon. The second peak, which gives the number of second neighbours, is broadened in the case of amorphous silicon, and this is accounted for by the variation of the bond angle. Two factors complicate the structural determination. Firstly *a*-Si:H is a binary system, and hence requires three partial pair correlation functions (Si-Si, Si-H, H-H) to fully describe the system [4]. The situation is made even worse because, of the three main scattering techniques, only neutron diffraction is sensitive to the presence of hydrogen [12]. However, compared to the typical

thickness of real *a*-Si:H layers, neutron diffraction requires very large scattering volumes. Generally those difficulties are ignored by considering the fact that the H concentration is generally around 10% in *a*-Si:H, and therefore assuming that it does not contribute significantly to the observed diffraction data. The second factor is that a real *a*-Si:H sample is not homogeneous, either because of the presence of different phases or structural defects such as voids, internal cracks or doping impurities [8]. The bond angle fluctuations and the bond length variations deduced from experimental RDFs are expected to arise from a variety of causes including: the overall non-crystallinity of the structure; the effect of incorporation of hydrogen or other impurities; the presence of microscopic defects, namely dangling bonds; and the presence of large scale inhomogeneities such as voids, and vacancies. For the purpose of describing the basic structure, however, the overall non-crystallinity can be assumed to have the most influence.

Different structural models have been developed to fulfil the features observed in the experimental radial distribution functions of *a*-Si:H. One early model was a microcrystalline model [13], which presented amorphous silicon as composed of micro-crystallites. However, the density of dangling bonds in the model was higher than that observed [8]. An improved structural model, based on a structural unit of a dodecahedron, was proposed by Grigorovici [14]. This model accounts for the RDF better than the microcrystalline model, but also yields a bond angle of 108^0 which is substantially different from the 109^0 28' observed for tetrahedrally coordinated amorphous materials [8]. A continuous random network (CRN), first proposed by Zachariasen [15], for oxide type glasses, was extended by Polk [16] to amorphous silicon. This model accounts for the RDF better than all the previous models. In this model, a silicon atom has four others around it forming a tetrahedron, but although the number of atoms associated with the nearest neighbour is the same, there is a slight variation in the bond length and interbond angles, of 1 and 10% respectively. This leads to a rapid loss of the local order, and ultimately to the absence of long range order. The dihedral angles are also chosen for distortion by bond angle and bond length to be as small as possible.

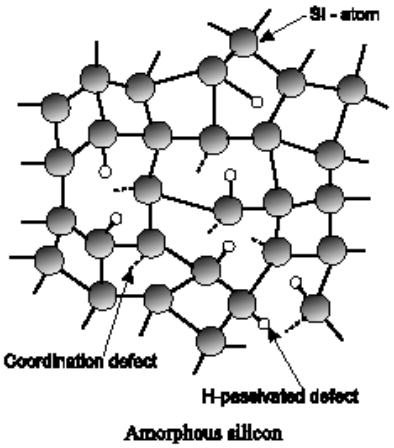

Fig. 3: Schematic illustration of the network structure of hydrogenated amorphous silicon showing coordination defects.

1.2 Defects in hydrogenated amorphous silicon

Defects in *a*-Si:H present one of the controversial aspects for this kind of material, starting with the definition of a defect. Due to the regular periodicity and translational symmetry with respect to atomic arrangement, a defect in a crystalline material can be defined as the absence of an atom from a regular lattice point (vacancy), or an atom which is at a position off the regular lattice (interstitial atom) [17]. If such a definition is applied in an amorphous material, all of the atoms will represent defects. In an amorphous system, which lacks the long range periodicity, the relative position of atoms only has a meaning in terms of a statistical distribution. Thus, in covalently bonded amorphous solid, a structural defect is defined as an anomaly in the covalent bonding in relation to the short-range order [4].

This approach immediately leads to the concept of coordination defects, illustrated in figure 3. Under-coordinated defects, known as dangling bonds, are the typical examples of defects in tetrahedraly bonded amorphous materials [18]. Understanding fully their relation with the growth mechanism [19], and the sample metastability after a prolonged illumination [20], has been, and still is, a challenge to physicists. Dangling bond defects in *a*-Si:H may appear in one of the three different charge states. They can be positively charged, neutral or negatively charged when they are unoccupied, singly, or doubly occupied by electrons. Dangling bond defects in the *a*-Si:H network therefore operate as charge recombination centres and affect the electrical properties of the material [21].

The mechanism of dangling bond formation and distribution in *a*-Si:H is thought to be mediated by hydrogen. This is because dangling bonds result from the breaking of weak Si-Si bonds, but it has been noticed that if the two dangling bonds are allowed to stay close to each other a different defect density will be measured compared to the situation where they are allowed to diffuse apart [22]. The diffusion of hydrogen will allow the dangling bond defect to occupy the Si-H site from which the hydrogen was removed. This effect is confirmed by the observation of hydrogen motion at the same temperature as the recovery of the metastable defects, or by considering the activation energy of defect annealing which is comparable to that of hydrogen diffusion [23]. However, the relationship between dangling bond concentration and hydrogen content, or bonding, in the *a*-Si:H network is not straightforward. The assumption that the higher the hydrogen concentration, then the lower the defect density, may not hold if there is insufficient structural relaxation of the network as a result of lower deposition temperature [24].

Over-coordinated defects are less common, and may arise when an additional covalent bond is formed between a normally coordinated atom and another. This type of defect in *a*-Si:H has been proposed as the interstitial hydrogen interacting with weak Si-Si bonds [25]. By extending the definition of defects as anomalies in structural bonding other types of defects can also be mentioned. These are weak Si-Si bonds with a bond length greater than the normal Si-Si bond, and a three-centred bond for the case where a hydrogen atom is bound to two Si atoms.

Atomic vacancies are another form of defect which occur in hydrogenated amorphous silicon. They are responsible for many of the electrical and optical properties of such material [18]. Vacancies can be thermally generated, but are also created by irradiation damage processes, such as displacement damage when an incident particle of radiation has sufficient energy to displace an atom of silicon [26]. Defects can also be created by electronic rearrangement when radiation causes an electronic excitation [17]. In this case electrons or holes resulting from the excitation can either be trapped at pre-existing defects, or can cause bonds to break, thereby creating neutral dangling bonds. Atomic vacancies may occur either singly, as monovacancies, or as divacancies and clusters. They are, after the single dangling bond defects, the most simple form of structural defects likely to be found in a-Si:H [1].

Density defects range from voids, which may be regarded as aggregates of a variable number of vacancies [1], to fluctuation in density (or free volume) which may be regarded as vacancies which have become distributed throughout the material [17], and which therefore cannot be regarded any more as well-defined point defects. The presence of such defects influences, to a great extent, the physical properties of the material because of the dangling bonds expected at the void surface [18]. Although annealing the samples to elevated temperatures reduces the void concentration to a certain extent, they cannot be removed entirely before the crystallization temperature is reached [1].

Impurity atoms, incorporated as uninvited guests during the deposition, or, in the case of boron or phosphorous by deliberately doping, constitute another form of defect in the *a*-Si:H network. The uninvited impurity atoms include oxygen, nitrogen and carbon, and their concentration may range between 10^{18}-10^{20}cm^{-3}[1]. A study by Carlson [27] suggested that oxygen may be admitted either from the walls of the vacuum chamber, in the form of H_2O, CO or CO_2, or as a contaminant of the silane source gas in the form of $(SiH_3)_2O$. Nitrogen may come from the leakage of air into the vacuum chamber, release from the chamber wall, or as a contaminant in the silane gas. Carbon may be introduced as CO or CO_2 in the exhaust gas, or as back-diffused hydrocarbons, from the vacuum pumps.

The concentration of dangling bonds increases after a prolonged exposure of the sample to light [28]. The breaking of weak Si-Si bonds by prolonged illumination seems to be the major mechanism for light induced defect creation in *a*-Si:H. The energy required to break the Si-H bond of about 3.5eV can only be achieved when undoped a-Si:H is bombarded with energetic particles, or when the material is annealed at temperature above 400^{o}C [29] The bond breaking is thought to be triggered by non-radiative recombination of electrons with holes trapped at such a weak Si-Si bond [30]. But there is also a model in which the threefold-coordination silicon centres, with negative correlation energy, may capture an electron or a hole to form a neutral dangling bond under optical excitation [31]. The dangling bond defects created on illumination are stable at room temperature and disappear on low energy annealing of the sample at temperatures as low as 200^{0}C [20].

Different experimental methods have been used to obtain information about structural defects. Among them positron annihilation spectroscopy [32] gives information

about the nature and concentration of defects. Electron spin resonance (ESR) [33] provides the most detailed information concerning the local bonding structure of defects. The energy position of defect levels in the band gap region is estimated from spectroscopic means. Optical spectroscopy such as photo-induced absorption [34] and photo-thermal deflection spectroscopy [35] measure optical transition energies, namely the depths of defect levels.

The annealing behaviour of the defect structure in hydrogenated amorphous silicon produced by hot wire chemical vapour deposition has been studied by pulsed and conventional positron beam techniques combined with X-ray diffraction [9]. An annealing stage, below the growth temperature, was found to lead to an increase in open volume. This was related to a redistribution of hydrogen in the sample and its escape from it [9]. The importance of defects in *a*-Si:H lies in the fact that many properties of amorphous material can be defect controlled. In many cases the behaviour resulting from the presence of defects can completely dominate that due to the intrinsic material.

To summarize this section, we can see that the thermal history and hydrogen concentration must be regarded as the main conditions which determine the intrinsic defect concentration in *a*-Si:H. These are also the same conditions influencing the structural relaxation on the sample surface during its deposition. Prolonged illumination introduces additional defects. It must also be noted, that not all the proposed types of defects have been demonstrated experimentally, but are only proposed for the purpose of understanding the localized levels within the band gap. In the light of the important role played by hydrogen in shaping the structure, and therefore the properties of *a*-Si:H, a full understanding of the role played by hydrogen in *a*-Si:H is discussed in the next section.

1.3 Hydrogen in hydrogenated amorphous silicon

Numerous studies have highlighted the important role of incorporated hydrogen in the amorphous network [1], and its importance in the growth mechanism [18] of good quality a-Si:H samples. Hydrogen incorporated into amorphous samples reduces the number of defects, but at the same time depletion of hydrogen from the silane plasma during the deposition process leads to an increase in the concentration of defects in the sample

produced [36]. Hydrogen is also believed to play an important role in the Staebler Wronski effect (SWE) [37], which is characterized by an increase in the concentration of the defects levels in the band gap after prolonged illumination. These defects act as recombination centres that degrade the electro-optical properties of *a*-Si:H, and can be annealed out at temperatures above 180^0C. Due to its importance, different investigations have been carried out on how hydrogen is incorporated in the amorphous network. Particular concerns are in which configuration it is present, the content required in a good quality sample, and how it can be related to the *a*-Si:H growth mechanism, defect density and metastability.

Hydrogen is present in *a*-Si:H in different forms, either as atomically dispersed and bonded to Si atoms in monohydride, di- or trihydride configurations or their complexes, or also in the form of isolated hydrogen molecules. The hydrogen content, bonding and configuration can easily be investigated from infrared absorption measurements, electron spin resonance, nuclear magnetic resonance, and ion beam analysis [6]. Layers with only monohydride bonding have been observed to contain NMR isolated and clustered H bonding [38]. As the dominant defects in *a*-Si:H are dangling bonds, which are present in neutral or charged form, hydrogen, with its possibility to diffuse over a long distance in the sample, will passivate these deep traps. By doing so the hydrogen will terminate the broken bonds, allowing the network structure to relax. Hydrogen in silicon is assumed to diffuse as unbonded atomic hydrogen, that may be present in neutral or positively charged form, but the work by Corbett *et al.* [39] suggest that, between room temperature and 600 °C, the atomic hydrogen may form interstitially dissolved, and essentially immobile, H_2 molecules.

The important role of hydrogen during the deposition of *a*-Si:H was also recognized by numerous authors [40,41]. Furthermore, high intrinsic compressive stress observed in *a*-Si:H has been associated with the incorporation of hydrogen into the amorphous matrix [42]. Although no correlation has been established between the total hydrogen in the sample and the magnitude of the compressive stress, it is generally accepted that the hydrogen bonding to silicon atoms plays a significant role. A correlation has been established between hydrogen atoms in the monohydride configuration and high compressive stress, while atoms in the dihydride configuration are associated with a tensile stress [43]. It must be noted that the hydrogen is not the primary or the sole cause of stress in *a*-Si:H. As is discussed in chapter 4 below, structural inhomogeneities such as voids, vacancies and dislocations are suggested to play a dominant role [44].

To summarize, the effect of atomic hydrogen in *a*-Si:H is at least three fold including: controlling the surface process during the growth of *a*-Si:H layer, directly eliminating the number of dangling bond defects and therefore relaxing the Si-Si network, and finally acting as an alloy, and hence affecting the network order and correspondingly modifying the electronic properties such as the band gap. Although our knowledge of the role-played by hydrogen in amorphous silicon has been improved, the complexity of its role is still not fully understood. Questions such as how hydrogen content, or bonding, in *a*-Si:H are related to the light induced metastability, or which growth mechanism can explain, in detail, the surface hydrogen removal during the deposition process, remain. Also further investigations are needed in order to correlate the high compressive stress observed in *a*-Si:H to its hydrogen content or bonding configuration.

2. LAYER GROWTH AND LOCAL RELAXATION IN THE *a*-Si:H NETWORK

Hydrogenated amorphous silicon is fabricated using various forms of chemical vapour deposition (CVD) techniques [45]. All these techniques use different processes to crack monosilane or similar reaction gases, such as chlorosilane or disilane [18], to produce the reactive SiH_x radicals which recombine at the growth surface to produce bulk silicon. Because the deposition process is far from the equilibrium conditions, the material produced freezes in an amorphous, metastable state [1]. All CVD processes are broadly similar with the main differences being the method used to crack the gas, and consequently the populations of different radicals impinging the growth surface. The dominant technique used for depositing *a*-Si:H is plasma enhanced chemical vapour deposition (PECVD), which has been established for industrial applications [18]. Other techniques are photo-assisted CVD, electrochemical vapour deposition, metallorganic CVD (MOCVD), and pulsed injection MOCVD. Recently hot wire chemical vapour deposition (HWCVD) has gained considerable attention as an alternative deposition method as it proved higher deposition rates and improved film stability for device quality material [45]. The following discussion will focus on hot wire CVD because it was the technique used to produce the samples in this study. This chapter will discuss how the radicals contributing to the growth of *a*-Si:H are produced and the growth mechanism of the *a*-Si:H layer on a heated substrate. Due to the non-equilibrium deposition conditions the network structure of the layer produced is always strained. The strain formation and relaxation in *a*-Si:H will be discussed and related to the growth conditions.

2.1 Production of Silicon Radicals in HWCVD

Hot wire CVD, also known as catalytic chemical vapour deposition (cat-CVD), is a relatively recently developed low temperature deposition technique which is based on the dissociation of a gas mixture at the surface of a resistively heated hot filament (tungsten or tantalum heated to 1500-2200^{o}C) at a low pressure of 10^{-3} to 10^{-1}mbar. These conditions lead to the cracking of gas molecules, and with the heated catalyser usually placed near the substrate, the ionized radicals in the plasma will freeze in contact with a relatively cold substrate.

The HWCVD technique has attracted attention because of the possibility of producing a low concentration of H in the *a*-Si:H alloys, with a view towards reducing or eliminating the instability in the material [46], as well as the possibility of obtaining a high deposition rate, and low temperature fabrication of polycrystalline silicon [47]. Furthermore, with HWCVD there are no effects of plasma damage or charge induced damage seen in various PECVD devices [48]. Also it allows a flexible range of substrate temperatures, and therefore allows an easy control of the production of unknown higher order silane radicals [49], whose gas phase reactions generally lead to the incorporation of undesirable excess hydrogen in the films.

The concept of using a catalytic reaction, by inserting a catalyst into a conventional thermal CVD system, to reduce the deposition temperature and increase the film quality was first proposed by Yamazaki [1] in 1968. Eleven years later, Wiesmann *et al.* [50] reported producing silicon films from a SiH_4 gas using heated W or C rods. However, because of the poor quality of the samples produced, due to the poor vacuum used, this work did not attract much attention. At that time it was thought that the SiH_4 gas was decomposed by a thermal reaction at the surface of the wire. It was 1985 when Matsumura *et al.* [51] reported to have succeeded in producing high quality hydrofluorinated amorphous silicon (*a*-Si:F:H) using silicon difluoride (SiF_2) and H_2 as gas precursors. They explained that the reaction of the gas mixture with the heated filament was catalytic in nature, and named the method catalytic CVD (cat-CVD). In 1986 [52], they went on to produce device quality *a*-Si, using only SiH_4 source gas and a heated W wire, by adjusting the deposition parameters. In 1988, Doyle *et al.* [53] produced high quality *a*-Si:H, using slightly different deposition conditions than those used by Matsumura. They termed the process "evaporative surface decomposition" (ESD) because of the highly efficient dissociation of the low pressure feed gas and the large flux of deposition radicals. The same process was later renamed hot wire assisted CVD because of uncertainty over whether the reaction at the filament surface was catalytic or not. In 1991, Mahan *et al.* [46] reported a comparison between sets of samples produced with cat-CVD and PECVD techniques, and demonstrated the superiority of cat-CVD to PECVD for producing *a*-Si:H. Since they used the term hot wire CVD (HWCVD) in their report, the technique is now also widely known by this name.

In hot wire CVD, the reaction gas (usually SiH_4) undergoes pyrolysis to form precursors at the surface of the heated filament. Ideally, the gas will be completely cracked to its constituents Si and H. All SiH_4 molecules introduced into the chamber collide with the catalyser within the residence time, and the probability that a molecule will be decomposed by one collision was established be at around 40% [54]. Depending on the temperature of the wire, different reactions were observed [55]. At room temperature the silane molecule is dissociatively adsorbed onto the surface of the metal to form SiH_3 and H radicals. When the temperature is elevated to between 600-1000^{0}C, the major decomposition configuration becomes SiH_2 and 2H, as in the case of thermal CVD [40]. When the temperature increases further, the SiH_4 is adsorbed on W or Ta in the form of Si and 4H. However, because of the high temperature, the thermal desorption rate of Si atoms from a W-Si or Ta-Si bonds becomes faster than the growth rate of W or Ta silicide. The important factors in this step are the filament temperature and the total pressure.

The gas phase reactions of the generated radicals, to form other species (SiH_x), depend on the pressure of reaction gas, and the distance between the filament and the substrate. The possible secondary radicals formed were identified as follows [56]:

$$H+SiH_4 \longrightarrow SiH_3+H_2$$
$$H+SiH_3 \longrightarrow SiH_2+H_2$$
$$SiH_3+SiH_3 \longrightarrow SiH_4+SiH_2 \quad .$$
$$Si+SiH_4 \longrightarrow Si_2H_2+H_2$$
$$Si_2H_2+SiH_4 \longrightarrow Si_3H_4+H_2$$

Depending on the deposition conditions all these radicals will contribute, in one way or another, to the growth of the amorphous silicon layer.

2.2 Growth Mechanism

The deposition of *a*-Si:H samples using HWCVD appears quite simple in principle, but the physical and chemical processes involved are extremely complex, making it difficult to identify the dominant reaction path responsible for the growth from the many possibilities. It is widely accepted in all growth models that the SiH_3 radicals are the dominant radical in *a*-Si:H growth. However, a recent paper by Zheng and Gallagher [57] suggested that the SiH_2 is now the primary depositing radical under optimum condition.

The importance of other radicals, assumed to play a minor role, cannot therefore be excluded as they may determine important film properties.

Different models have been developed to describe the growth process of hydrogenated amorphous silicon, but two of them have proved to be more consistent with experimental findings. These are the thermodynamical approach and the kinetic model. Initiated by the work of Winer [58] and Street [59], the thermodynamical approach can help to explain the defect concentration, and other properties of the amorphous layer, using hydrogen equilibration as a function of the deposition parameters such as the deposition temperature and growth rate. Within this model, the formation of a dangling bond results from the breaking of a weak Si-Si bond in the bulk by mobile hydrogen that is released from a Si-H bond [40] as shown in figure 4.

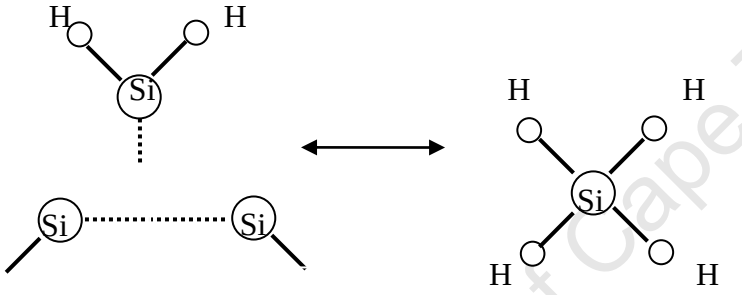

Fig 4: Illustration of the dangling bond formation in a-Si:H in the thermodynamical approach of Winer [58] and Street [59].

In this model, the defect density is a result of the thermal equilibrium between the mobile hydrogen diffusion and the incorporation of the weak Si-Si bonds. The weakness of this model resides in the fact that it does not explain how the surface chemical reactions leading to the growth of the layer actually take place. The effect of the deposition temperature is associated with the hydrogen diffusion acting as a mediator in the reactions, which convert weak bonds in the subsurface region into strong bonds. At a higher substrate temperature, H diffusion is very fast and can redistribute between alternative bonding sites and equilibrate the Si-Si and Si-H bonds and thereby minimize the concentration of weak bonds and consequently the dangling bonds. This model was improved by Yamasaki *et al.* [60.], with the mobile hydrogen becoming also responsible for the creation and passivation of dangling bonds at the surface and in the bulk.

The kinetic model was developed by Matsuda, Gallagher, Perrin *et al.* [61,62,63], and is based upon the assumption that the dangling bond is the growth site. The SiH_3, assumed to be the dominant growth precursor, is weakly absorbed at the hydrogen passivated surface in a three centred Si-H-Si bond (physisorbed state). As illustrated in figure 5, since the radical is weakly bonded it can diffuse very quickly over the hydrogen-passivated surface and increase its possibility of finding a dangling bond. To conserve the continuous growth, new dangling bonds are created by H abstraction by SiH_3 or another gas phase radical in a so called Kisliuk or Eley-Rideal mechanism [40]. However, the direct insertion of silyl (SiH_2) radicals into strained Si-Si bonds without removing any surface hydrogen can explain the low dangling bond density at the surface. This growth step does not require the creation of a dangling bond.

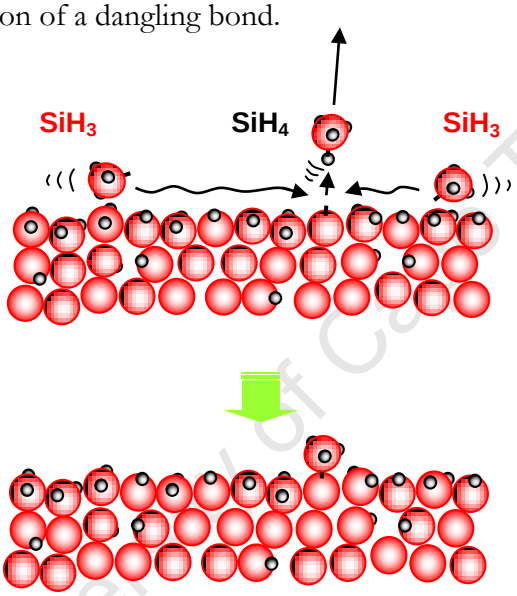

Fig.5: Schematic sketch for the surface growth process [64].

In all models, as well as in the real growth situation, the key factor is the substrate temperature [65]. The surface rearrangement reaction of useful radicals to incorporate the adsorbed radial in the film and release of hydrogen is highly dependent to the substrate temperature. The substrate temperature determines the surface mobility of these radical and increases the diffusion of hydrogen.

The growth surface was reported to be fully passivated by hydrogen [41] but an important question was also raised on how this hydrogen was removed leaving only around 10% in the layer. Different models of hydrogen removal were suggested, among them the

breaking of a Si-H bond followed by a recombination of the dangling bonds into a Si-Si bond [66]. This mechanism was immediately refuted, as the probability for a dangling bond to find another dangling bond at the sample surface during the deposition process is minimal compared to the abstraction or passivation reactions of radicals with the reacting plasma described above. Thermal desorption of hydrogen from the sample surface [67] was also considered, where a Si-Si bond, followed by the emission of a H_2 molecule, is formed from the bond breaking of two neighbouring Si-H bonds. This reaction is, however, not activated at normal deposition temperatures below 450^0C. Hydrogen removal by so-called cross linking [66], occurring directly after the chemisorption of a SiH_3 radical was able to explain the reduced hydrogen in the bulk, but several questions were not answered as to why hydrogen is randomly distributed in the sample and not in small clusters.

The use of high hydrogen diluted silane plasma can also lead to the deposition of microcrystalline (*μc*-Si:H) silicon [64] but the mechanism behind this is not fully understood. It is suggested that the extra atomic hydrogen at the sample surface could possibly induce the crystalline growth [68].

For low temperature growth, particularly at higher gas pressures, another growth mechanism is the charged cluster model [69]. The charged cluster model, which was suggested as growth mechanism of CVD diamond, could, in general, explain the growth mechanism in many thin films. In this model, nanometre size clusters formed, presumably by ion or photo induced nucleation in the gas phase, are the deposited units.

2.3 Network Strain and Relaxation

As discussed in the previous section *a*-Si:H materials are produced in non-equilibrium conditions. The structure of *a*-Si:H is best described by the CRN structure, where distortions in the bond length and bond angle are introduced to account for the experimental RDF. It was also noted that the main defects are dangling bonds. The major source of local microscopic strain is therefore the network and defect structure resulting from the non equilibrium growth conditions associated with various deposition techniques. These conditions may lead to density variations, formation of voids, gas incorporation during the deposition, or recrystallisation of the amorphous phases and oxidation of

porous samples after deposition. All these aspects of the microstructure which influence the stress are highly dependent on the details of the deposition process.

Distortions in the bond length and bond angle create relatively highly strained Si-Si bonds as atoms are moved from their minimum energy equilibrium position. These weak bonds may get broken by a hydrogen atom in their vicinity, or by incorporation of an impurity atom while doping or from the environment in post-deposition oxidation [70]. This contributes to the relaxation of the network strain.

In *a*-Si:H the strain in the sample is also attributed to the presence of defects. Knights [71] has associated the tensile stress in the samples to the presence of voids. Films which are rich in voids were observed to exhibit a tensile stress, as the voids allow contraction of the film as far as energetically possible. Spear [72] associated an observed compressive stress to the invasive incorporation of impurities such oxygen, nitrogen, argon, and for *a*-Si:H it was attributed to the incorporation of hydrogen.

Nevertheless, the role played by hydrogen in determining the strain in *a*-Si:H is still debatable. Although it has been reported that increasing the hydrogen concentration in the sample tends to increase the compressive stress, there is an intriguing question on how such a relatively small hydrogen range can account for the large variation in the stress observed. It must also be noted that it has been difficult to isolate the contribution from the hydrogen and the contribution from the film structure and bonding, which determine the strain in the film. This is in agreement with the work reported in [73], which suggested that the amount of hydrogen atoms in a monohydride (Si-H) configuration has a positive correlation with compressive stress, and that in a dihidride ($Si-H_2$) bonding configuration, it has an opposite correlation.

However, Marques *et al.* [74] have found that the main contribution to the stress comes from unbound hydrogen. They explain that this type of hydrogen is interstitial or is inside small voids. The authors further suggest that it exerts a pressure on the void wall resulting in increased volume of the film, and thus a compressive stress is developed. However, according to established theory [75], such situation would only result in a shear stress, unless the increase in layer volume was otherwise constrained, *e.g.* by the substrate. In a very defective film, with a large number of voids the pressure is less effective and the

electrostatic attraction is thought to dominate [74], which may lead to a tensile stress in the sample. There is no relationship established yet between hydrogen and the stress in the sample, but samples with high porosity and therefore less concentration of non-bonded hydrogen show a tensile, or lower compressive, strain with the tensile contribution coming from the surface tension of the voids. The decrease in tensile stress may result from the improved structure which keeps the hydrogen pressure. Therefore, high density homogeneous material should show high compressive stress, associated with a densification of the structure [74]. This is supported by the sharp change in the stress observed at the onset of columnar growth [76].

From the above description it can be seen that the intrinsic strain in *a*-Si:H films is generally correlated to the structural properties and hydrogen concentration in the sample. In the case of *a*-Si:H, intrinsic stresses are related to the presence of defects [49] and part of the strain in the CRN is relaxed by hydrogen termination of dangling bonds. But, as discussed in chapter II.3.1, this hydrogen related defects are also responsible for the subsequent degradation of the material upon exposure to intense light. This degradation is associated with changes in microstructure because of hydrogen evolution within the sample (diffusing and probably escaping from the sample). Therefore there will be changes in the network strain. Nonomura *et al.* [77] have reported light induced changes in *a*-Si:H which resemble the light induced volume changes normalized to the initial volume. Furthermore, changes in hydrogen content and bonding may affect the already inhomogeneous distribution of hydrogen in the sample and changes in domain boundaries. The extreme case being light induced crystallization. Other changes in microstructure may come from oxidation after the deposition. Thermal cycling and electrical bias also have a contributing effect to the degradation processes.

To summarize this chapter, it was discussed how the understanding of quite complex growth process of a-Si:H material is of paramount importance in producing high quality and reliable devices. The microscopic strain formation and therefore the resulting residual stress is highly correlated with growth conditions. A crucial role is played by hydrogen present in the sample in different forms.

3. MICROSTRURAL CHANGES UNDER EXTERNAL INFLUENCES

Light induced metastability of hydrogenated amorphous silicon is one of the most extensively investigated areas since its discovery in 1977 [17]. This phenomenon of reversible metastable changes observed in the opto-electronic properties of *a*-Si:H when environmental stress is applied, whether by illumination, voltage bias or electrical current, constitutes a serious limitation to the widespread applications of this kind of material. The most well known and highly investigated is the degradation of electrical conductivity (increase in the dark conductivity and decrease in photoconductivity) known as Staebler-Wronski effect (SWE) [78]. The SWE involves the creation of midgap electronic states at densities around 10^{16}-10^{17}cm^{-3} after a prolonged exposure to light. It is well established that these defects are dangling bonds that act as recombination centres for generated carriers. Despite considerable efforts over the last 30 years, the microscopic mechanisms behind this effect are still not fully understood, and thus present a challenge to physicists and engineers [20].

3.1 Light Induced Degradation

Several types of microscopic models, each based on a different defect creation mechanism, have been proposed to explain the light induced metastability in *a*-Si:H. All these models try to explain different experimental results observed in *a*-Si:H, but none of them has managed to explain all the aspects of this phenomenon. Only two models have retained attention, as they explain quite a large number of those aspects, but the detailed mechanism of defect creation in *a*-Si:H is still an open question. The first model is the weak Si-Si bond breaking model, also called the Stutzmann-Jackson-Tsai model [30], which assumes light induced degradation (LID) to be a local effect. They suggested that an electronic bimolecular recombination (or trapping) event triggers the atomic reaction of defect creation. A weak Si-Si bond is broken and a nearby H-atom (bonded to one of the Si atoms) moves into the location preventing the pair of photo-generated dangling bonds from recombining. This structural rearrangement leads to the creation of two spatially separated dangling bonds. This model, however, would imply a spatial correlation between hydrogen atoms and dangling bond defects which has been ruled out by ESR experiments [79]. The model developed by Branz [80,81], also called the hydrogen collision model,

describes LID as a long-range hydrogen motion. The model shown in figure 6 involves the breaking of Si-H bonds followed by a long-range diffusion of the H. The mobile H atoms collide in pairs, forming metastable doubly hydrogenated complexes, in the marked region in the figure, and lead to isolated dangling bonds in the amorphous network.

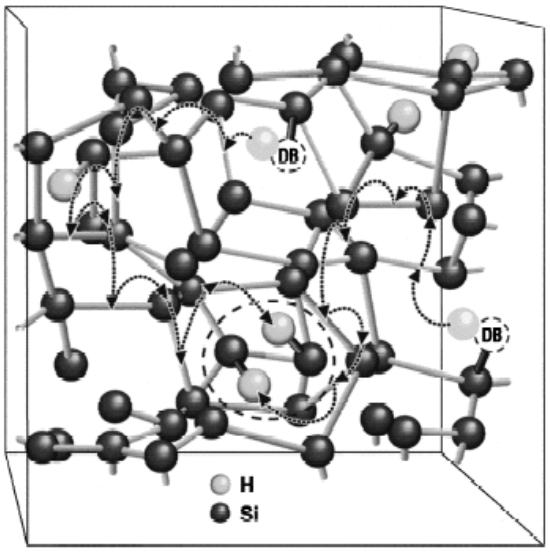

Fig.6: Schematic diagram of dangling bond creation in the hydrogen collision model [80]

Other models have also been proposed, which all suggest that H plays an active role, but it is not clear how. One of the other proposed mechanisms is the relaxation of neighbouring H-terminated dangling bonds [9] to allow the recombination of molecular hydrogen as the diffusing species.

The kinetics of defect creation is explained by a recombination model proposed by Stutzmann [30], which assumes that the defect creation is initiated by the non-radiative band-to-band recombination of an electron and a hole. This recombination releases about 1.5 eV of energy, which breaks a weak Si-Si bond and generates a defect. The defect creation rate is given by

$$\frac{dN_d}{dt} = c_d np\,, \tag{3.1}$$

where N_d is the number of dangling bonds, c_d is a constant describing the creation probability, and *n* and *p* the carrier concentrations. Provided that the illumination intensity is high enough, the carrier concentration can be expressed as

$$n = p = \frac{G}{AN_d}, \tag{3.2}$$

where A is an average recombination constant and G the generation rate. The time dependence of the defect density can be obtained by inserting equation (3.2) in the equation (3.1) and integrating to give

$$N_d{}^3(t) - N_d{}^3(0) = \frac{3c_d G^2 t}{A^2}, \tag{3.3}$$

where $N_d(0)$ is the initial equilibrium defect density. At sufficiently long illumination times such that $N_d(t) >> 2N_d(0)$ the previous equation approximates to

$$N_d(t) = \left[\frac{3c_d}{A^2}\right]^{1/3} G^{2/3} t^{1/3}, \tag{3.4}$$

which agrees with the intensity and time dependence from experimental results.

As the hydrogen plays an important role in the metastability through its property of diffusing at moderate temperatures, the most direct experimental way to study the effect of light soaking is to follow the changes in H-bonding and content and total hydrogen in the sample using different techniques such FTIR [82], ERDA [83], ESR [84], and NMR [85].

The formation of metastable defects, which act as recombination centres, is not the only structural change induced by illumination. Large scale structural changes occur in *a*-Si:H in addition to the proliferation of dangling bond defects[20]. Evidence of this is given by a reversible volume change [86, 87] which increases with light exposure. This behaviour coincides with that of light induced defects, except that while the reversible volume change keeps on growing with illumination time, the number of dangling bonds will reach saturation. Therefore, the volume changes cannot be limited to the environment of dangling bond defects.

The use of hydrogen diluted silane gas during the growth process made it possible to produce *a*-Si:H samples with a reduced SWE [88]. This material, called protocrystalline silicon, is grown at the threshold of crystallinity, and comprises ordered regions containing less hydrogen and surroundings with more hydrogen. The threshold was seen to depend on the film thickness and the deposition ratio, and is also affected by the deposition temperature and substrate material.

Decreasing the hydrogen content of the sample also reduces the SWE. This decrease in hydrogen content reduces the hydrogen diffusion, which in turn is responsible

for the SWE. This was achieved with the HWCVD technique, but the high deposition temperature required by this technique results in hydrogen effusion near the substrate-layer interface [89], and therefore an increased number of defects in that region. Replacing hydrogen by deuterium was also considered as a way of reducing the SWE [90], as there may be a change in microstructure for the sample produced, but due to the expensiveness of deuterium, there are few works published in this area.

4. MACROSCOPIC STRAIN AND STRESS

The defects and structural reconfiguration as discussed in sections II.1.2 and II.3.1, represent changes in the atomic level strain, and hence give rise to stresses on a microscopic level. However, we are dealing with macroscopic systems, in the form of *a*-Si:H layers deposited on a substrate. Therefore we can expect that these microstresses are superimposed onto macroscopic stress fields arising from other sources. This chapter present a brief introduction to the fundamental concepts of stress and strain, and how both quantities are related to each other, followed by a discussion of the stresses in layered structures. Both considerations provide the background for the discussion of strain measurement and stress determination presented in chapter III.2.

4.1 Stress and Strain in the Framework of the Theory of Elasticity

All the previous discussions concerning strain and stress were related to microscopic features of amorphous materials, and amorphous silicon in particular. But it should be mentioned that the formalistic description of stress and strain is based on the theory of elasticity, by nature a continuum theory, ignoring the microscopic appearance of the material for which it is applied. The description below follows two textbooks, firstly the classic book of Landau and Lifschitz [91] with its rigorous mathematical approach, and secondly Noyan and Cohen's book on residual stress [92].

4.1.1 The Concept of Strain

If an external load is applied to a solid body the body deforms. The theory of elasticity describes elastic deformations, which are deformations that disappear if the applied force is removed, so that the body recovers its original shape. The continuum represents a model of the material under consideration. To describe the change of the continuum by deformations, the body is thought to be divided into small volume elements. The basic idea is that the change of the continuum has to appear continuous - not singular - with the effect that the volume elements change shape and are displaced, but do not overlap or leave gaps.

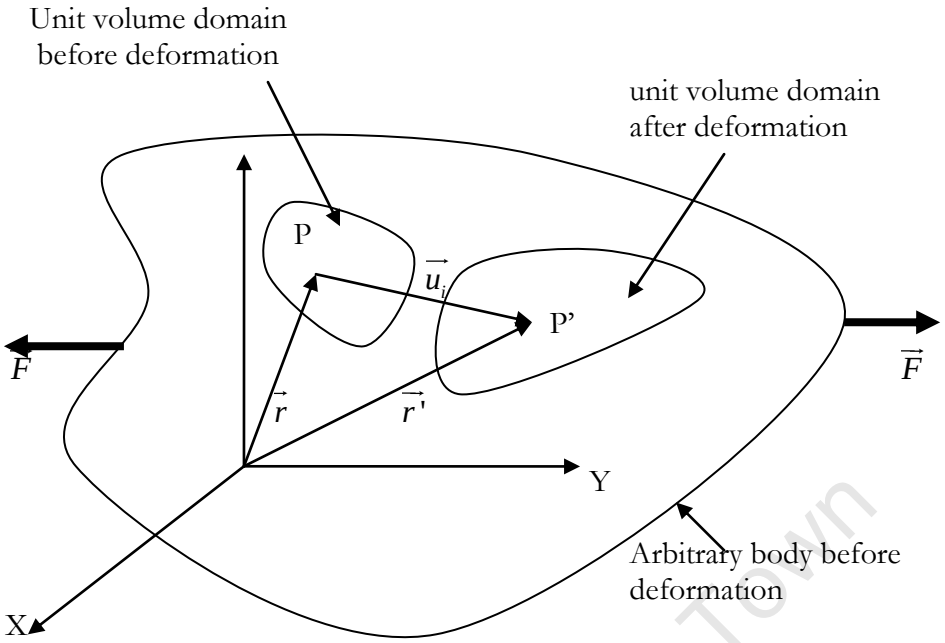

Fig.7: Behaviour of a volume element in an arbitrary body under the influence of elastic deformation, used to identify the displacement vector.

This situation is illustrated in figure 7, where one volume element in an arbitrary body is shown. The force $\vec{F}$ deforms the body elastically. The position P of a volume element before deformation is identified by the position vector $\vec{r}$ with the components $x_1 = x, x_2 = y$ and $x_3 = z$ in the coordinate system given. As long as the force acts on the body the volume element is deformed and its new position is given by the position vector $\vec{r}'$ with components $\vec{x_i}'$. The displacement of the volume element may be identified by the displacement vector

$$\vec{u_i} = \vec{x_i}' - \vec{x_i} \ . \tag{4.1}$$

It is obvious that on deformation all points of the body change position, and more importantly, the distances between the points will also change. Taking only two points, infinitesimally separated, into account, the distance between the points before deformation is given by

$$dl = \sqrt{dx_1^{\,2} + dx_2^{\,2} + dx_3^{\,2}} \ , \tag{4.2}$$

and, after deformation by

$$dl' = \sqrt{dx_1{}'^2 + dx_2{}'^2 + dx'_3{}^2} \ . \tag{4.3}$$

Applying the summation convention, and using the substitution $du_i = \frac{\partial u_i}{\partial x_k} dx_k$ yields after rearrangement

$$dl'^2 = dl^2 + 2u_{ik} dx_i dx_k \ . \tag{4.4}$$

This equation defines the strain tensor as a symmetric second rank tensor

$$u_{ik} = \frac{1}{2}\left(\frac{\partial u_i}{\partial x_k} + \frac{\partial u_k}{\partial x_i} + \frac{\partial u_l}{\partial x_i}\frac{\partial u_l}{\partial x_k} \right). \tag{4.5}$$

Elastic deformations are in general small. Assuming that the displacement vectors are also small, the second term in the definition of the stress tensor can be ignored. Renaming the strain tensor, together with the above assumption yields

$$\varepsilon_{ik} = \frac{1}{2}\left(\frac{\partial u_i}{\partial x_k} + \frac{\partial u_k}{\partial x_i} \right). \tag{4.6}$$

The strain therefore represents the mutual change of position of the points in a body under elastic deformation. For completeness the symmetric strain tensor is given as

$$\varepsilon_{ik} = \begin{pmatrix} \varepsilon_{xx} & \varepsilon_{xy} & \varepsilon_{xz} \\ \varepsilon_{yx} & \varepsilon_{yy} & \varepsilon_{yz} \\ \varepsilon_{zx} & \varepsilon_{zy} & \varepsilon_{zz} \end{pmatrix}. \tag{4.7}$$

The diagonal elements of the strain tensor are called the normal strain, while the off diagonals are called shear strain.

4.1.2 The Concept of Stress

As seen above, the deformation of a body is caused by an external applied force. On a microscopic level, working against the binding forces between the atoms, the applied force causes the body's atoms to deviate from their position. The binding forces act in a way such that they act to set the atoms back to their equilibrium position - when the applied load is removed. Therefore deformation yields a distribution of internal forces. Referring the internal forces to areas inside the body, say the faces of the volume elements, leads to the concept of a distribution of stresses. It should be mentioned that in the framework of the macroscopic theory of elasticity, only the distribution of the stresses is of

relevance. The sources of the internal stresses, the individual binding forces, do not appear explicitly in this theory, because of their short interaction distance.

The concept of stress can be demonstrated by investigating the resulting force on an arbitrary volume ΔV inside an elastic body under an applied load. The total force acting on this volume is

$$\Delta\vec{F} = \int_{\Delta V} \vec{f}(\vec{r})\, dV\,, \tag{4.8}$$

where $\vec{f}(\vec{r})$ is the local force (per unit volume) at a position $\vec{r}$ enclosed by the infinitesimal volume element dV. When we consider that the sum of internal forces inside ΔV is zero, ΔF can be thought of as the resultant force acting through the surface of ΔV, which is balanced by the forces from the material outside. If we can represent $\vec{f}(\vec{r})$ as a gradient, or more accurately as a divergence, we can apply Stokes' theorem to obtain a surface integral

$$\int_{\Delta V} \vec{f}(\vec{r})dV = \int_{\Delta V} \left(\nabla\cdot\tilde{\sigma}(\vec{r})\right)dV = \int_{\Delta S} \tilde{\sigma}\cdot d\vec{s}\ . \tag{4.9}$$

In this case then the force per unit volume is the gradient of a second rank tensor $\tilde{\sigma}$ with the dimension of force per unit area, whose components are given by

$$f_k = \sum_l \frac{\partial\sigma_{kl}}{\partial x_l}\,. \tag{4.10}$$

This tensor is the stress tensor, which, similarly to the strain tensor, is a symmetric second rank tensor, and can be expressed in component form as

$$\sigma_{kl} = \begin{pmatrix} \sigma_{xx} & \sigma_{xy} & \sigma_{xz} \\ \sigma_{yx} & \sigma_{yy} & \sigma_{yz} \\ \sigma_{zx} & \sigma_{zy} & \sigma_{zz} \end{pmatrix}, \tag{4.11}$$

where σ_{xx}, σ_{yy} and σ_{zz} are known as normal stress, and σ_{xy}, σ_{xz} and σ_{yz} the shear stress.

4.1.3 Relationship Between Stress and Strain in the Elastic Domain

Under the assumption of small deformations, or the so called elasticity domain, the strain tensor components of the deformed body, depend linearly on the component of stress tensor, as expressed by the generalized form of Hook's law [92]

$$\varepsilon_{ij} = \sum_{k,l=1} S_{ijkl}\sigma_{kl} \ . \tag{4.12}$$

The proportionality constants S_{ijkl} are known as compliances, and are represented in a 4th rank tensor. Vice versa, the inverse tensor of the compliance tensor, the tensor of the elasticity constants or stiffness constants, C_{ijkl}, which is also a 4th rank tensor, represents the stress as a function of strain

$$\sigma_{ij} = \sum_{k,l=1} c_{ijkl}\varepsilon_{kl}. \tag{4.13}$$

At this point it should be mentioned, that the Hooke's law not only shows the relationship between stress and strain, but also introduces material specific properties into the framework of the theory of elasticity. The concept of stress, as well as the concept of strain is purely theoretical. For their explanation no information of the real material is used. In contrast, both elastic constants or compliances introduce, with their material dependence, the taking into account of the huge variety of solid materials with their vast difference in mechanical properties.

Because the strain and stress tensors are symmetric, the maximum number of independent elastic constants is reduced from 81 to 36. However, due to elastic energy considerations the number of these independent constants is further reduced to 21 [93]. The elastic response of a single crystalline solid should therefore be described by 21 independent elastic constants. This is true for a material crystallizing in the triclinic crystal structure, but because of the increasing symmetry of the crystal systems, the number of elastic constants reduces. For materials with a cubic crystal structure, the structure with the highest symmetry, only three independent elastic constants are sufficient to describe the elastic properties. For an elastically isotropic body in the form of a polycrystalline solid with out texture, only two independent constants are left. These are generally given as Young's modulus E and Poisson's ratio ν. This means that elastic behaviour of a

homogeneous and isotropic body can be fully described in terms of the two elastic constants, which should be the case for *a*-Si:H.

4.2 Residual Stress in Layered Systems

Residual stress is defined as the stress that remains in a material in the absences of external load such as applied force or thermal gradient [92]. Investigation of the origins, magnitude and the control of residual stresses is of paramount importance because of their influence on device lifetime and performance, which may be either beneficial or detrimental. This applies equally to the electronic properties of a device from *a*-Si:H as to a mechanical component. In the broadest sense residual stresses originate from misfits between regions of a material or composite material [93], whether over the atomic scale or extending over distances which are large compared to the samples. Residual stresses can be categorized by their causes, the length scale at which the stress equilibrates, or the methods used to determine them [92]. in terms of length scale residual stress can be divided into two classes. Macroscopic stress or macrostress extends over distances that are large relative to the characteristic size of the material. The term microscopic stress or microstress refers to fluctuations of the average stress over a short-range relative to the scale of the macrostructure of the material. Microstresses are often distinguished into different categories. Common distinctions for polycrystalline materials are Type II and type III residual stresses [92], which correspond to intergranular and intragranular stress fluctuations respectively. The extreme limit of microstress is the atomic level stress, which is often applied in theoretical studies of amorphous network [94].

The basic principles for the genesis of stress in *a*-Si:H layers are the same as in any other layered system. A classification scheme for internal stresses according to their origin is given in figure 8. It should not be thought, however, that there is a one to one correspondence between these definitions and the above definition of macro-and microstresses. While it is obvious that a macroscopic cause of stress will result in a macrostress, it is by no means the case that a microscopic origin will lead only to microstress. It is possible that these will add coherently, resulting in a macroscopic stress distribution.

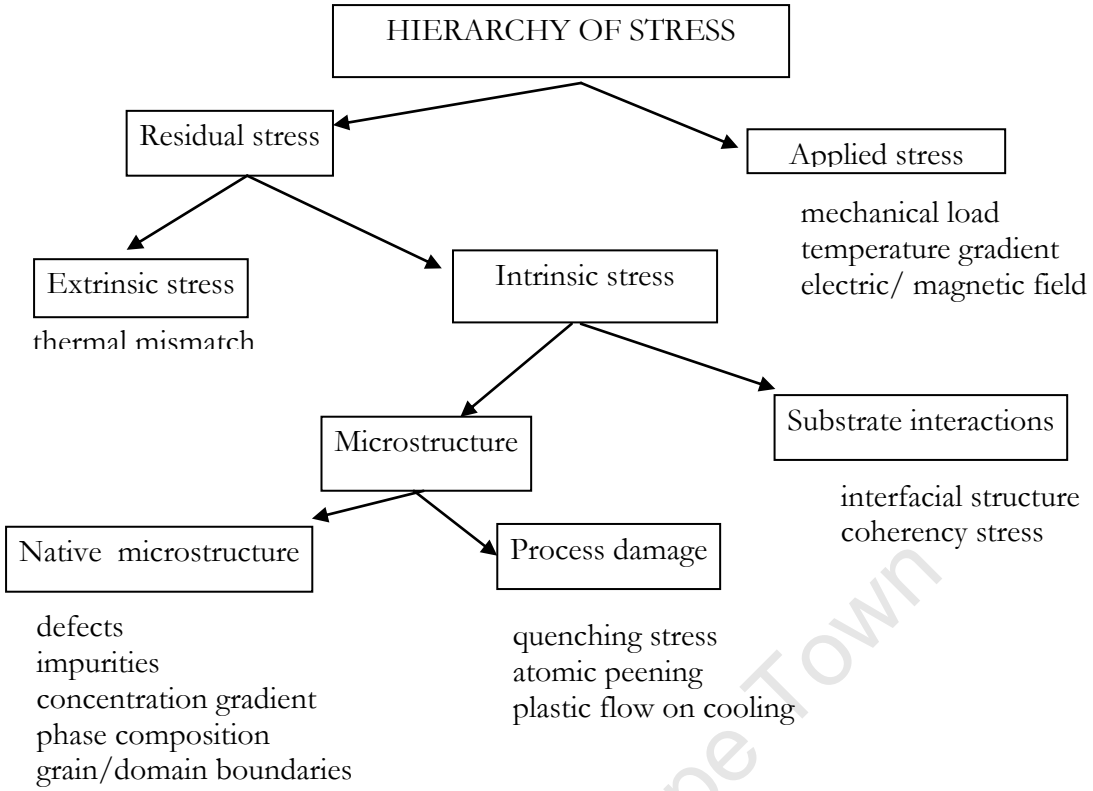

Fig.8: The hierarchy of stress, classified according to origin, in a layered system.

As seen in figure 8 the residual stress can be described as a superposition of extrinsic and intrinsic contributions [95]. In binary systems, like thin layers on a substrate, the main extrinsic cause of residual stress is a thermal mismatch which originates from the differences in the thermal expansion coefficient of the layer and the substrate. In general, the film and the substrate have different coefficients of thermal expansion, and therefore as most of the films are deposited at elevated temperature T_d, they will contract differently when cooling down to the operating temperature T_0. The unconstrained strain in any material caused by thermal expansion $\varepsilon(T)$ is isotropic and given by

$$\varepsilon(T_d) = \varepsilon(T_0) + \alpha_T \Delta T \tag{4.14}$$

where $\Delta T = T_d - T_0$ and α_T is the coefficient of thermal expansion. The difference between the expansion of the film and the substrate gives the resulting constrained strain in the film, known as the thermal mismatch strain

$$\varepsilon = (\alpha_{Tf} - \alpha_{Ts})\Delta T \tag{4.15}$$

where α_{Tf} and α_{Ts} are linear thermal extension coefficients for the layer and the substrate respectively. This thermal mismatch will result in stress in the film which can be assumed

to be biaxial in the centre of the film, away from the edge, as there is nothing to support stress in direction normal to the surface.

Using the generalized form of Hooke's law (eq. II. 4.13) to relate the stress and the strain in the principal coordinate system, and taking into account that the stress component in the normal direction is zero, gives the in plane thermal mismatch σ_{fm} [95]

$$\sigma_{fm} = \frac{E}{1-\upsilon}(\alpha_{Tf} - \alpha_{Ts})\Delta T \,. \tag{4.16}$$

where υ is Poisson's ratio. If the appropriate material constants and the deposition temperature are known the thermal contribution can easily be calculated.

On the other hand, the evaluation of the contribution of intrinsic stress is more complicated. The cause of intrinsic stress can be subdivided into two major contributions, resulting from the microstructure of the layer itself and the interactions with the substrate. As discussed earlier, the intrinsic stress can result from numerous native microstructural features such as film densification during the deposition [43], vacancies and dangling bonds defects [41], and incorporation of hydrogen or other impurities [43]. Other reported sources of intrinsic stress in a-Si:H, resulting from the deposition process, are the atomic peening effect [96], which causes the layers to become over dense, and implantation of working gas atoms [98], even though conclusive evidences for these effects is not yet reported.

Quenching stresses [95] and thermal relaxation stresses [92], resulting from plastic deformation during rapid and slow cooling respectively, which are well known in other deposition processes, are not thought to be significant in CVD deposition of *a*-Si:H.

Generally, substrate interactions are only a significant source of intrinsic stress in epitaxial systems, where a coherency stress occurs because of a mismatch in lattice parameter [99]. However, in a-Si:H, there is a difference in the properties of the first atomic layers at the beginning of the deposition, which may show a different stress state, but the contribution of the so called interfacial stress is not significant for samples thicker than 0.5μm [100].

III. EXPERIMENTAL TECHNIQUES

1. SAMPLE PREPARATION

1.1 Technical details about HWCVD

As discussed above *a*-Si:H layers are prepared in non-equilibrium conditions, and their properties depend on the preparation method and deposition conditions. In hot wire CVD the key issues pertaining to the deposition are: filament and substrate temperatures; reaction gas pressure; flow rate and dilution; and the distance between the filament and the substrate.

The filament temperature and the gas pressure both have a significant effect on the fraction of the silane used. The reaction rate increases as both the filament temperature and the gas pressure increase [101]. The exhaust mole fraction of silane is seen to decrease exponentially with increased filament temperature in the range of 1550 to 1850 ^{o}C. Therefore, the filament temperature determines the nature of the dissociation products and the composition of the gas plasma during the deposition process [102].

When the pressure is higher the possibility for secondary reactions becomes higher [103], and therefore the content of radicals of SiH, SiH_2 and SiH_3 is increased, and subsequently the film quality is lower. Similarly, the amount of hydrogen dilution of the silane determines the partial pressure of both gases, and is crucial for the properties of the deposited layer [104]. At a low silane flow rate the growth rate of the layer increases linearly with silane flow rate, due to a decrease in the residence time, but at a very high flow rates the kinetics of silane decomposition becomes rate limited due to the very short residence time [103].

As discussed in chapter II.3.2, the substrate temperature determines the dynamics of the film growth and influences the crystallinity of the deposited film. This is made possible by the increase of the mobility of the growth precursors at the surface of growing layer.

The total pressure and the distance filament and substrate determine the free path of different dissociation products, and their mobility on the growing layer. Hence they

influence both the gas-phase composition and the deposition rate. The filament to substrate distance also influences the nucleation, the growth rate and the hot wire radiative heating of the substrate

1.2 *a*-Si:H Deposition

The hot wire chamber at the University of Western Cape, used in this work, is a single chamber hot wire chemical vapour system, produced by MVSystem Inc. for the deposition of high quality doped and undoped a-Si:H films. It consists primary of two stainless steel vacuum chambers: the load-lock and an ultra high vacuum reaction chamber, coupled with a turbomolecular pump, which yields a base pressure of around 10^{-7} mbar. The gas supply units are connected to different gas bottles through Matheson pressure regulators, and the gas line connections are controlled with high vacuum pneumatic valves, which are controlled from a separated set of solenoid air pressure valves. The process pressure can be held constant by using a throttle valve.

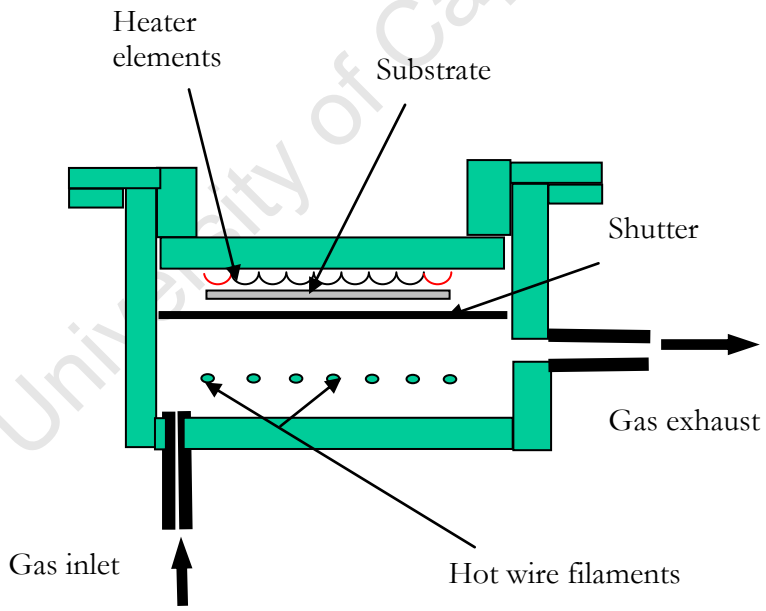

Fig.9: Sketch of the side view of the deposition chamber used to produce a-Si:H layers used in this work

A sketch of the deposition chamber is shown in figure 9. Seven parallel tantalum wires of 0.5mm diameter placed at a distance of 36 mm from the sample holder were used as the filament assembly. These parallel filaments, each of length 7cm, are spaced 3 cm apart from each other.

The filament temperature is estimated with an optical pyrometer (Chino Corp., Japan) by observing the heated filament through the glass viewport, as well as by monitoring the filament current. Prior to deposition the substrate temperature is set to the appropriate value using the temperature controller, and left to stabilize for about an hour, during which the adsorbed water vapour is also removed from the substrate, the chamber and sample holder. An external thermocouple, installed on the sample chamber, is calibrated against the thermocouple at the sample position and the accuracy for the sample temperature at 500°C is ±5°C. This calibration neglected the heating of the substrate by the filament. The deposition is then carried out for desired length of time, and a shutter is brought between the substrate and the rest of the reaction chamber to stop the deposition. The deposited layers are then allowed to cool down to room temperature in the load lock chamber to avoid additional radiative heating from the filament wire, and to prevent atmospheric contamination by oxygen or other impurities. To minimize the formation of tantalum silicide, which leads to a rapid aging and breaking of the filament, the chamber was cleaned immediately after each deposition for about 5 minutes by allowing hydrogen only to flow through the chamber.

In each deposition, two 25mm square samples were produced simultaneously on <100> oriented crystalline silicon and glass substrates. The samples deposited on silicon were used in FTIR experiments to determine the bonded hydrogen content in the sample, because of silicon's good infrared transparency. For most other purposes however, the glass is a better choice substrate because of its low cost, transparency, electrical insulation, and chemical stability. Prior to deposition the substrates were cleaned in an ultrasonic bath with organic solvents to remove impurities from their surfaces. The cleansing sequences were 5 minutes in acetone followed by 5 minutes in ethanol. In addition the silicon substrates were also etched for about a minute in hydrofluoric acid (HF) to remove any native oxide.

During deposition, the tantalum filament temperature was kept constant at 1600 ^{0}C. Pure silane gas was used as the reactive gas, at a constant flow rate of 60 sccm, and the total pressure inside the chamber was maintained at 40 μbar. As the main investigation concerns the effect of the substrate temperature on the microstructure and defect structure in a-Si:H, this was varied between 150 to 500 ^{0}C. To obtain layers of different nominal thickness, two different deposition time times, of 11 and 20 minutes, were used. From the

sample thickness, the deposition rate at all temperatures is approximately 200nm/min which is comparable to the reported 180nm/min for undiluted silane [105]. The deposition parameters are summarized in table 1.

Sample identity	Substrate temperature [^{0}C]	Deposition time[minutes]
Mw139	250	20
Mw140	350	20
Mw141	400	20
Mw142	250	20
Mw145	250	11
Mw148	300	11
Mw150	400	11
Mw151	500	11
Mw152	350	11
Mw153	450	11
Mw170	150	11
Mw172	300	11
Mw173	500	11

Table 1: The deposition parameters for the set of samples of different *a*-Si:H layers studied in this thesis.

1.3 Sample Illumination

To investigate the effect of illumination, a set of 3 samples, Mw170, Mw172, and Mw173, deposited at 150, 300 and 500^{0}C were used. Each sample was cut into 4 small pieces approximately 10mm × 10mm square. The light soaking experiments were performed using a metal halide lamp (Osram HQI E 400W/D). The lamp and sample stage is housed in a mirrored chamber, with internal dimensions 0.5×0.5×0.5 m^3, with forced air-cooling. The use of the mirror in the box was to increase the illuminance, which was increased by a factor of 20 compared to the naked bulb. However, it has some slight drawbacks as the red blue, UVA and IR components of the spectrum are reduced because of the preferential absorption in the glass. The resultant effect is that the light has a notable green tone.. When switched on the illuminance stabilises within 10 minutes, and the

temperature at the sample stage, estimated at $(31\pm1)^0$C, stabilizes after 20 minutes. The measured illuminance over longer periods at the sample position was approximately 110 Wm^{-2} [106]. Illumination was performed on one piece of each sample for 12 and another for 48hrs.

2. DIFFRACTION AND STRESS DETERMINATION IN *a*-Si:H

Diffraction techniques have long been used extensively for investigating the structure of crystalline or polycrystalline materials. However, it was shown very early that using a modified diffraction technique, macro- and average microstrain, and therefore macro- and average microstresses, in specific phases can be estimated in a non-destructive way [92]. Due to the high absorption, and therefore the low penetration of X-rays, they can only probe the near surface region, whereas neutron diffraction can be used to investigate the bulk of the specimen [12].

Stress, or rather strain, measurement using X-ray diffraction methods is a form of precision measurement of the crystal lattice. It has the advantage over other conventional methods, in that it is a non-destructive method for determining the initial and residual stress in a specimen. One of the main characteristics of this diffraction method is to provide an intra-granular stress value, which is different to the global value often measured by other techniques such as the curvature method [107]. Also, diffraction methods usually measure the strain in a region less than 1 or 2 mm in diameter, and therefore the method allows the study of localized stresses, and the observation of steep stress gradients thereby becomes possible.

This section on synchrotron radiation diffraction is organized as follows: the first section presents an overview on X-ray diffraction in general, and on amorphous materials in particular. This is followed by an elementary description of stress determination by X-ray diffraction methods, starting with crystalline material and extending the discussion to focus on stress determination in amorphous materials. The third part discusses the experimental details on how the measurement were performed, while the final section presents, and discusses, the results in terms of stress and microstructure .

2.1 Diffraction in Amorphous Materials

Discovered in 1895 by a German physicist Conrad Rontgen as invisible rays of unknown nature when a high potential was applied between two electrodes in an evacuated tube, X-rays were later recognized as electromagnetic radiation by von Laue, Friedrich, and

Knipping [92]. In 1912, they established the electromagnetic wave nature by passing X-rays through a crystal of ZnS and observing diffraction. They therefore concluded that, firstly crystals are composed by periodic arrays of atoms extending in three dimensions, and secondly, that crystals caused distinct x-ray diffraction patterns because the distance between atoms are the same order of magnitude as the wavelength of X-rays. Two basic concepts lay behind these findings: firstly, X-rays scatter from the electrons of the atoms in the crystalline structure, and secondly the regular array of scatterers produces diffraction patterns inherent to an individual material because of constructive and destructive interference of the isotopically scatted X-rays from the individual ion cores. Further studies by W.H. Bragg and W.L. Bragg showed in 1914 that diffraction patterns can be used to determine the relative position of atoms within a single crystal.

The most elegant way to present the diffraction condition is given by the Laue condition

$$\vec{k} - \vec{k'} = \vec{G} \tag{4.17}$$

where $\vec{k}$ and $\vec{k'}$ are the wave vectors of the incident and scattered X-rays respectively, and $\vec{G}$ is the translation vector of the reciprocal lattice. A more intuitive understanding of the diffraction conditions is given by the Bragg model of diffraction. In this model, the crystalline structure is represent by evenly spaced sheets running through the centre of atoms in the material, and each reflection is associated with a different set of these sheets. The orientation of particular set of sheets is identified by its three Miller indices *(h,k,l)* and their spacing *d*. W.L. Bragg proposed a model, in which the incoming X-rays are scattered specularly from each plane. Under this assumption, the x-rays scattered from adjacent planes will interfere constructively depending on angle θ between the plane, and the resulting X-ray path difference will be an integer *n* multiple of the x-ray wavelength λ,

$$2d \sin\theta = n\lambda \,. \tag{4.18}$$

This law relates the diffraction phenomenon to the crystal structure, and has facilitated the study of the structure and the behaviour of material.

2.1.1 Introduction to Amorphous Diffraction

Considerable effort was made over the early years of the twentieth century to develop diffraction theories, for both for single crystalline and polycrystalline material, as well as for the development of refined equipment and experimental techniques, because of the ability to use X-ray diffraction as a powerful tool to investigate the internal structure of crystalline matter. Beside this development, it was understood from the beginning that X-ray diffraction can provide valuable information if applied to non-crystalline matter. This can be seen from the fact that R.W. James, professor of Physics at the University of Cape Town, dedicated in his classic book, *The Optical Principles of the Diffraction of X-rays* [108], a full chapter to this topic. He set the framework as follows: "no arrangement of molecules of a finite size can be a random one in the sense that all positions are equally probable at any instant for any molecule of the assemblage, there must be a rudimentary degree of arrangement….this is in principle enough to give rise to diffraction phenomena". This statement should be seen as the background for the next section.

As discussed in section I.1, the description of the hierarchy of structural order in material ranges from short range order, through intermediate range order, to long range order. Using the idea of length scale, illustrated in figure 10, the long range order decreases from single crystalline material, through polycrystalline material and nanocrystalline material, to amorphous material, and finally to liquids and gases. The ideal single crystal has atoms, ions, or molecules arranged in a particular structure. In this case, translational symmetry is maintained over the whole crystal. Polycrystalline materials are the next most ordered materials. They are formed from single crystalline grains, where the long range order is maintained inside the grain, separated by the grain boundaries which are not ordered. The long rang order is therefore maintained over shorter distances than in single crystalline materials, and mainly at the size of individual grains. Nanomaterials have similar features to polycrystalline material, but the length scale of the ordered structure is in nanometre range. These materials are at the transition to short range ordered materials. As discussed in I.1, amorphous solids possess only short, and possibly medium, range order. Finally, liquids and gases are the classical examples of matter which generally exhibit only short range order.

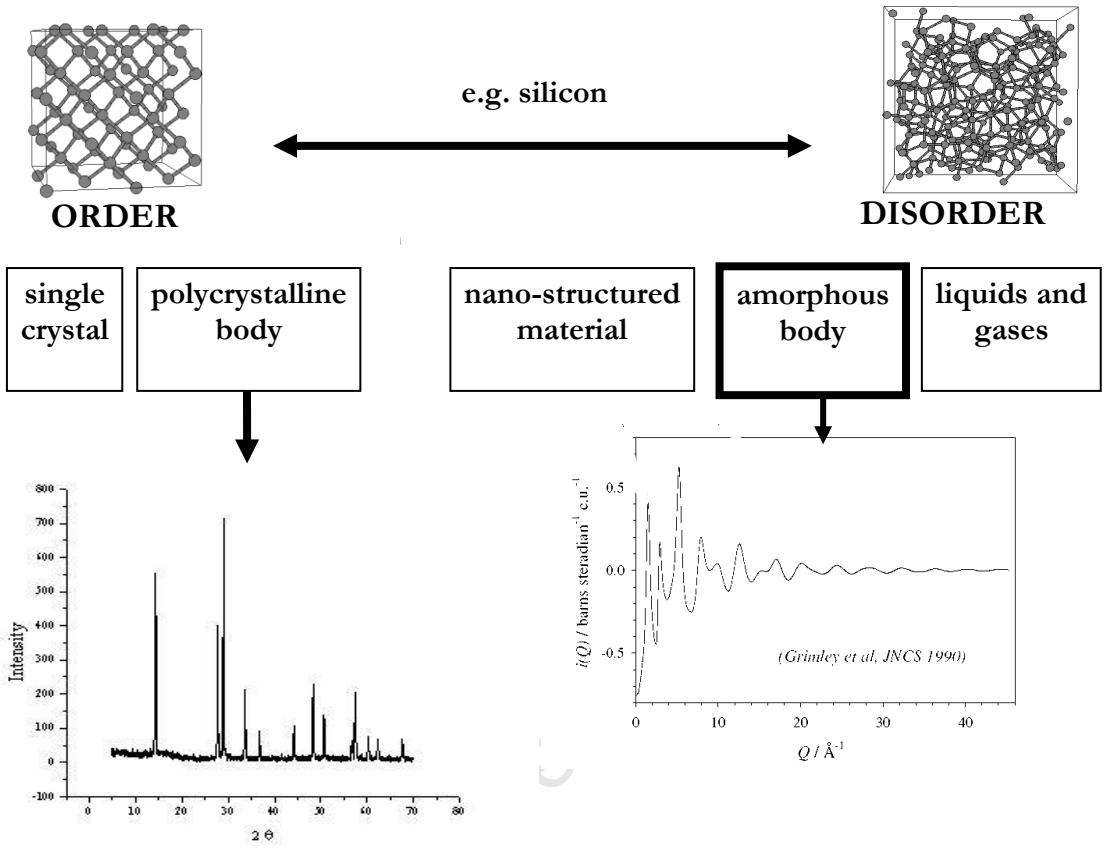

Fig.10: Relationship between order and diffraction in condensed matter.

In a single crystal, which is the most ordered; diffraction will only occur if a set of crystallographic planes satisfies the Bragg condition. In this case, whether diffraction peaks occur depends on the orientation of the crystal in the diffraction experiment. In the case of a polychromatic beam of X-rays, diffraction will occur for all the sets of planes that satisfy the Bragg law with one of the available wavelengths.

The most common diffraction experiments are performed on polycrystalline materials. In this type of material, where coarse single crystalline grains are randomly oriented with respect to the incident beam, planes of different spacing may be available for diffraction from each grain. Therefore a monochromatic beam will diffract at different angles from each grain. The number and position of peaks in the diffraction pattern depends on the crystal structure of the material. Compared to a large perfect single crystal, the shape of the peak in a typical polycrystalline material is broad, indicating a decrease in the long range order. As the size of the grains in polycrystalline material becomes smaller,

or, in other words, the structure becomes less ordered and the distance, over which the regular repetition of a given pattern describing the crystal structure is maintained, the shape of the peak becomes broader [109]. This is the case for nanocrystalline materials. The next less ordered material is amorphous material. In this type of material, where the long range order is lost and only short range order is present, the peaks in their diffraction patterns are broader, and their intensities decrease. As shown in the example (fig. 11), there are also far fewer diffraction peaks than in the pattern for the same material in crystalline form, typically only two or three, although for a high *q*-range and a good signal to noise ratio more than five may be seen.

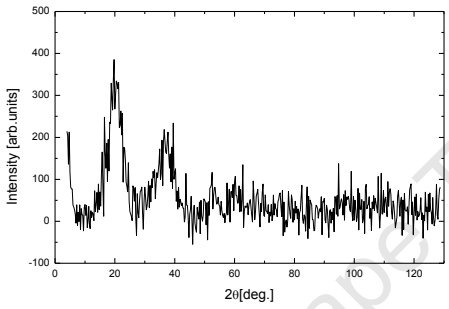

Fig.11: Typical diffraction pattern from a-Si:H deposited on a glass substrate showing only two broad peaks

In the case of crystalline solids, the resulting diffraction patterns comprising both the position and intensities of the diffraction effects are used for the identification of the substance and the determination of its complete structure [109]. Analysis of these positions and intensities leads immediately to the knowledge of the position of the individual atoms in the cell, and also the size, the shape, and the orientation of unit cell. To a limited extent this is also possible in covalently bonded amorphous materials, like *a*-Si:H which have a known local structure [9]. However, more information can be obtained from the diffraction data of amorphous material when the diffraction patterns are Fourier transformed from reciprocal space into real space. In this case the diffraction intensities are expressed as a function of the real distance *r*. The transformation from reciprocal space to real space yields a radial distribution function, which is seen as a very useful representation of the topology of an amorphous network [110]. Such an analysis was first developed for liquids by Zernike and Prins [111] in 1926, and applied to solids by Warren [112] ten years later. The next section presents a theoretical derivation of the radial distribution function, as developed by Zernike and Prins and still applied in most standard texts.

2.1.2 The Derivation of the Radial Distribution Function

The basis for radial distribution analysis is the Debye equation [109], which expresses the intensity, as a function of the scattering vector $k = 4\pi \sin\theta / \lambda$, scattered by non-crystalline arrays of atoms at the angle θ,

$$I(k) = \sum_n \sum_m f_m f_n \frac{\sin kr_{mn}}{kr_{mn}}, \tag{4.19}$$

where f_m and f_n are the respective atomic scattering factors of the *m*th and *n*th atoms, and r_{mn} is the magnitude of the vector separating two atoms. The double summation is taken over all pairs of atoms in the ensemble. In this equation it assumed that the material is isotropic so that the vector $\overrightarrow{r_{mn}}$ may adopt all orientations with equal probability, which is a good approximation for amorphous materials.

If it is assumed that the material is monoatomic with the density function ρ, a new expression for the intensity scattered by such arrays of *N* atoms is [3]

$$I(k) = Nf^2 \left(1 + \int_0^\infty 4\pi r^2 \rho(r) \frac{\sin kr}{kr} dr \right), \tag{4.20}$$

where the subscript has now been omitted from the atomic scattering factor *f*, and $4\pi r^2 \rho(r)$ is the radial distribution function. In equation (4.20), the distribution of atoms about any reference atoms is regarded as continuous function and the summation has been replaced by an integral. If we introduce ρ_o, the macroscopic density, in the case of amorphous materials, the quantity $(\rho(r) - \rho_0)$ will tend to zero for distances greater than a few primary atomic separations. This consideration transforms the equation (4.20) into

$$I(k) = Nf^2 (1 + \int_0^\infty 4\pi r^2 [\rho(r) - \rho_0] \frac{\sin kr}{kr} dr), \tag{4.21}$$

where the infinite upper limit is justified since the size of the sample in such experiments is much greater than the atomic dimensions.

Finally, the introduction of the reduced scattering intensity *f(k)* and the reduced radial distribution function *G(r)*, defined as follows

$$f(k) = k(\frac{I}{Nf^2} - 1), \tag{4.22}$$

and

$$G(r) = 4\pi r[\rho(r) - \rho_0], \tag{4.23}$$

into equation (4.21) yields the following expression

$$f(k) = \int_0^\infty G(r)\sin krdr. \tag{4.24}$$

The importance of this equation is that the quantity *f(k)* is directly obtainable from experiment, while the function *G(r)* describes the real space structure of the amorphous solid. The Fourier transform of equation (4.24) leads to the expression below

$$G(r) = \frac{2}{\pi}\int_0^\infty f(k)\sin krdr. \tag{4.25}$$

Since the range of values of *k* accessible to experiments is strictly limited, errors may occur in the conversion of reciprocal space data to the real space correlation function via Fourier transforms [3]. This has a direct consequence of introducing what are called termination errors, as $f(k)$ seems to be multiplied by a modification function *M(k)* which is equal to 1 for $k < k_{\max}$, and 0 for $k > k_{\max}$,

$$G'(r) = \frac{2}{\pi}\int_0^{k\max} f(k)\sin krdr = \frac{2}{\pi}\int_0^\infty f(k)M(k)\sin krdr \ . \tag{4.26}$$

The effect of this is a loss in resolution since small distances in real space are lost.

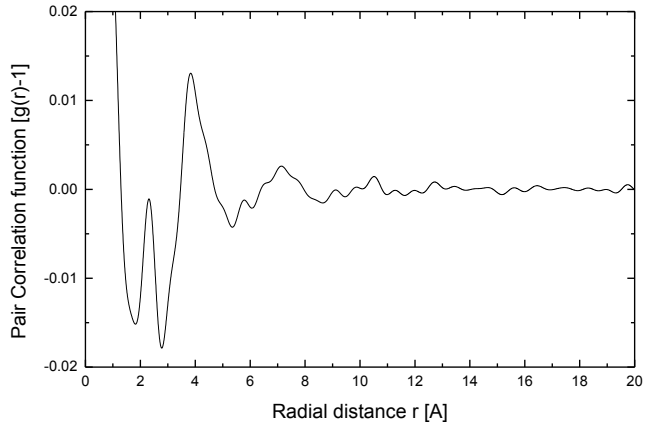

Fig. 12: Typical pair correlation function from an amorphous material.

The radial distribution function for amorphous materials exhibits an oscillatory behaviour [113], with the peak in the probability function representing the average interatomic separation as shown in figure 12. As discussed in chapter II.1, the position of the first peak gives a value of the average nearest neighbour bond length r_1 and similarly the position of the second peak gives the next nearest neighbour distance r_2.

2.2 Strain Determination in Amorphous Materials

X-ray stress determination is well known in crystalline and polycrystalline materials. In these ordered materials, diffraction techniques yield well defined peaks in reciprocal space. The technique is based on measuring the peak shift in the diffraction pattern as the sample is tilted through different angles, and therefore the structural lattice spacing is used as an internal strain gauge. In this section, the principle of stress determination will be discussed, and the possibility of applying the same technique to analyse the stress in amorphous materials will be highlighted.

2.2.1 Background on Strain Determination in Amorphous Materials

Earlier studies on the effect of applied stress on diffraction pattern of amorphous matter were for hydrostatic stress on gaseous isopentane [114] and nitrogen [115]. In both cases a clear dependence of position of the first amorphous diffraction peak on pressure

was observed. A similar study on ether was carried out by Spangler [116] who focussed on the effect of pressure in the gas phase, and temperature in the liquid. Although not reported on, his data show a slight dependence of the diffraction peak position on applied pressure in the liquid at 184.5^{0}C.

The first systematic study reporting on the peak shift in X-ray diffraction measurements on disordered condensed matter was by Einstein and Gingrich [117] in 1942, who obtained different diffraction patterns from compressed liquid argon near its triple point.

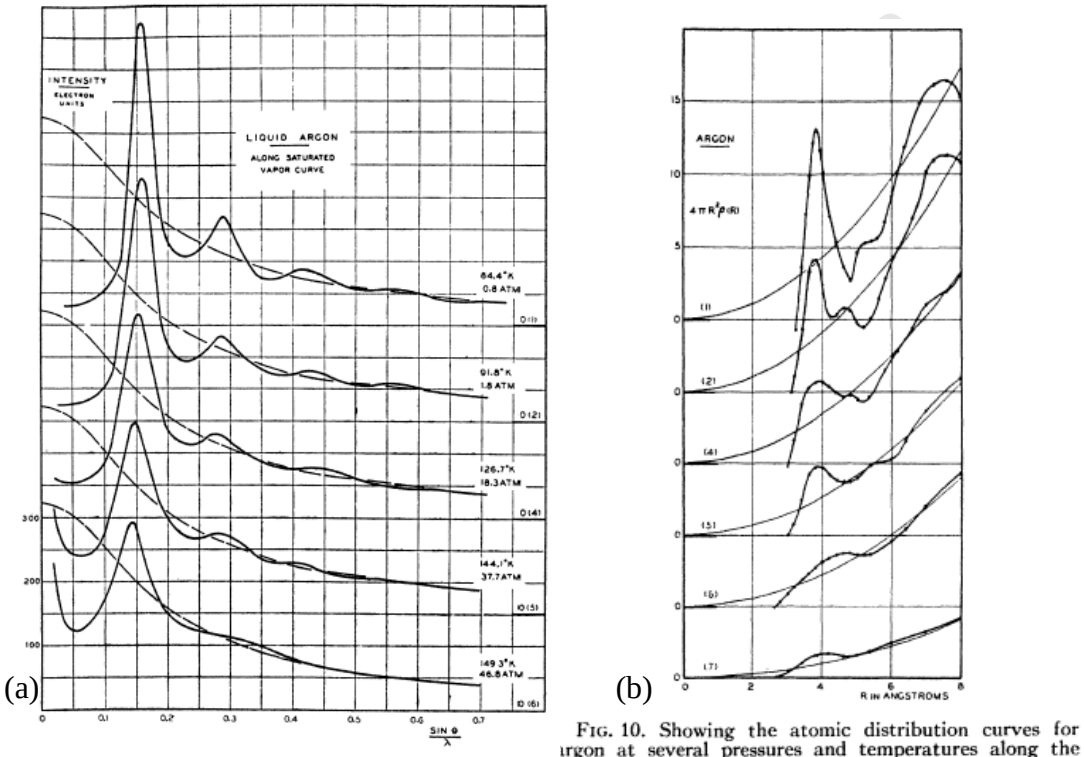

FIG. 3. The intensity patterns for argon liquid, in electron units, as a function of sin θ/λ, for the P-T conditions numbered 1, 2, 4, 5, and 6.

FIG. 10. Showing the atomic distribution curves for argon at several pressures and temperatures along the saturated vapor curve. Curves 1, 2, 4, 5, and 6 are for liquid argon; curve 7 is for argon vapor.

Fig.13: The original data of Einstein and Gingrich [117] showing shifts in: (a) the diffraction peak positions; and b) the radial distribution function, for liquid and gaseous Ar at different pressures and temperatures.

The observed peak shift seen in fig 13 a) was associated with the compression of the liquid argon, thus proving that the strain in amorphous material can be measured using diffraction techniques. Einstein and Gingrich were also the first to investigate the effect of pressure on the radial distribution function. However, the radial distribution function obtained from these diffraction patterns did not reflect the shift observed in reciprocal

space. The reason for this is that compressing a liquid increases the number of nearest neighbours, but does not change the interatomic distances significantly [118]. In their data, shown in figure 13b), the greatest changes are seen for the second coordination peak.

The first investigation in amorphous solids was by Härting *et al.* [119] in 2004, who used a conventional X-ray diffractometer to study *a*-Si:H. The shift in the first diffraction peak position was used to estimate the residual stress in the sample using the conventional $\sin^2\psi$ method discussed in the next section. In this work the silicon tetrahedron was used to provide a reference lattice parameter. The first use of synchrotron radiation on disordered material was on metallic glasses by Halevy *et al.* [120] in 2004 while analysing the deformation, under hydrostatic pressure, of a bulk metallic glass alloy. Essentially repeating the work of Einstein and Gingrich, they also observed a clear shift in both direct diffraction patterns and the radial distribution function. The first use of synchrotron radiation diffraction to analyse the strain distribution in amorphous solids under an applied uniaxial stress, was reported afterwards by Poulsen *et al.* [121]. This was followed by the analysis of biaxial residual strain in hydrogenated amorphous silicon using synchrotron radiation diffraction, using both direct diffraction patterns and the RDF, shortly afterwards by Harting *et al.* [122] in 2006. The next section will discuss how the biaxial stress can be determined with an emphasis on amorphous solids.

2.2.2 Strain Determination Using Diffraction Methods

The traditional way of measuring the strain is by determining a peak shift in a measuring direction determined by azimuthal and tilt angles, ϕ and ψ [92]. The experiments are generally performed in reflection geometry, but with high energy synchrotron radiation, experiments can also be performed in transmission geometry for strain mapping [123]. The following discussion will focus on the reflection geometry used in our study. We will first discuss strain measurement in polycrystalline material, and then apply it to amorphous silicon.

If an incident beam of monochromatic X-rays impinges on a surface of a stressed sample, the planes which are correctly oriented will diffract the X-rays hence contributing to diffraction peaks following Bragg's equation (4.18). For a fixed wavelength λ, any change in lattice spacing Δd^{hkl} will reflect in a shift of the peak position in 2θ,

$$\Delta 2\theta = -2\frac{\Delta d^{hkl}}{d_0^{hkl}}\tan\theta \tag{4.27}$$

where d_0^{hkl} is the unstrained lattice spacing.

Consider an example where a tensile stress is applied in the plane of the sample. This will result in a Poisson contraction in the perpendicular direction, hence reducing the lattice spacing d^{hkl} probed by the X-rays, and consequently increase the diffraction angle. If the lattice spacing of the unstrained material is known, the linear strain in the direction normal to the diffracting planes can be estimated using the following expression,

$$\varepsilon^{hkl} = \frac{d^{hkl} - d_0^{hkl}}{d_0^{hkl}} = \frac{\Delta d^{hkl}}{d_0^{hkl}} = -\cot\theta\Delta\theta\,. \tag{4.28}$$

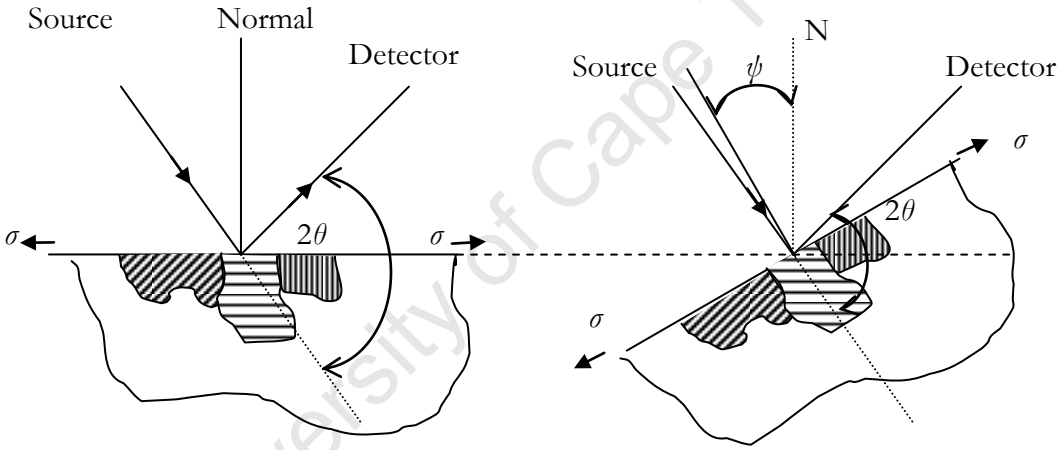

Fig.14: Illustration of strain measurement by tilting the sample surface.

By tilting the sample surface by an angle ψ, as shown in figure 14, new grains will be allowed to satisfy the Bragg condition, and hence contribute to the diffraction peak. The procedure is repeated for different ψ angles, but at the same time the sample can be rotated around an axis perpendicular to the sample surface. Negatives values for the ψ tilt can also be achieved by rotating the sample through an azimuthal angle higher than 180°.

In typical diffraction geometry, two orthogonal coordinate systems can be defined: the sample system S_i and the laboratory system L_i (fig.15). By properly defining the relative orientation φ and ψ for these orthogonal coordinate systems, we can change the above Cartesian coordinates to match the direction of maximum stress. The axes of this system

are called the principal axes, and will be used in the following discussion. The sample system S_i is made up by the axes S_1 and S_2, defining the surface of the specimen, and S_3 in the direction normal to the sample surface. The laboratory system L_i is oriented in such way that the axis L_3 is in the direction normal to the diffracting planes (*hkl*), and hence tilted by an angle ψ relative to S_3. Similarly, L_1 and L_2 are in the sample surface but rotated by an angle φ relative to S_1 and S_2.

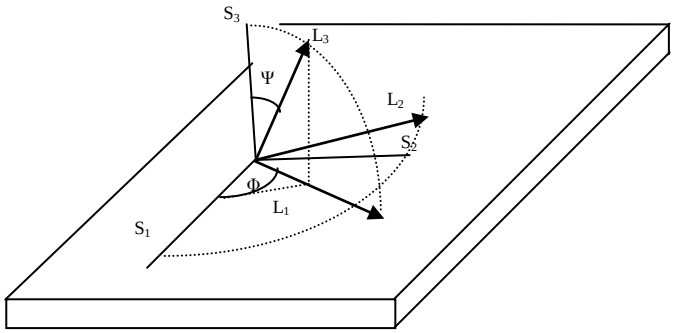

Fig.15: Definition of the sample system (S_i) and laboratory system (L_i) in typical diffraction geometry

The two systems can be related by the direction cosines a_{ij} as given by

$$a_{ij} = \cos\left(x'_i, x_j\right) , \tag{4.29}$$

where the primed variables relate to the laboratory coordinate system L_i and the unprimed to the specimen coordinate system S_i, following the convention established by Dolle [124], and x is a general direction. In full, the direction cosines are given by the following matrix

$$\begin{pmatrix} \cos\varphi\cos\psi & \sin\varphi\cos\psi & -\sin\psi \\ -\sin\varphi & \cos\varphi & 0 \\ \cos\varphi\sin\psi & sin\varphi\cos\psi & \cos\psi \end{pmatrix} . \tag{4.30}$$

For a particular grain oriented in a direction, defined by the angles φ and ψ, which satisfies the Bragg condition, the estimated strain in that direction as measured in the laboratory coordinate system L_i is

$$\left(\varepsilon'_{33}\right)_{\phi\psi} = \frac{d_{\varphi\psi} - d_0}{d_0} = a_{3k}a_{3l}\varepsilon_{kl} . \tag{4.31}$$

Substituting the direction cosines in equation 4.31 leads to the following expression

$$\left(\varepsilon'_{33}\right)_{\phi\psi} = \frac{d_{\varphi\psi} - d_0}{d_0} = \varepsilon_{11}\cos^2\phi\sin^2\psi + \varepsilon_{12}\sin 2\phi\sin^2\psi + \varepsilon_{22}\sin^2\phi\sin^2\psi + \varepsilon_{33}\cos^2\psi + \varepsilon_{13}\cos\phi\sin 2\psi + \varepsilon_{23}\sin\phi\sin 2\psi \quad . \quad (4.32)$$

This is the fundamental equation of X-ray strain determination [12, 92]. It is a linear equation in six unknowns, and may, in principle, be solved exactly by measuring $d_{\varphi\psi}$ along six independent directions. In practice, because of statistical uncertainty, more than 6 measurements are required.

Once the strains have been determined, the stress in the sample coordinate system can be calculated using Hooke's law

$$\sigma_{ij} = C_{ijkl}\varepsilon_{kl} \ , \quad (4.33)$$

where C_{ijkl} are the elastic stiffness coefficients and are referred to the sample coordinate system. The stress in other coordinate systems may be determined from the transformation rule for second rank tensors;

$$\sigma'_{ij} = a_{mi}a_{nj}\varepsilon_{ij} \quad (4.34)$$

where a_{mi} are the appropriate direction cosines.

In the most general case, of an anisotropic material, the stress is a general symmetric triaxial tensor

$$\sigma_{ij} = \begin{pmatrix} \sigma_{11} & \sigma_{12} & \sigma_{13} \\ \sigma_{12} & \sigma_{22} & \sigma_{23} \\ \sigma_{13} & \sigma_{23} & \sigma_{33} \end{pmatrix}, \quad (4.35)$$

and the strains in the sample coordinate system can be expressed in terms of stresses by the inverse of equation 4.33

$$\varepsilon_{ij} = S_{ijkl}\sigma_{kl} \, , \quad (4.36)$$

where S_{ijkl} are the elastic compliances. If the material under investigation is assumed to be isotropic, the above equation becomes

$$\varepsilon_{ij} = \frac{1+\nu}{\mathrm{E}}\sigma_{ij} - \delta_{ij}\frac{\nu}{\mathrm{E}}\sigma_{kk} \, , \quad (4.37)$$

and subsequently

$$\sigma_{ij} = \frac{\mathrm{E}}{1+\nu}\varepsilon_{ij} + \frac{\nu \mathrm{E}}{(1+\nu)(1-2\nu)}\delta_{ij}\varepsilon_{ij}, \tag{4.38}$$

where ν and E are Poisson's ratio and Young's modulus respectively. Substituting the direction cosines in equation (4.37) we obtain the following expression for strain in an isotropic medium

$$\begin{aligned}\varepsilon_{\phi\psi} = (\frac{1+\nu}{\mathrm{E}})([\sigma_{11}\cos^2\phi + \sigma_{12}\sin 2\phi + \sigma_{22}\sin^2\phi]\sin^2\psi \\ +\sigma_{33}\cos^2\psi + [\sigma_{13}\cos\phi + \sigma_{23}\sin\phi]\sin 2\psi) - \frac{\nu}{\mathrm{E}}[\sigma_{11}+\sigma_{22}+\sigma_{33}]\end{aligned}. \tag{4.39}$$

By replacing the constants $-\frac{\nu}{\mathrm{E}}$ and $\frac{1+\nu}{\mathrm{E}}$ with (*hkl*) specific X-ray elastic constants S_1 and $S_2/2$ respectively [92] this equation becomes

$$\begin{aligned}(\varepsilon^{'}_{\phi\psi}) = \frac{1}{2}S_2([\sigma_{11}\cos^2\phi + \sigma_{12}\sin 2\phi + \sigma_{22}\sin^2\phi]\sin^2\psi \\ +\sigma_{33}\cos^2\psi + [\sigma_{13}\cos\phi + \sigma_{23}\sin\phi]\sin 2\psi) + S_1[\sigma_{11}+\sigma_{22}+\sigma_{33}]\end{aligned}. \tag{4.40}$$

For polycrystalline material, where at least *6* independent directions can be measured, this equation predicts two main behaviours. The most common is a linear dependence on $\sin^2\psi$ if σ_{13} and σ_{23} are zero, as discussed in the next section.

2.2.3 Sin²ψ Technique for Stress Determination

Conventional X-ray diffraction stress measurement is confined, by the shallow penetration of the x-rays to the near surface region of the sample. The stress state therefore can be seen as a biaxial surface state, which means that the principal stress σ_1 and σ_2 exist in the plane of the surface, and the stress perpendicular to the surface is assumed to be zero, which is in agreement with the boundary conditions on force at a free surface. In the fundamental equation for stress determination this means that all σ_{ij} components are set to zero for $i,j = 3$ and the equation reduces to

$$(\varepsilon^{'}_{\phi\psi}) = (\frac{1+\nu}{\mathrm{E}})([\sigma_{11}\cos^2\phi + \sigma_{12}\sin 2\phi + \sigma_{22}\sin^2\phi]\sin^2\psi - \frac{\nu}{\mathrm{E}}[\sigma_{11}+\sigma_{22}]. \tag{4.41}$$

Setting $\sigma_\phi = \sigma_{11}\cos^2\phi + \sigma_{12}\sin 2\phi + \sigma_{22}\sin^2\phi$, the above equation (4.41) can be written as

$$\left(\varepsilon'_{\phi\psi}\right) = \frac{1+\nu}{E}\sigma_{\phi}\sin^2\psi - \frac{\nu}{E}\left[\sigma_{11}+\sigma_{22}\right]. \qquad (4.42)$$

This is a linear equation predicting a straight line in $\sin^2\psi$, for both $+\psi$ and $-\psi$ and for any given azimuthal angle ϕ. In practice, the shape of the $\sin^2\psi$ curve can be influenced by different factors including the presence of stress gradient in the layer, presence of strong texture, near surface shear stresses normal to the surface or plastic deformation, and also experimental uncertainties may introduce a varying slope [124]. If the elastic constants E, ν and the unstressed plane spacing d_0 are known, the lattice spacing is determined for multiple ψ tilts and a straight line is fitted by a least squares method. The slope of the best-fit line gives the average surface stress σ_{ϕ}, while the intercept gives the sum of the two normal stresses, $\sigma_{11}+\sigma_{22}$, parallel to the surface. This method is generally known as the $\sin^2\psi$ technique.

The $\sin^2\psi$ technique has widely been applied to stress determination in polycrystalline materials. The drawbacks of this method include peak broadening for very fine grained material, the loss of peak intensity as the ψ angle is varied for highly textured material, and the low depth penetration, which can be on a scale equal to the surface roughness. When it is applied to thin films, the method has another disadvantage in that the X-ray beam may not be confined totally within the layer and, therefore, there may be interference with diffraction peaks from the substrate. In most of the cases, the intensity from the coating may be rather weak due the limited amount of coating material, and thus a proper subtraction of the substrate contribution from the measured peak intensity is a necessary requirement.

2.2.4 Residual Stress Determination in a-Si:H

As mentioned in 2.2.1 above, Härting *et al.* [122] were the first group to analyse the biaxial residual stress in *a*-Si:H with synchrotron radiation diffraction using both direct diffraction data and the RDF. The approach used is discussed in detail in the following section, as it is the same approach used, throughout this thesis, to determine the residual stress in as-deposited and illuminated *a*-Si:H layers.

The structure of *a*-Si:H can be deduced from the structure of crystalline silicon, which crystallise in diamond structure, with silicon atoms arranged in perfect Si-Si_4 tetrahedra. It was discussed in chapter II.2 that the amorphous structure is a CRN where the bond length and the bond angle are distorted. Therefore as the short range order is kept in amorphous material, it is expected to have the same building block as crystalline silicon. In the CRN model the atoms are displaced from their equilibrium positions, and therefore the bonds and the bond angle are strained. However, the displacements within the *a*-Si:H are random, and therefore, the strain may assumed to be essentially hydrostatic. In real *a*-Si:H, hydrogen incorporated in the sample was seen to relax the strain in the material [86]. In the context of the CRN, some Si-Si bonds are highly strained and may break leading to randomly distributed dangling bonds. These bonds are electronically and chemically active, and are passivated by hydrogen, reducing the interatomic interaction and hence relaxing the hydrostatic strain.

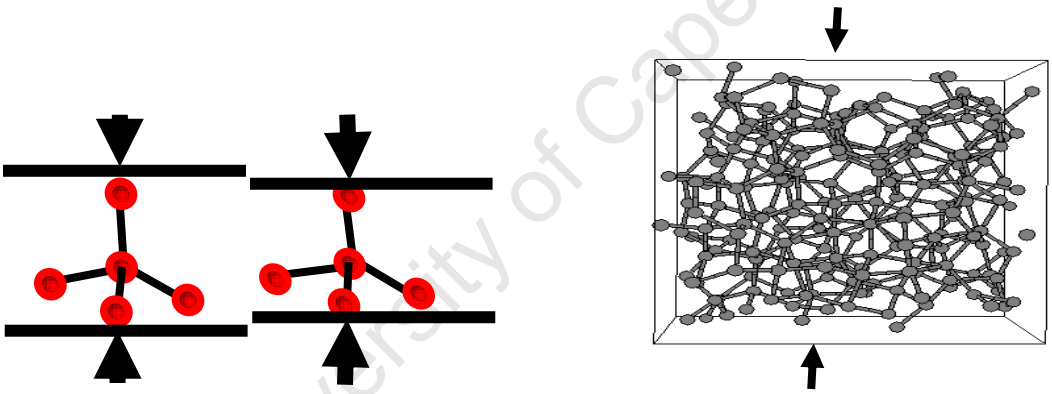

Fig 16: How a compressed tetrahedron may shift the diffraction peak.

As discussed above, in strained polycrystalline silicon, the position of the diffraction peaks will shift, and therefore the stress can be estimated by using equation 4.33. It must be noted that $d_{\varphi\psi}$ and d_0 in this equation, traditionally taken as lattice spacings, can be replaced by any internal spacing measured in an oriented direction *(φ, ψ)*. In determining the strain, and thereafter the stress, Härting *et al.* [122] considered the Si-Si_4 tetrahedron as a fundamental unit in the structure [18]. If the amorphous silicon is strained, the change in height of the tetrahedra should lead to a peak shift in the diffraction pattern if the sample is tilted. The strained Si-Si_4 tetrahedron was therefore used as internal strain gauge as shown in figure 16.

In amorphous silicon we expect the number of peaks to be reduced compared to polycrystalline silicon and due to the absence of long range order in the material the shape of the is broad. A typical diffraction pattern from amorphous material is shown in fig. 17.

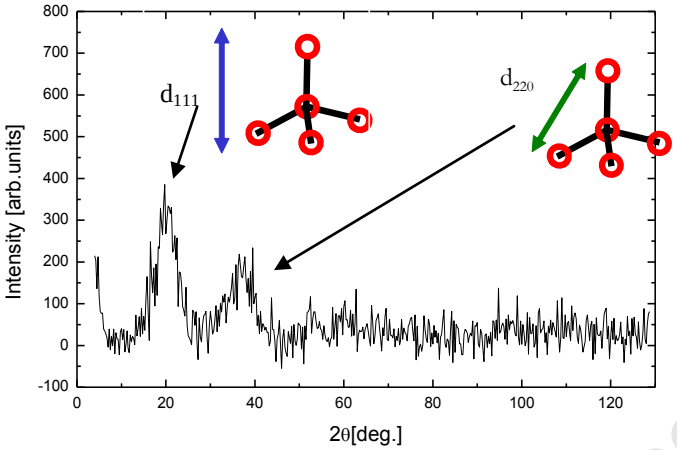

Fig.17: Typical diffraction pattern from *a*-Si:H deposited on a glass substrate showing only two broad peaks, identified with distances in the Si structure.

The first diffraction peak observed in crystalline silicon, and therefore expected in amorphous silicon, is the (111) reflection [9, 18]. As indicated in figure 18(a), the corresponding lattice spacing d_{111} is the height of the tetrahedron. In amorphous silicon however there no lattices planes with separations, only the corresponding average physical distances. Any shift in the first diffraction peak, therefore results from combined effect of both the change in the bond length and the change in the bond angle.

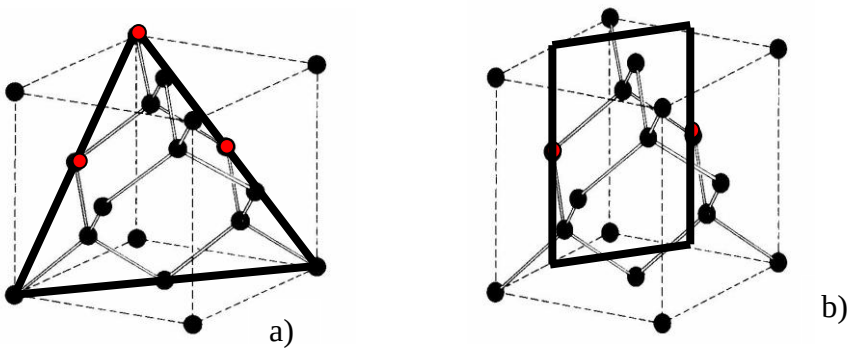

Fig. 18: showing reflecting planes, a) (111) and b) (220), in crystalline silicon structure

The second diffraction peak is equivalent to the (220) reflection from crystalline silicon (fig.18 (b)), and the corresponding lattice spacing d_{220} is exactly half the length of the side of non deformed Si-Si4 tetrahedron. The change in this spacing can therefore be assumed to be dominated by variations in the bond angle. The Fourier transform of the diffraction pattern gives the pair correlation function. The peak shift observed in the reciprocal space may also be reflected in the pair correlation, and therefore strain can be measured also in real space. An example of the pair correlation function is provided in figure 19, indicating the corresponding distances in the Si-Si_4 tetrahedron.

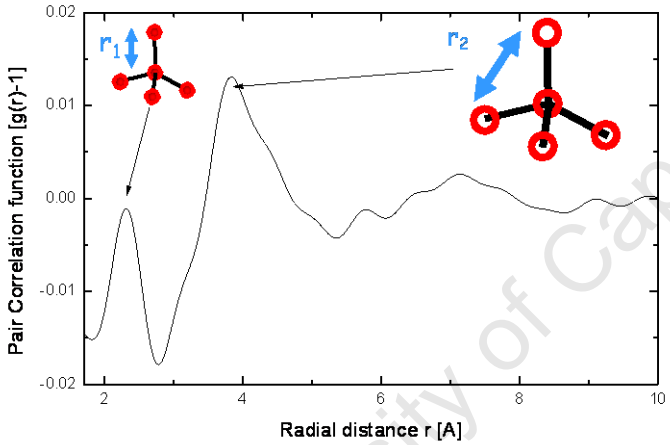

Fig. 19: Typical pair correlation function from *a*-Si:H, showing the identification of the peaks with distances in the Si structure.

The position of the first peak gives a value of the average nearest neighbour distance r_1, and similarly the position of the second peak gives the next nearest neighbour distance r_2. The nearest neighbour separation r_1 is unique in that it yields information on the bond strain, without any contribution strain. These distances and the appropriate elastic constants can be used as references values in determination of strain in real amorphous silicon. It should also be noted that the lattice spacing d_{220} and the distance to the second nearest neighbour, in an ideal tetrahedral amorphous solid, represent the same distance. In real amorphous silicon, however, due to the broadening of the observed peaks, the second diffraction peak may result from the superposition of the (220) and (311) peaks which is avoided in the pair correlation function.

2.3 Experimental Set up for Diffraction Measurements

Synchrotron diffraction measurements were performed on as deposited samples, and after twelve and forty eight hours of illumination time, at the Laboratório Nacional de Luz Síncrotron (LNLS) Brazil, using the 3 axis XPD diffractometer on beamline 10B [125].

Investigation into the structural features of *a*-Si:H was made from the direct X-Ray diffraction patterns, and in more elaborate way using the pair correlation function obtained from the Fourier transform of the diffraction measurements. A direct determination of the first and second peak position of the diffraction pattern associated with the (111) and (220) reflection planes of a crystalline silicon yielded information on the dimensions of the silicon tetrahedron, while the Si-Si pair correlation functions calculated, using a numerical sine transform, provided information on the interatomic separations r_1 and r_2.

2.3.1 Outline of the beamline and diffractometer system

An overview of Beamline 10B is shown in figure 20 [125]. X-rays from a 1.67 T bending magnet of the LNLS ring, operated at 1.37 GeV, are monochromated by a Si (111) double-bounce crystal monochrometer, with water cooling of the first crystal. In the monochrometer the first crystal is flat, and the second one is bent for sagittal focussing [126]. The whole monochrometer system is mounted onto a commercial Huber goniometer, under a ultra high vacuum (typically 10^{-7}mbar), providing good energy stability and reproducibility [125].

beam line 10B

beam size: vertical 1 mm
wavelength resolution: $\frac{\Delta\lambda}{\lambda} = 2.8\times10^{-4}$

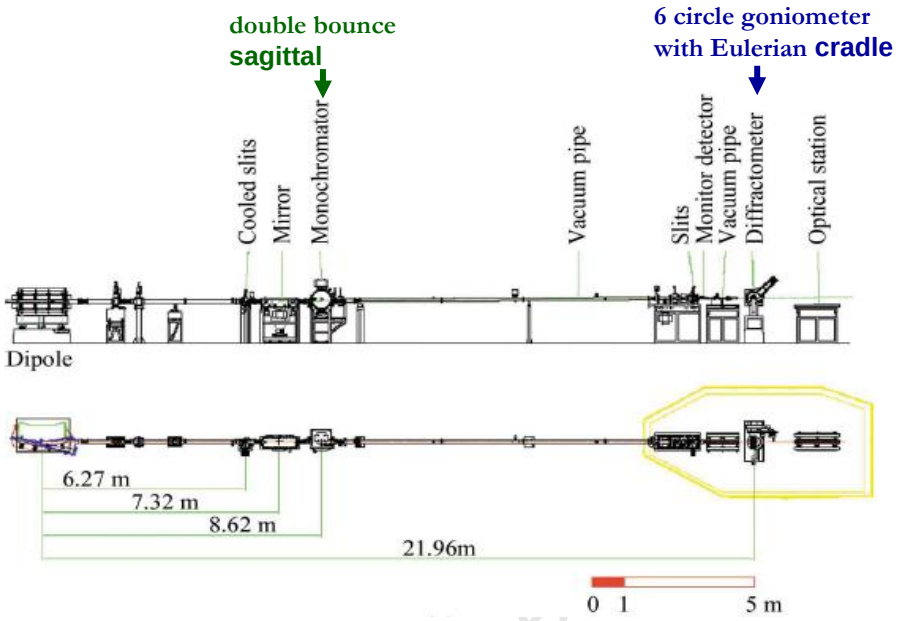

Fig. 20: schematic illustration of the beam line 10B at LNLS [122]

Four sets of four-blade slits are used to define the size of the X-ray beam at the sample position, and the beam entering the detector. The first one is positioned before the mirror and is water cooled. This helps to limit the horizontal and vertical divergence of the incoming white beam. The second set is placed before the diffractometer, and defines the final size of the beam at the sample surface. In our experiment the focused beam size at the sample position was approximately 0.6 cm (horizontal) × 0.4 cm (vertical) at a scattering angle of 4^0. These two sets are computer controlled by the *3-winDCM* software. The two remaining sets of slits are manually operated, and are placed on the 2θ arm of the diffractometer to define the beam entering the detector. The purpose of these is to improve the resolution and to reduce the background due to scattering.

In order to avoid unwanted attenuation and air scattering, a vacuum path with Kapton windows is positioned between the second set of slits and the diffractometer. Another vacuum path is positioned between the sample and the detector, precisely between the scatter slits and receiving slits on the 2θ arm.

The XPD diffractometer used for these measurements is a Huber 4+2 circle diffractometer (fig.21), equipped with Eulerian cradle and located inside the experimental hutch, about 13m away from the monochrometer system. The diffractometer is mounted on table which can be lifted up, or laterally translated, to allow the correct positioning of the X-ray beam at its centre. The minimum angular step of the two theta arm is 0.0001^0.

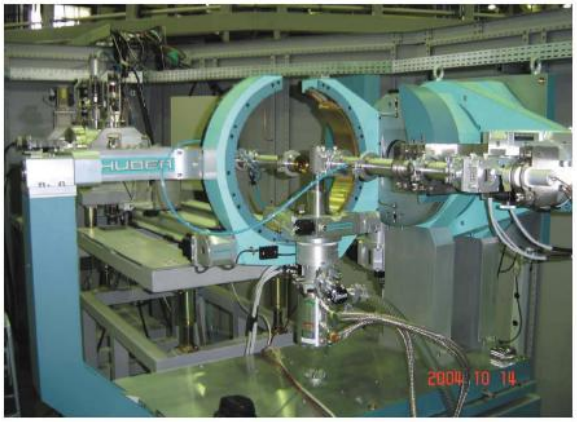

Fig.21: A picture of the Huber 4+2 circle diffractometer equipped with an Eulerian cradle

The diffracted X-ray detection system is a high-throughput Cyber star X1000 (Oxford Danfysik) X-ray detector. This kind of detector can allow for count rates up to 10^6 counts per second, with a very good linear response up to 300,000 counts per second [125]. An X-ray eye, which is a simple high efficiency X-ray sensitive CCD video camera, was used while focussing the X-ray beam to the sample position, but also to check the alignment of the sample with the beam. At the time of our first measurements the typical initial average current was about 270 mA, with a beam lifetime of 20 hrs, but in the second series the lifetime was typically 10 hrs.

2.3.2 Adjustment of the Diffractometer and Sample Alignment

The X-ray powder diffraction beamline at LNLS operates in the energy range between 4.5 and 15KeV. The lower limit is imposed by absorption losses in the Be window, and the upper limit is fixed by the synchrotron source and the cut-off energy of the X-ray mirror. By tilting and translating the monochrometer, and changing its radius using a remotely computer controlled stepping motor, the energy of the X-ray beam was adjusted to 11 KeV, corresponding to a wavelength of 1.125Å. As indicated in figure 22,

this value is a good compromise between the intensity and maximum scattering vector required for the determination of the RDFs.

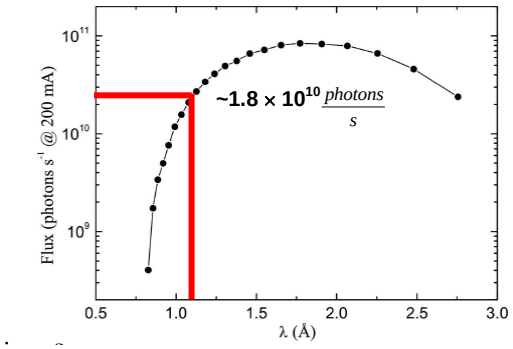

Fig.22. Photon flux of the beamline at the sample position as a function of the wavelength [125].

After setting the beam energy, the next step was to set the beam at the centre of the goniometer. This was achieved with a pin mounted onto an Eulerian cradle. By looking through a telescope, the cross-hairs show if the tip of the pin is at the centre of the goniometer, and if it moves on rotation. Otherwise it must be brought into the centre by moving the goniometer manually. While monitoring the transmitted beam intensity, with an ionisation chamber, the height of the pin was then adjusted until it bisected the beam. The pin was rotated through 180^0 and the count rate checked to see if the top of the pin stays at the centre of the goniometer. Once the adjustment was completed the pin was replaced by the sample.

The samples used in these experiments were 2 cm × 2 cm square samples for the first measurements, which were later cut into four samples of approximately 10 mm × 10 mm for the light soaking experiments and second measurements. Using a double side adhesive tape, the samples were mounted on a 1.5 cm radius Al disc as shown in figure 23 below. The samples were always mounted at the centre of the sample holder with the x-ray beam perpendicular to the edge of the sample for the initial azimuthal angle ϕ=0.

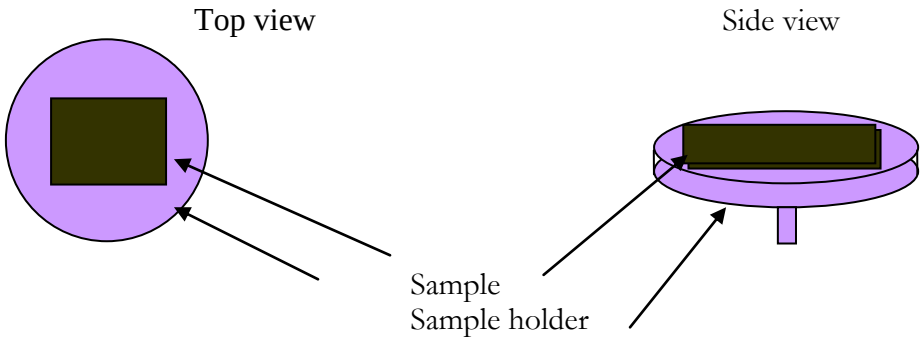

Fig. 23: Layout of the sample and the sample holder for the synchrotron experiment

The sample alignment requires that the sample surface must be parallel to the X-ray beam for at least two perpendicular azimuthal angles, zero and 90^0. This was achieved by rocking the sample through a narrow range of tilt angles while monitoring the count rate. Similarly, the height of the sample in the beam was also adjusted in such a way that the sample cuts a half of the beam in the vertical position when the tube and the detector were moved to zero position. These steps were repeated iteratively until consistent results were obtained.

2.3.3 Data Collection and Treatment

As mentioned before the synchrotron diffraction measurements on as deposited samples, and after twelve and forty eight hours of illumination time, were performed in two series of experiment at the Laboratorio Nacional de Luz Sincrotron (LNLS Brazil), using the 3-axis XPD diffractometer on beamline 10B [125]. The wavelength of the radiation used was 1.125Å, corresponding to the beam energy of 11keV. For stress determination, a full diffraction pattern over a 2θ range of 4^o-129^o in steps of 0.25 was recorded for both as deposited and illuminated samples, and uncoated substrates. Different ψ tilt angles were also chosen: 0, 20, 40, 60, 80, and 85 degrees for the as deposited samples, and the sample deposited at 300°C after illumination. Additional tilt angles of 10 and 30^o were also measured on illuminated samples deposited at 150 and 500°C to make use of a longer beam time allocation. Under these conditions, the maximum scattering vector is $10Å^{-1}$ which is approximately twice that achievable with a conventional X-ray diffractometer, resulting in a better resolution in the pair correlation function.

As raw data, the diffraction patterns need to be processed to remove unnecessary contributions to the scattered intensity, which may result from the sample or the beam geometry. We have identified three sources of unwanted signal which need to be subtracted before any consistent information may be extracted from these measurements. These sources were identified as the substrate contribution in the final signal, the contribution from the primary beam and finally the air scattered radiation reaching the detector. The correction for these sources of error is described below. We can also mention that the glass, in this case, is the best substrate as it has an amorphous character and therefore offers a smooth background with the peaks quite at the same positions as for the deposited layer. However the contribution of the glass substrate into the measured signal is quite significant and the ways of minimizing it may influence the stress state in the layer. A possible way is the thinning of the substrate to reduce this contribution but this will requires us to get a substrate which is as thin as the deposited layer which at the end will relax the stress state in the layer.

(i) Subtraction of the Substrate Contribution

As mentioned above the samples used in this investigation are thin films with thickness of about 2μm, deposited on Corning glass substrates. X-rays, and particularly synchrotron radiation with higher energy, penetrate both the layer and the substrate. Hence the observed scattered intensity is the result of radiation scattered by both the top layer and the substrate. Since the Corning glass used as substrate also has an amorphous diffraction peak, at approximately the same position as the *a*-Si:H, a proper subtraction of the substrate contribution was performed in order to correctly describe the diffraction patterns of the deposited layers.

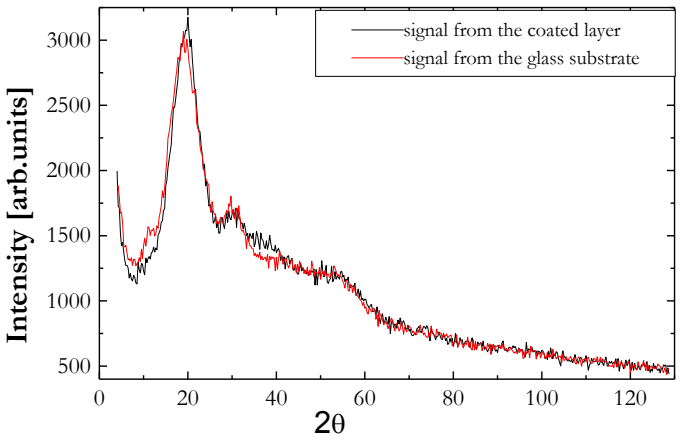

Fig 24: Superimposed plots of synchrotron diffraction patterns for uncoated glass and a-Si:H coated thin film deposited at 300°C

Fig. 24 shows the as-taken diffraction patterns from both the *a*-Si:H sample deposited at 300°C, and an uncoated substrate subjected to the same thermal treatment. It is apparent from this plot that both diffraction patterns are very similar with a large amorphous peak at the same position. From this consideration it can be assumed the contribution from the glass substrate to the diffracted intensity can be up to 99% for normal incidence at low ψ and high θ. For high ψ tilts and lower θ the substrate contribution is less as discussed below which is in a broad agreement with estimates of scattering in the layer obtained from the X-ray penetration depth. Therefore a careful subtraction must be applied in order to keep only the information from the layer.

The principles involved in the substrate subtraction are explained as follows. We assume that there is an exponential loss of intensity as a result of attenuation in the film layer, and consequently the intensity reaching the substrate I_{sub} can be expressed as weighted intensity of the primary beam I_0

$$I_{sub} = \beta I_0 . \tag{4.43}$$

The factor β is a weighting function, taking into account the path of the radiation l through the layer, the linear coefficient of absorption μ, the layer thickness h, the scattering angle θ, and the tilt angle ψ, evaluated as

$$\beta = \exp\left(\frac{-2\mu h}{\sin\theta\cos\psi}\right). \tag{4.44}$$

The linear absorption coefficient was estimated from the mass absorption coefficient in the international tables for X-Ray Crystallography [127] and an approximate density of 2.3 g/cm^3. For *a*-Si:H material, μ was estimated to be 56.935 and 139.38 cm^{-1} for 11KeV synchrotron and X-ray K_α radiation respectively. In this expression we assume that the thin films are isotropic and uniform materials, with a constant refractive index, and also that the radiation has to pass through the layer twice, namely before and after reflection. It can be seen from the above expression that a proper background subtraction depends explicitly on the effective path length *l*, which is a function of the vertical thickness *h* of the sample.

$$l = \frac{h}{\sin\theta\cos\psi}. \tag{4.45}$$

In order to choose a suitable thickness as seen by the X-rays, the following arguments were considered:

- At a suitable thickness, the first two diffraction peaks in the corrected intensity I_{cor} should be symmetrical around their maximum, although the wings need not be symmetrical. This implies that the position of the peak must correspond to the median of a suitable Gaussian curve fit fitted to the peak.
- Assuming a uniform background in both patterns, the signal to noise ratio at high 2θ should be around zero. This means that at the appropriate thickness, the noise in the corrected intensity must be very similar to the characteristic instrumental background.

The effective thickness was allowed to vary between samples to account for slight variations in the mass density, but it was kept constant for each set of data. In all cases it was found to be comparable to the thickness estimated from by UV absorption spectroscopy. A typical illustration of the effect substrate of contribution subtraction on the intensity spectrum is shown in figure 25 below.

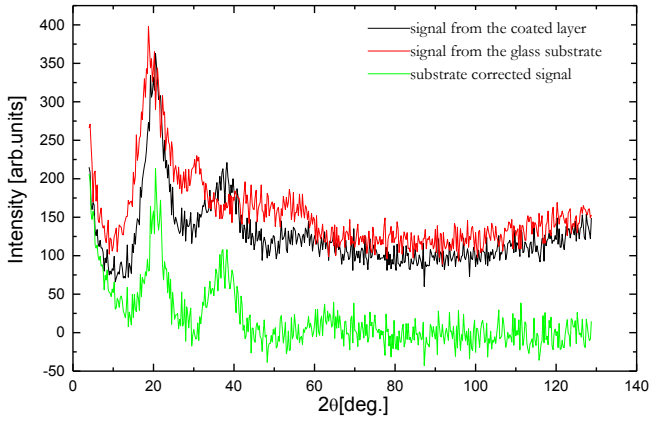

Fig 25: Typical substrate corrected synchrotron diffraction pattern for a-Si:H sample for the zero azimuth and ψ tilting. The sample is grown on glass substrate at 150°C using pure silane as the reactive gas.

It was noticed that as the sample was tilted, the shape of the diffraction peak was becoming more resolved as the tilt angle was increased. This behaviour does not contradict what we expect in polycrystalline material where broad peaks are observed at a higher ψ, because in our case, at a higher ψ tilts the radiation is mainly probing the top amorphous silicon layer, and consequently the contribution from the substrate is weaker. In contrast, a quite weak intensity was observed at lower ψ tilts due to the strong contribution from the substrate.

(ii) Subtraction of the Primary Beam Contribution

It can be seen from the above-corrected intensity, that at a very low scattering angles the diffracted intensity is high and decreases almost exponentially as the angle increases. We attributed this to the primary beam entering the detector without being scattered. Depending on the geometry of the beam and the sample, and the profile of the primary beam, its contribution to the final signal changes with ψ tilting. We have used the following phenomenological function to subtract the effect of the primary beam from the diffraction pattern, keeping in mind that this effect decreases as the scattering angle increases.

$$E = A\exp(-(2\theta - x_0)/m) \ , \tag{4.46}$$

where A, x_0 and m are arbitrary constants depending on the shape of the primary beam contribution and the ψ tilt. The final signal is then

$$I_{cor} = I_f - \exp(\frac{-2\mu h}{\sin\theta\cos\psi})I_0 - A\exp(-(2\theta - x_0)/m)\,, \qquad (4.47)$$

including contributions from both the substrate and primary beam. Fig 26 shows the previous substrate subtracted intensity after being corrected from the primary beam contribution.

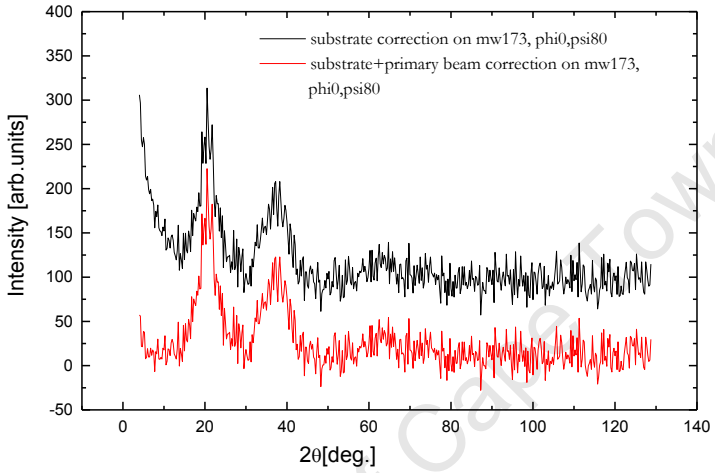

Fig 26: Example of substrate and primary beam corrected synchrotron diffraction pattern for an *a*-Si:H sample. The sample is grown on a glass substrate at 150^{0}C using pure silane as reactive gas.

(*iii) Subtraction of the Air Scattering Contribution*

Radiation scattered by the air may reach the detector and contribute to the final measured intensity. This effect was mainly observed for low ψ angles, and increases as the angle 2θ increases, resulting in increased intensity at a higher scattering angle. The shape of this contribution changes for different tilt angles, but can be approximated by a linear background with a different slope. Figure 27 below illustrates the effect of subtraction on the measured diffraction pattern.

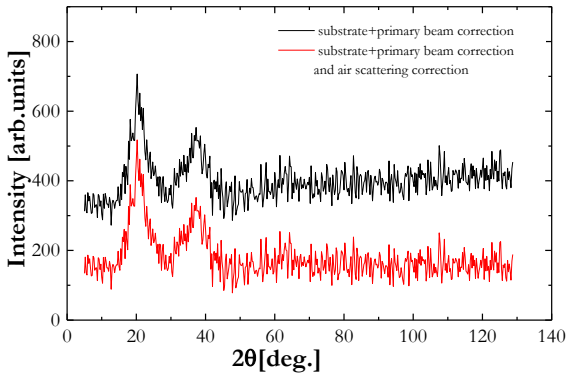

Fig 27: Example of substrate, primary beam and air scattering corrected synchrotron diffraction pattern for a-Si:H sample, grown on a glass substrate at 150^{0}C using pure silane as the reactive gas. The curves have been shifted for clarity

It can be seen from the spectrum that the sample is indeed amorphous, as the diffraction yields diffuse diffraction peaks characteristic of amorphous material. The two clear peaks are indications that the layers under investigation are not disordered in a statistical way but a certain order hold on small scale. It means that the interatomic distances fluctuate around a mean value hence diffraction planes are somehow distorted but constructive interferences are still possible.

2.3.4 Determination of the Pair Correlation Function

In general the diffraction patterns are presented in the form of scattered intensity as a function of the scattering angle 2θ. However, the scattering angle is related to the scattering vector k,

$$k = \left(\frac{4\pi}{\lambda}\right)\sin\theta\,, \tag{4.48}$$

in a given direction in the sample. To determine the Si-Si pair correlation function, the raw intensity data must be expressed as a function of the scattering vector k. The data are then normalized with the atomic form factor, because of its dependence on the scattering vector. Finally the normalized data are Fourier transformed, from reciprocal space to real space, to generate a pair correlation function as described in chapter 2.1.2. It must be noted that a well defined peak in reciprocal space results in weakly resolved peak in real space and

vice versa. The peaks in the pair correlation function are associated with a high 2θ range, while the oscillations at a high scattering vector are representative of the short range order. Once the peak positions are identified, the strain can be determined as shift in the peak position, and using the $\sin^2\psi$ method, the stress can be calculated.

2.3.5 Peak Position and Estimated Error

Different peak determination possibilities are available [110]. These include the gravity method which computes the centre of gravity of diffraction peak above a defined threshold, the parabolic method which approximates the region around the peak position as parabola, and least square fitting of a mathematical function. Common functions which are used include Gaussian, Lorentzian or pseudo-Voigt functions [93].

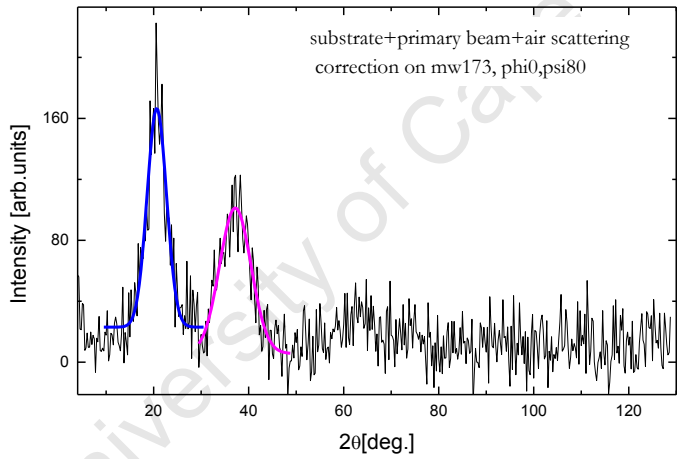

Fig28: Smoothed synchrotron diffraction pattern and Gaussian fits for an *a*-Si:H sample for the zero azimuth and 80^0 ψ tilt. The sample is grown on a glass substrate at 500°C using pure silane as reactive gas.

Both diffraction peaks and the real space peaks in the pair correlation function have an approximate Gaussian shape, and so the Gaussian fit appears to be the best choice. Fig. 28 shows an illustration of the diffraction pattern with the fitted Gaussian curves superimposed on it

The peak positions determined using the Gaussian fit were converted to the interatomic separations. The error in the peak position propagates to an error on the strain, because the broadening of the peaks results from the strain. The errors in the interatomic distances were calculated assuming a normal statistical distribution and unweighted fit was

applied to determine the peak position and width. Hence, this treatment does not include the propagation of statistical errors. The standard deviation σ_d is related to the full width at a half maximum (FWHM) for a Breit-Wigner distribution by the following expression

$$fwhm = 2\sigma_d\sqrt{2\ln 2}\,, \tag{4.49}$$

and the standard deviation is deduced from the expression

$$\Delta(2\theta) = \frac{\sigma_d}{N}\,, \tag{4.50}$$

where N is the area under the peak and $\Delta(2\theta)$ the error in two theta. The previous equation can be rewritten as follows

$$\Delta(\theta) = \frac{1}{2}\frac{\sigma_d}{\sqrt{N}}\,. \tag{4.51}$$

Equating (4.50) and (4.52) leads to the following expression for the error

$$\Delta(\theta) = \frac{fwhm}{4\sqrt{2N\ln 2}}\; or \Delta\theta = 0.212\left(\frac{fwhm}{\sqrt{N}}\right). \tag{4.52}$$

But differentiating the Bragg equation yields

$$\Delta d = -d\cot(\theta)\Delta(\theta)\,. \tag{4.53}$$

Therefore, the error on the strain is

$$\Delta\varepsilon = \left(\frac{\Delta d}{d}\right)_{\phi\psi} = -0.212\cot(\theta)\left(\frac{fwhm}{2\sqrt{N}}\right). \tag{4.54}$$

A similar procedure, without the conversion from angle to distance, was also undertaken to calculate the errors on the strain determined from the position of the pair correlation peak.

Despite the excellent quality of the data as discussed so far, systematic errors need to be considered and an additional discussion of how these were evaluated is presented below:

- The primary source of errors in every stress determination experiment is the alignment of the diffractometer [110]. As previously discussed in the alignment

section, the equipment used is a (4+2) circle high resolution XPD diffractometer regularly used for grazing incidence measurements. The alignment was checked by measuring a stress free silicon powder sample. The plot of $\sin\theta$ vs $\sin^2\psi$ for the (220) reflection is shown in fig.29. It can be seen that within errors the measured lattice spacing is constant, and therefore the alignment is good.

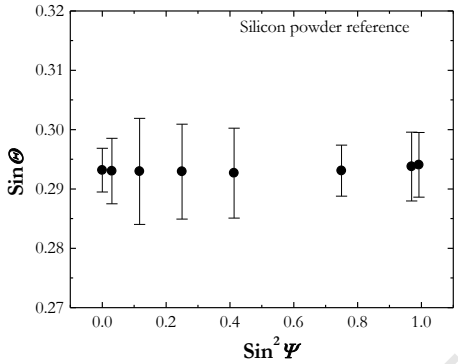

Fig.29: $\sin\theta$ vs $\sin^2\psi$ plot for a stress free silicon powder used as a reference to check the alignment.

- A second issue is that in amorphous material, strain measurement and therefore stress determination is believed to be less reliable than in crystalline materials. The uncertainty in the peak position leads to large statistical errors which are already included in the data analysis.

- A third source of statistical errors results from the low intensity of the sample signal compared to the substrate signal. However as seen in section III.2.3.3, after the subtraction of the substrate signal, clear and well resolved scattering peaks are visible.

- A fourth source of error comes from the sample, in that it may be heterogeneous on the scale of the X-ray diffraction beam. As discussed in section III.2.3.1 a large beam spot was used to illuminate the sample and the reflected beam was collimated to ensure that the beam entering the detector is scattered from the same area of the sample.

2.4 Synchrotron Diffraction Results and Discussion

As described above the analysis of the synchrotron diffraction measurements performed on our samples, either as deposited or after different illumination times, were conducted in two different approaches. In the first approach the positions of the first and second diffraction peaks in the direct diffraction patterns were determined using a Gaussian fit to the background subtracted and smoothed diffraction patterns. These positions were converted to interatomic distances d_{111} and d_{220}, which were converted to strain relative to the values for perfect crystalline silicon. Finally the principal stress components were deduced using the $\sin^2\psi$ method with appropriate values for the elastic constants of 100 GPa for E and 0.22 for ν [44].

In the second approach the Si-Si pair correlation functions were extracted, using a simple numerical sine transform, from the direct diffraction pattern for each ψ tilt and azimuth rotation φ after background correction. Similar to the first approach, the positions of the first and second peaks in the radial distribution function were determined using a Gaussian fit, and therefore the first and second nearest neighbour interatomic distances r_1 and r_2 were estimated. These distances were then converted to strain and stress using the expected values from crystalline silicon. In this approach the correction for atomic scattering factor has been applied using the standard data for silicon [127]. The effect of illumination for 12 and 48 hrs on the microstructure and therefore on the residual strain and stress were also investigated using both approaches, namely the direct diffraction and the pair correlation function.

2.4.1 Structural Information on *a*-Si:H in Reciprocal Space

Representative diffraction patterns for three samples in as deposited conditions are shown in figure 30. For this example, the azimuth angle was chosen to be zero, while a high tilt angle was chosen to minimize the contribution from the substrate. The scans have been shifted upwards for clarity.

It can be noticed that, within the temperature range used for deposition, the structure of the layers remains amorphous as they only present two clear broad peaks at

approximately 2 and 3.5Å^{-1} , and a reduced intensity at a high scattering vector associated with the absence of long-range order. Due to fluctuations in the bond angle and length inherent to amorphous material, the peaks become broader as the scattering vector increases. Thus the background overshadows a broader third peak with very weak intensity.

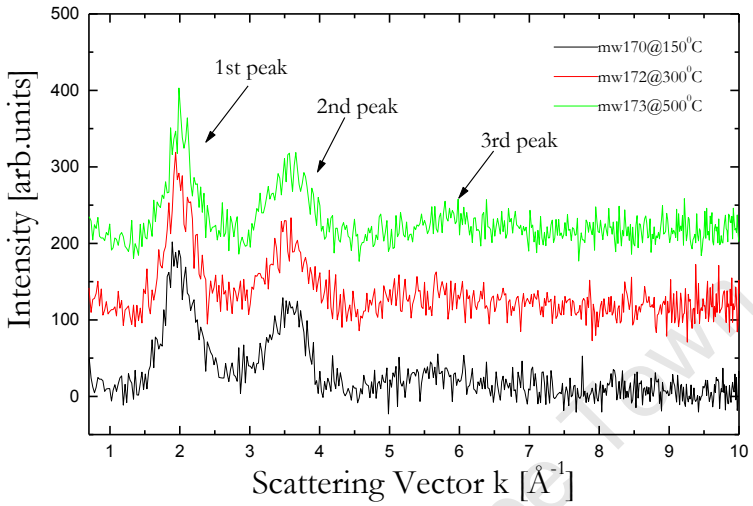

Fig.30: Diffraction patterns from *a*-Si:H samples deposited at different temperature between 150 and 500^{0}C

As discussed in the chapter II.1, the structure of *a*-Si:H is derived from the crystalline silicon structure by slightly changing the bond length and distorting the bond angle. Consequently, indications of some other peaks can also be identified in the diffraction patterns. A small peak, between the two main peaks, at around 2.8 Å^{-1} may be the equivalent of what can be the (211) peak in an fcc structure. This peak is not visible in the *c*-Si diffraction pattern because of destructive interference. However, due to either hydrogen substitution or distortion in the bond length and angle, the interference may not be completely destructive, and a small peak is seen close to either the first or second peak depending on the tilt angle or the deposition temperature. The (311) peak located at 3.84 Å^{-1} in the *c*-Si diffraction pattern is, in the case of amorphous material, completely mixed with the (220) situated at 3.27Å^{-1} due to the broadening of the amorphous peak. The small peak appearing on the right side of the second broad peak, for low temperature deposition, may be the equivalent of the (400) peak situated at 4.63 Å^{-1}.

A further analysis of the position of the peaks obtained by the Gaussian fit revealed that the average distances d_{111} for the three samples are respectively 3.16±0.01Å,

3.21±0.01, and 3.20±0.02Å, while the lattice spacings d_{220} are 1.77±0.01 Å, 1.80±0.01 Å and 1.81±0.01Å. These values are comparable with the values of *c*-Si, namely 3.135Å and 1.920Å respectively. This confirms the fact that the structure of amorphous silicon can be deduced from the structure of *c*-Si distorted in the bond length and the bond angles.

Also a shift in peak position was observed as the sample surface was tilted through different ψ angles. Figure 31 below illustrates the peak shift in the diffraction pattern with ψ tilting

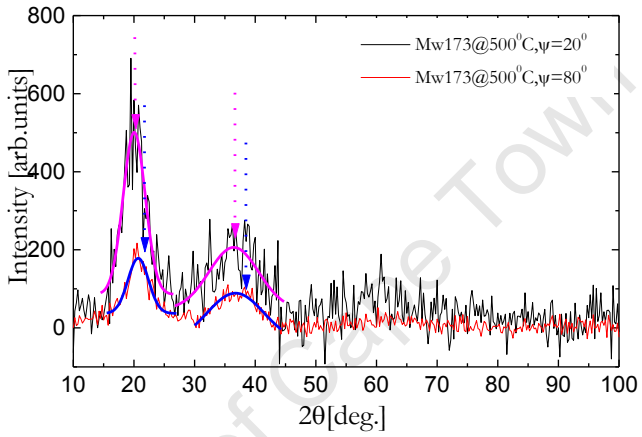

Fig. 31: Diffraction peak shifted as the sample surface is tilted from 20 to 80⁰. the a-Si:H layer is deposited at 500⁰C.

This variation in the interatomic distances associated with the ψ direction was converted into strain, and, with appropriate elastic constants, the stress in the sample can be calculated.

2.4.2 Strain Variation and Residual Stress in Reciprocal Space

As mentioned before the changes in internal distances with different ψ orientation of the sample surface were converted into lattice strain using the interatomic distances for crystalline Silicon as a reference. We recall that the first diffraction peak in *a*-Si:H is comparable to the (111) reflection peak in the *c*-Si structure, and that the interplanar distance d_{111} is the equivalent perpendicular height of the Si-Si_4 tetrahedron from which the

amorphous network is built. The second peak corresponds to the (220) reflection and the interplanar spacing d_{220} is equal to equal to the length of side of the basic tetrahedron.

a) Strain variation in reciprocal space

Figure 32 below illustrates the strain variation with $\sin^2\psi$ for the sample grown at 500^{0}C, as determined from the position of the first diffraction peaks, for one of the six different azimuthal rotations measured. As can be seen from the sin$^2\psi$ plots, the strain in the sample changes with different ψ-orientations of the sample surface, and the observed behaviour is consistent for different ϕ-rotations.

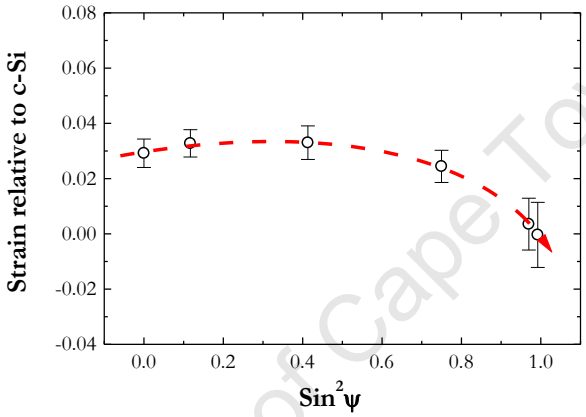

Fig. 32: The sin$^2\psi$ plot illustrating the strain variation in *a*-Si:H sample deposited at 500^{0}C for one ϕ rotation.

By rotating the sample surface we may expect to investigate different orientations, and therefore different behaviour in the sin$^2\psi$ plots, but there should not be changes in the perpendicular strain, determined for ψ zero. This is not the case with our measurements. As can be seen in the following polar plot (fig.33), the perpendicular strain seems to move around eccentrically.

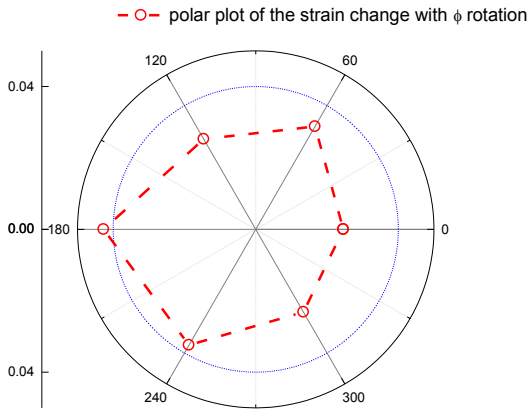

Fig. 33: Perpendicular strain changes, with ϕ rotation, for a sample deposited at 500^{0}C on a glass substrate using pure silane.

Ideally, the perpendicular strain should remain constant, tracing out a circle, when the sample is rotated, which implies that the beam probes exactly the same volume of the sample. This means that the beam profile on the sample must not change in shape or intensity with time, and both the beam and the sample the sample must be symmetric about the rotating axis. In our case, these seem to be the reasons behind this observed behaviour.

If the plot is not at the centre, then the sample is tilted giving a ϕ dependent constant error in θ. This is the main source of error in figure 33. In the polar plot the displacement vector of the centre of the circle indicates the direction in which the sample is tilted. In the case shown, the sample is tilted approximately along the $\phi = 0$ direction, *i.e.* about an axis in the $\phi = 90^0$ direction.

An elliptical, or more complicated, locus can result from the beam probing different areas of the sample as it is rotated. The cause of this can be a slight misalignment between the goniometer axes and the beam [128], or a non uniform beam profile. When performing our measurements, the duration period to complete one measurement was around 10 hrs. It is therefore probable that the beam profile on the sample changed with time, because the beam intensity was decreasing, reaching about a third of its initial intensity before the next electron injection. In this case, the instrumental shift is compounded by any inhomogeneity in the sample microstructure. This may be related to

the relative orientation of the filaments and the substrate in the deposition chamber, or to the direction of the flow of the reactive gas inside the deposition chamber.

For the first diffraction peak, the behaviour of the $\sin^2\psi$ plots does not reflect a true linear dependence when all different azimuthal rotations are taken into account. Considering the individual plot, shown in figure 31, a straight line can be fitted, which has a negative gradient, and therefore a compressive stress state in the plane of the layer. However, a close look at all ϕ rotations, in the Appendix, shows that a curve can better fit the data. This deviation from the linear dependence, predicted by the $\sin^2\psi$ method, was taken as an indication of the presence of a non-biaxial stress state, and consequently a gradient in the stress [129]. Similar behaviour was reported in previous work on *a*-Si:H deposited under similar conditions using both conventional laboratory X-rays [119] and synchrotron radiation [122].

As discussed above, for low ψ tilting the X-rays penetrate deep in the sample, and therefore the information gathered can be related to the region around the interface between the substrate and the layer. At high ψ tilts the X-rays probe a shallow region near the sample surface. The two regions can easily be identified from these $\sin^2\psi$ plots. For $\sin^2\psi < 0.75$, this region present a low stress gradient compared to the region where $\sin^2\psi > 0.75$, which shows a high curvature. Strain within these regions will be discussed bearing in our mind that the strain in thin films results from a thermal mismatch contribution and intrinsic strain. We expect the thermal mismatch contribution to be more significant in the region close the interface between the substrate and the layer while the intrinsic strain is more significant at the sample surface. For this sample deposited at 500 ^{0}C, all six ϕ-rotations show an increase in strain gradient starting from a low compressive strain near the interface to a higher compressive stress at the sample surface. The change in the strain with $\sin^2\psi$ is the same for all ϕ rotations and this indicates that the near surface stress is identical in all direction.

A parallel analysis for the second diffraction peak is shown in figure 34 for the same sample. The interplanar spacing associated with this peak is equal to the length of side of the basic tetrahedron. Using the interplanar distance d_{220} from the *c*-Si structure the strain, relative to crystalline silicon, in *a*-Si:H can be estimated. Figure 33 shows a typical

$\sin^2\psi$ plot for $\phi = 240^0$. The remaining $\sin^2\psi$ plots for other azimuthal angles are included in Appendices at the end of this thesis, along with those for the other samples.

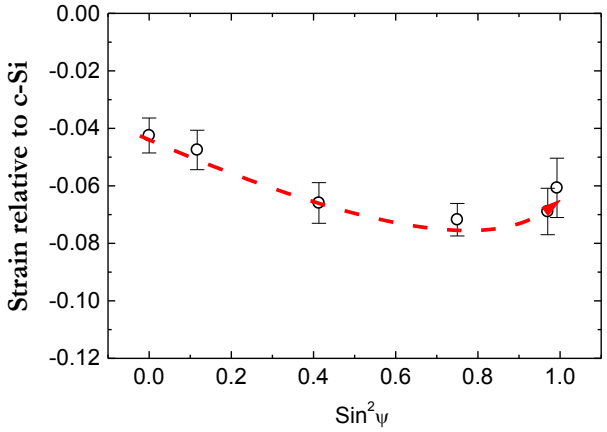

Fig. 34: Typical sin²ψ plot from the second diffraction peak for an a-Si:H sample deposited on glass substrate at 500⁰C

A certain correlation between the behaviour of the $\sin^2\psi$ plots for the two diffraction peaks is expected, as stretching the height of a tetrahedron will result in stretching the sides, even if they may not elongate by the same amount due to changes in the bond angle. It can be seen from this figure that the measured strain becomes more negative as the sample surface is tilted, indicating a compressive strain. In comparison with the first peak, however, the curvature of this plot is reversed. The slopes at the region close to the interface are different, but the slopes over a higher ψ range are the same for both diffraction peaks. This indicates that the intrinsic stress, reflected in the near surface stress, is the same whether we are looking at the height of the tetrahedron or at the edge of the tetrahedron. The same conclusion does not hold at the region close to the interface, where the increase in the height of the tetrahedron is accompanied by a compression of its side and that can only be possible when the bond angle changes significantly.

A similar analysis was applied to the first and second diffraction peaks for the samples deposited at 150 ^{0}C and 300 ^{0}C. In both cases the $\sin^2\psi$ plots do not reflect a true linear dependence. As can be seen in following figures, different deposition temperatures yield different behaviours, but there is a consistent behaviour for each sample with respect to different azimuthal rotations, even if a certain scattering of the data points was observed for the sample deposited at 150^{0}C.

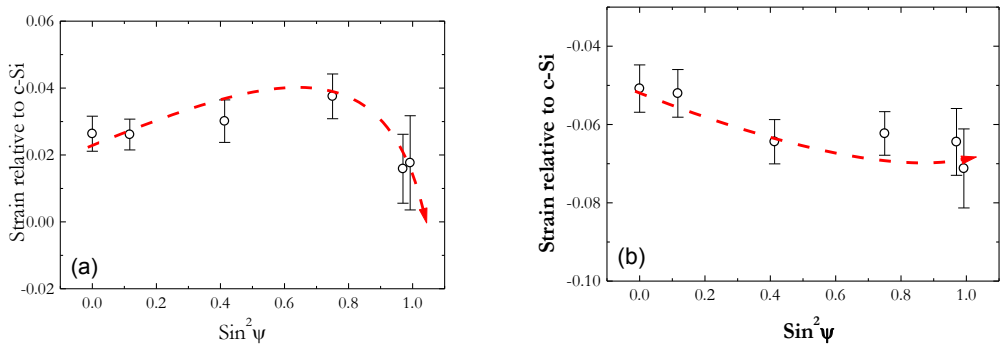

Fig 35: Typical sin2ψ plots for the a-Si:H layer deposited at 300^{0}C: (a) From 1st diffraction peak, and (b) 2nd diffraction peak.

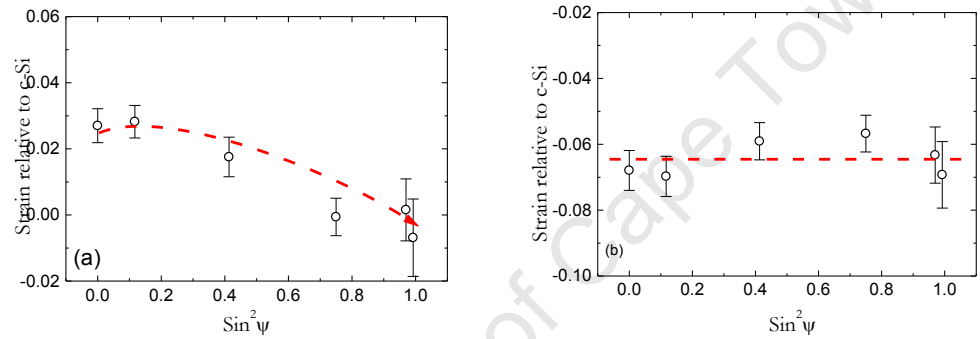

Fig. 36: Typical $\sin^2\psi$ plots for the *a*-Si:H layers deposited at 150^{0}C: (a) 1st diffraction peak, and (b) 2nd diffraction peak

A close look at the $\sin^2\psi$ plots for the layer deposited at 300^{0}C (Fig 35) also reveals two different regions: the region near the interface between the layer and the substrate, where the thermal mismatch is predominant, and the near surface region were the intrinsic stress contributes more towards the total stress. At a low ψ, the first peak exhibits an increasing strain with increase in ψ angle, while the second peak shows a decreasing strain with increasing ψ angle. At a higher ψ angles, the behaviour is reversed in both plots, and the strain at the sample surface is similar. The same behaviour was also seen in the sample deposited at 500^{0}C. This can be seen as an indication that the two samples have similar microstructures, and that the only difference comes from the thermal mismatch as the deposition temperatures are different by 200^{0}C. The first and second diffraction peaks for the sample deposited at 300 ^{0}C show a general compressive strain with

the edge of the tetrahedron more compressed than its height. The edge of tetrahedron in the near surface region is almost unstrained.

The sample deposited at 150 ^{0}C behaves quite differently from the others. The first diffraction peak shows change in the strain with ψ tilting. The strain gradient changes from low tensile, at low $\sin^2\psi$, to a higher compressive stress but with a lower slope than the one for the sample deposited at 500 ^{0}C. The two regions identified in the previous samples can also be found in this sample, but not as clearly defined as in the other samples. A ψ-splitting is observed for this sample deposited at a low temperature, as highlighted in figure 37 below. The ψ-splitting effect is associated with the presence of shear stress components, σ_{13} and σ_{23}, in the depth, leading to a sin2ψ dependence in the fundamental equation for stress determination.

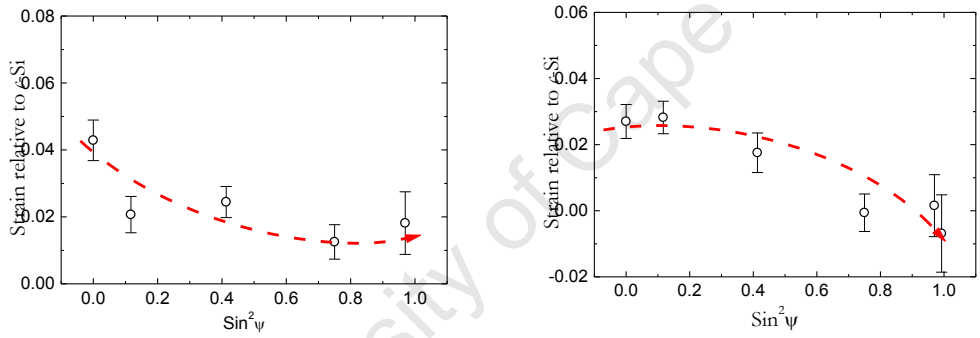

Fig. 37: $\sin^2\psi$ plots for two ϕ with a 180^0 rotation, showing the ψ-splitting effect in the *a*-Si:H sample deposited on a glass substrate at 150^{0}C.

From the first and second peaks in direct diffraction patterns, which are the equivalent to the (111) peak and (220) in *c*-Si, for as deposited a-Si:H samples it can be seen that different deposition temperatures yield different microstructure, and therefore different strain distributions. This is accounted for by a difference in thermal expansion coefficients between the amorphous layer and the substrate, on the one hand, but also the difference in intrinsic stress in the very near surface region. As in most cases, the thermal expansion coefficient of the glass is higher than that of the layer, the in plane thermal mismatch stress as given by equation (II.4.16) will be always compressive. The intrinsic stress, resulting from numerous transformations such as film densification during the deposition, lattice mismatch, vacancies and interstitial diffusion can also account for the

observed differences well. Samples grown at 300 and 500 ^{0}C show a similar microstructure with only a difference in the thermal stress contribution around the interface between the layer and substrate. The sample deposited at a low temperature differs from the others, not only from the thermal contribution, but also the intrinsic contribution is totally different. This is an indication of a totally different microstructure which can be explained by, amongst other parameters, the hydrogen configuration and content in this sample, as it is known to play a significant role in shaping the microstructure of the thin layer [63]. Other parameters such as defects and the densification of the sample at a higher deposition temperature must also be taken into account.

b) Residual Stress in Reciprocal Space

The strain and the stress in the sample are related via the generalized Hooke's law (eq. II.4.33), and in the case of hydrogenated amorphous silicon which is assumed to be isotropic, only the two elastic constants, E and ν, which are independent of the coordinate system, are required. Neglecting the slight curvature, in the $\sin^2\psi$ plots, in the first approximation, a linear fit yields, in general, a negative slope and therefore a compressive strain difference between the in plane and normal strain $(\varepsilon_{11}-\varepsilon_{33})$. The following figure illustrates this linear fit for the sample deposited at 300^{0}C.

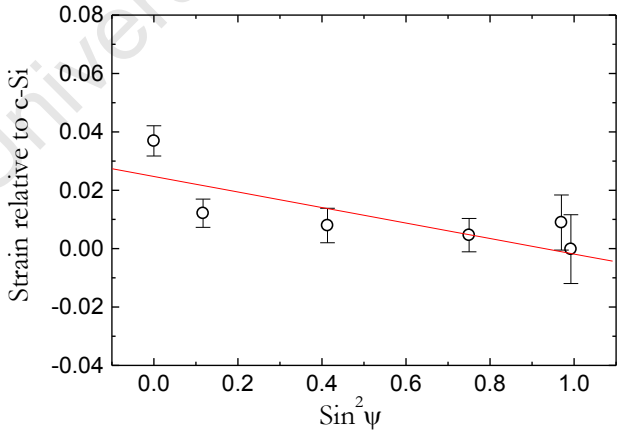

Fig. 38: Linear fit to obtain the gradient used to calculate the stress in the sample used in this study.

The slopes values from these linear fit were used to estimate the residual stress in the sample using the elastic constants $E=100GPa$ and $\upsilon=0.22$ reported previously for

a-Si:H samples grown under similar conditions [44]. We recall that the gradient of the linear fit in the $\sin^2\psi$ method gives the projected stress

$$\sigma_\phi = \sigma_{11}\cos^2\phi + \sigma_{12}\sin 2\phi + \sigma_{22}\sin^2\phi \qquad (4.55)$$

in the azimuthal direction ϕ, and the intercept gives an estimate of the normal stress $\sigma_{11}+\sigma_{22}$. The values of σ_ϕ for the first diffraction peak are shown as polar plots, at the three deposition temperatures in figure 39. The solid circle represents zero stress, $\sigma_\phi = 0$, while the inside the circle is compressive and outside is tensile.

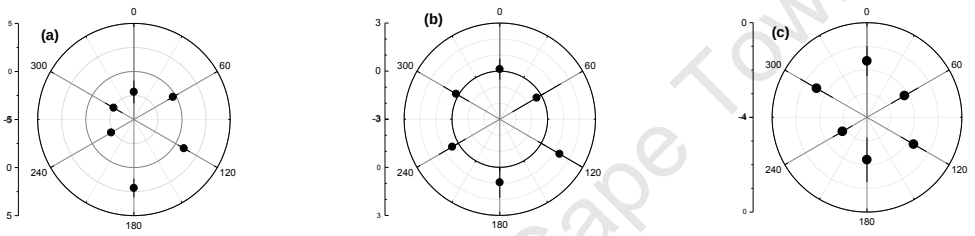

Fig. 39: Stress component σ_ϕ derived from the $\sin^2\psi$ analysis of the first diffraction peak for a-Si:H deposited on Corning glass substrates at: (a)150 ^{0}C , (b)300 ^{0}C, and (c)500 ^{0}C

It can be seen from the polar plots, obtained from the first diffraction peak in reciprocal space that the projected stress changes with the deposition temperature. While the sample deposited at low temperature shows mainly a compressive stress, the stress in the sample grown at 300 ^{0}C is slightly tensile, and finally the stress in the sample at 500 ^{0}C is always compressive. The second observation is that the projected stress is not isotropic for each sample. All the samples show the same trend consisting in a displaced distribution of the stress in a certain direction. The distribution of the stress for the sample deposited at 500 ^{0}C seems to be displaced by 180 degrees relative to the other two, because the orientation of the least compressive stress is towards 330^0, compared to the maximum tensile stress along the direction $\phi = 150^0$ for the other two samples.

Similar polar plots, obtained from the second diffraction peak in reciprocal space are displayed in figure 40 below.

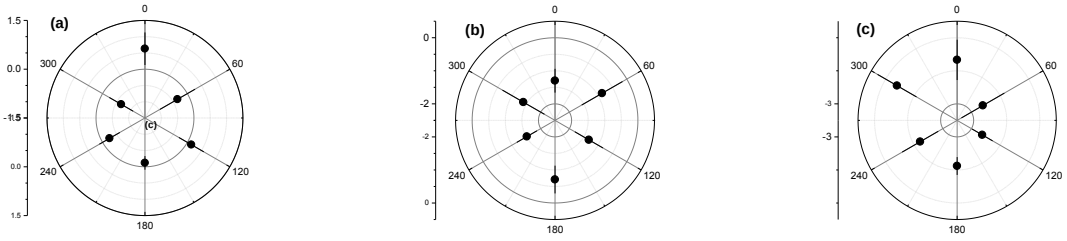

Fig. 40: Stress component σ_ϕ derived from the $\sin^2\psi$ analysis of the second pair correlation peak for a-Si:H deposited on Corning glass substrates at: (a)150 ^{0}C , (b) 300 ^{0}C, and (c) 500 ^{0}C.

The same conclusions from the first diffraction peak hold for the second even if the patterns are less distinct. They all show a compressive stress, which changes with deposition temperature, and the stress distribution is ϕ dependent. It generally appears that, for the second diffraction peak in reciprocal space, the stress is compressive and increases with deposition temperature. It still appears that the sample at 500 ^{0}C is rotated by 180 degrees compared to the other two.

The overall compressive stress increasing with the deposition temperature, observed from the second diffraction peak, is consistent with the thermal stress dominating in the *a*-Si:H layers deposited on glass substrates. This picture is not so clear for the stress estimated from the first diffraction peak in reciprocal space, where the lowest overall stress is seen in the sample grown at 300 ^{0}C. This temperature range is, however, thought to be an optimum growth temperature [44].

Because the stress is anisotropic in the samples analyzed, it is imperative to resolve it into stress components, and possibly investigate its depth dependence. To investigate the depth profile and resolve the stress into components, different methods can be used. A depth profiling model proposed by Härting [129], has been developed for a semi-infinite solid, but cannot be used here because of the finite film thickness, around 2μm. Also, because of errors in the ψ zero points, as indicated in figure 33, any global fit using different ϕ orientations, including this model, would be problematic.

Another depth profiling model, in terms of two stress zones [130] could, in principle be applied. In this model the $\sin^2\psi$ curve is approximated with two regions of different stress: a near-surface region *a* with a thickness *l*, and a deeper region *b* extending from *l* to the layer thickness *L*. This model therefore requires five independent parameters, but for the

first series of synchrotron measurements we only have six data points in each curve, which is not enough to obtain a meaningful fit.

For similar reasons that a global fit for all ϕ is not practical, it is not sensible to use the intercept to determine the normal stress. The best way, therefore, to get the normal stress was to fit equation (4.55) to obtain the three stress components, and combine these to find the normal and principal stresses. The normal stress is simply the sum of the normal components,

$$\sigma_{normal} = \sigma_{11} + \sigma_{22}, \tag{4.56}$$

and the principal stresses are given by a principal axis transformation [92],

$$\sigma_1 = \left(\frac{\sigma_{11}+\sigma_{22}}{2}\right) + \sqrt{\left(\frac{\sigma_{11}-\sigma_{22}}{2}\right)^2 + {\sigma_{12}}^2}, \tag{4.57}$$

and

$$\sigma_2 = \left(\frac{\sigma_{11}+\sigma_{22}}{2}\right) - \sqrt{\left(\frac{\sigma_{11}-\sigma_{22}}{2}\right)^2 + {\sigma_{12}}^2}. \tag{4.58}$$

The estimated stress values from the above fit are given in table 2 below.

Biaxial stress in GPa	1st peak (111)			2nd peak (220)		
	Mw 170	Mw 172	Mw 173	Mw 170	Mw 172	Mw 173
σ_{11}	-2.12±1.91	0.37±0.32	-1.80±0.29	-0.004±0.21	-1.05±0.21	-2.05±0.25
σ_{22}	-0.86±1.29	0.36±0.47	-2.24±0.25	-0.36±0.32	-1.48±0.28	-2.47±0.40
σ_{12}	-1.18±0.98	-0.12±0.40	-0.54±0.20	0.003±0.27	-0.02±0.23	-0.01±0.34
$\sigma_{11+}\ \sigma_{22}$	-2.99±2.31	0.73±0.57	-4.03±1.00	-0.37±0.39	-2.52±0.35	-4.52±0.56
σ_1	-0.15±2.74	0.49±9.78	-1.43±2.24	-0.004±0.27	-1.05±0.25	-2.05±0.67
σ_2	-2.84±2.74	0.24±9.78	-2.60±2.24	-0.36±0.27	-1.48±0.25	-2.47±0.67

Table 2: Residual stresses, in as deposited samples, estimated from the position of the first peak in reciprocal space for all ϕ rotations.

It can be noted that the errors are large, but there are certain visible trends. From the diffraction peak, the normal stress for 150 ^{0}C is slightly compressive, becomes slightly tensile at 300 ^{0}C, presumably because of increased order and less defects, and finally

becomes strongly compressive at 500 ^{0}C, when the thermal mismatch dominates. A similar behavior is also observed in the principal stresses for which the anisotropy also decreases with increasing deposition temperature. For the second peak, there is a continuous increase in compressive stress, in both the normal or principal stresses, as the deposition temperature is increased.

2.4.3 Structural Information on *a*-Si:H in Real Space

The microstructure and local order in amorphous material can be described by a radial distribution function, or pair correlation function, obtained by Fourier transforming the diffraction pattern from reciprocal space. The positions of the peaks in this function are associated with the characteristic distances separating pairs of atoms, and therefore reflect the atomic arrangement within the material. For amorphous material, and particularly *a*-Si:H, characterized by the absence of long range order, the pair correlation function shows only two well resolved peaks at a low scattering vector associated with the short range order, followed by vanishing oscillations related to the medium range order.

A typical example of a pair correlation function, from the synchrotron diffraction measurement carried out on an *a*-Si:H sample, deposited at 500^{0}C on glass substrate using pure silane gas as the reactive gas, is shown in figure 40. We must recall that this curve, typically, represent only Si-Si pair correlations as hydrogen cannot be detected by X-rays.

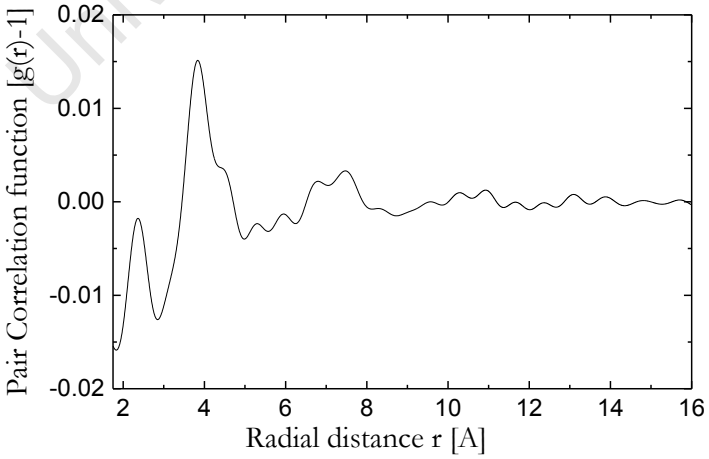

Fig.41: Pair correlation function for a-Si:H sample deposited at 500^{0}C highlighting the amorphous character of our samples.

The plot reveals a very sharp well defined first peak associated with the first nearest neighbour situated at around 2.37 Å, reflecting the well defined local tetrahedral geometry characteristic of *a*-Si:H. This interatomic distance is close to the 2.35 Å bond length in *c*-Si. A much broader second peak occurs at around 3.85 Å. The width of this second peak is associated with the fluctuation in the bond length and distortion of the bonds angles. This also confirms the amorphous character of the sample within the range of deposition temperature we have chosen. Further peaks, with decreasing intensity, are also discernable at higher scattering vector in the Si-Si pair correlation function, representing higher order correlations. The one appearing as a shoulder on the second peak at around 4.5 Å , may be seen as a signature of medium range order. This shoulder most likely result from the overlapping of the second peak with a native and poorly resolved third Si correlation shell, but may also be associated with the presence of hydrogen.

It can be noted that, while the first peak in the pair correlation function does not have an equivalent in reciprocal space, *i.e.* there is no diffracting plane intersecting the nearest neighbour atoms, the second peak has an equivalent in reciprocal space. The interplanar spacing d_{220} from the second diffraction peak in reciprocal space is the same as the second nearest neighbour distance r_2. However in our analysis we have realised that, because of the broadening of the diffraction peak, the (220) peak at 34^0 in *c*-Si and the (311) at 40^0 are mixed to give a peak centred at around 36^0. Also the (400) peak may appear as a shoulder on the high angle side of the second peak. In a similar development, the forbidden (211) peak may appear at a lower angles, if the interference is not completely destructive due to hydrogen substitution or distortion in the bond length or angle. All these peaks contribute to the (220) diffraction peak, but are well separated in the radial distribution function. Therefore the second nearest neighbour distance may not completely reflect the behaviour of the equivalent interplanar spacing d_{220}.

2.4.4 Strain Variation and Residual Stress in *a*-Si:H in Real Space

By tilting the sample surface, different diffraction patterns are recorded. These diffraction patterns will yield different projections of the pair correlation functions corresponding to ϕ and ψ directions. Figure 42 below shows a peak shift in the pair correlation function on tilting the *a*-Si:H sample surface.

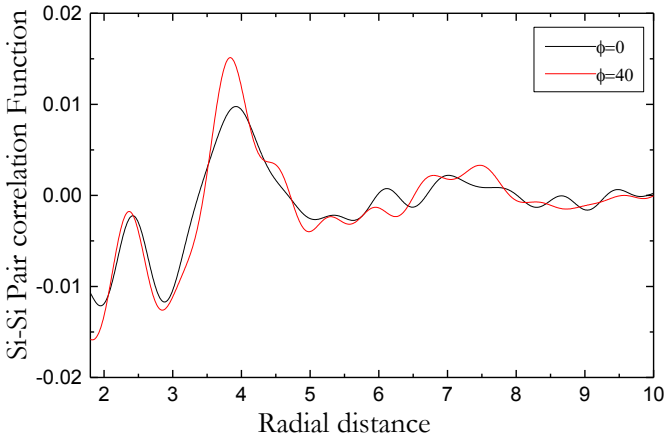

Fig. 42: The shift in the peak position in the pair correlation function as the sample surface is tilted by 40 degrees.

In similar ways as from the shift in the peak position from the direct diffraction patterns, the shift in the peak position, from the Gaussian fit to the pair correlation function, by tilting the sample surface can be converted into strain. The first peak is associated with the nearest neighbour distance, and therefore the shift in the first peak gives the strain associated with the covalent bond. The shift in the second peak associated with the second nearest neighbour separation is mainly informative of the strain resulting from the bond angle distortion.

a) Strain Variation in Real Space

In the following analysis the strain was estimated relative to the *c*-Si interatomic separations. However the equilibrium interatomic distance in *c*-Si may be different to that in the amorphous network, as it depends on the position of other atoms in the network, which is randomly organized. Figure 43 below illustrates the strain relative to crystalline silicon for the nearest neighbour separation in *a*-Si:H sample deposited at 500 ^{0}C.

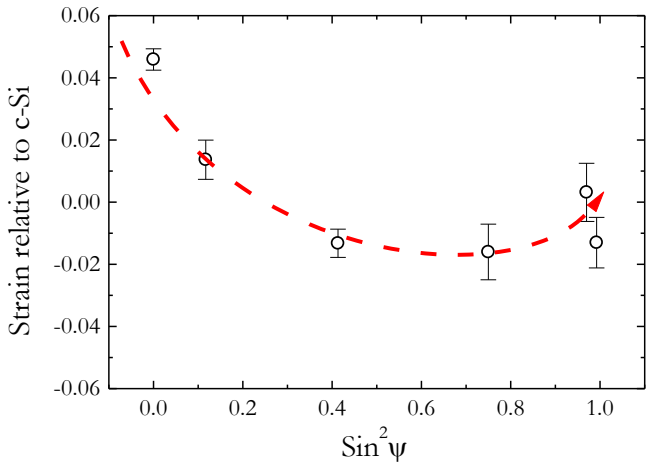

Fig.43: Typical sin2ψ plot illustrating the shift in the first peak position in the pair correlation function as the sample surface is tilted for the sample deposited at 500 ^{0}C.

As for the diffraction peaks, the sin$^2\psi$ curve for the pair correlation function does not reflect a true linear dependence, but there is consistent behaviour for all different ϕ rotations. This was interpreted as the presence of stress gradient in the sample. There is strong curvature showing a higher compressive strain at the interface to the substrate, decreasing towards the sample surface. The intrinsic strain reflected by the surface stress is similar to that indicated by the diffraction peak, but the thermal mismatch stress reflected in the near interface layer substrate is different. The strain at a low ψ is tensile when determined in reciprocal space while it is compressive in real space. The higher compressive strain at the interface is quite unexpected, as in most of the literature [122] the strain is carried by the bond angle distortion rather than the bond length. Two reasons may explain this behaviour. The strain indicated by the first peak in reciprocal space results from a combination of a probable extension, or compression, of the bond length, and a change in the bond angle. A small change in the bond length will require a larger change in the bond angle to keep the same change in the height of the tetrahedron, and vice versa. The second reason is that the change in the bond length, in the case of amorphous material differs from what can be expected in crystalline material where the structure repeats itself infinitely. In amorphous silicon the change in the bond length will depend on the initial equilibrium position which is also related to the environment around the bonded atoms.

The second peak shows a different behaviour, as can be seen from figure 44 below.

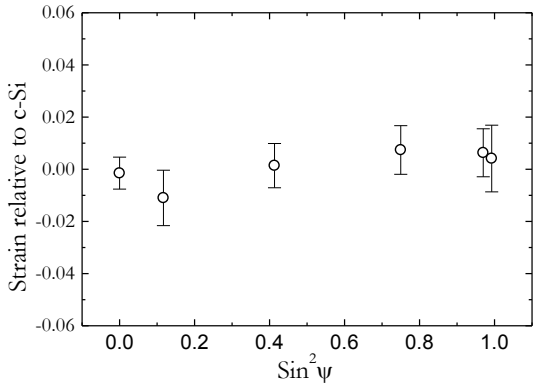

Fig. 44: The shift of the 2nd pair correlation peak as the sample surface is tilted for the sample deposited at 500 ^{0}C.

The two regions are still separated, but in this situation the first region shows nearly zero gradient when fitted with a straight line, while the near surface region has changed to a positive slope, and therefore indicates a tensile stress state carried by the bond angle distortion.

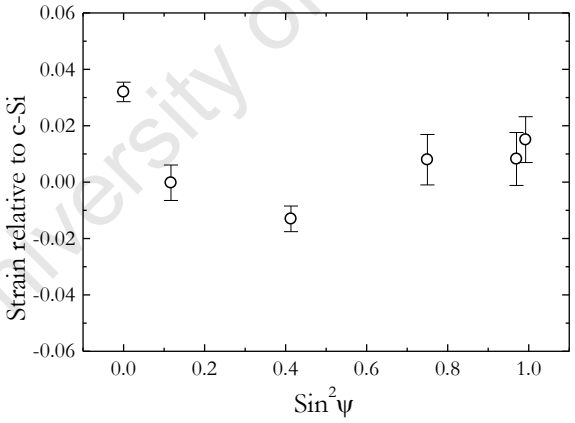

Fig. 45: The shift of the first pair correlation peak as the sample surface is tilted for the sample deposited at 300 ^{0}C.

The 1st peak in real space for the sample deposited at 300 ^{0}C shows a similar behaviour as the sample deposited at 500 ^{0}C. Figure 45 shows a $\sin^2\psi$ plot from the 1st peak of the pair correlation function of the layer deposited at 300 ^{0}C. In general there is a high compressive strain at the interface to the substrate becoming less compressive towards the surface. Except for the scattering observed at a low ψ, the surface stress is

similar to that at 500 ^{0}C, but the thermal mismatch contribution reflected in the higher compressive strain at the interface layer substrate is lower than the one at higher deposition temperature. The scattering seen in the results at 300 ^{0}C may come from the Fourier transformation process. At a low ψ, the peaks are less resolved than for high ψ, because of the considerable contribution from the substrate, and therefore they yield well defined peaks in the pair correlation function, which however have an uncertain peak position. This effect is less visible in the sample grown at 500 ^{0}C, where the peaks are quite well resolved.

Figure 46 shows a $\sin^2\psi$ plot from the 2nd peak in the pair correlation function from the sample deposited at 300 ^{0}C.

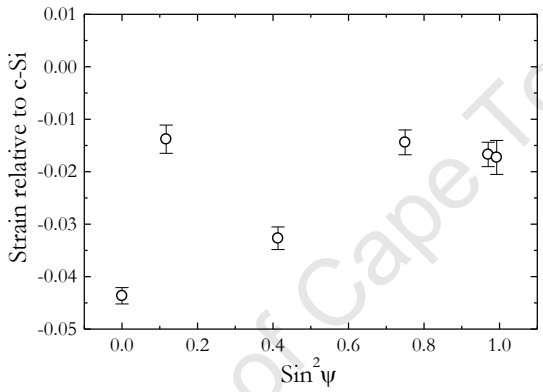

Fig. 46: The shift of the 2nd pair correlation peak as the sample surface is tilted for the sample deposited at 300 ^{0}C.

It can be seen in this plot there is a generally increasing strain with increasing $\sin^2\psi$, indicating tensile strain in the plane of the sample. The scattering, mentioned in the discussion of the first peak related to the background subtraction and the Fourier transformation process, is also apparent here.

Figure 47 shows a $\sin^2\psi$ plot from the first peak from the pair correlation function for the sample deposited at 150 ^{0}C. Excluding the first point at a low ψ, with the same argument as for the sample deposited at 300 ^{0}C, the $\sin^2\psi$ plots indicate a consistent compressive strain for all rotations. However, there is a noticeable ψ-splitting, leading to opposite curvature for a ϕ rotation through 180^0.

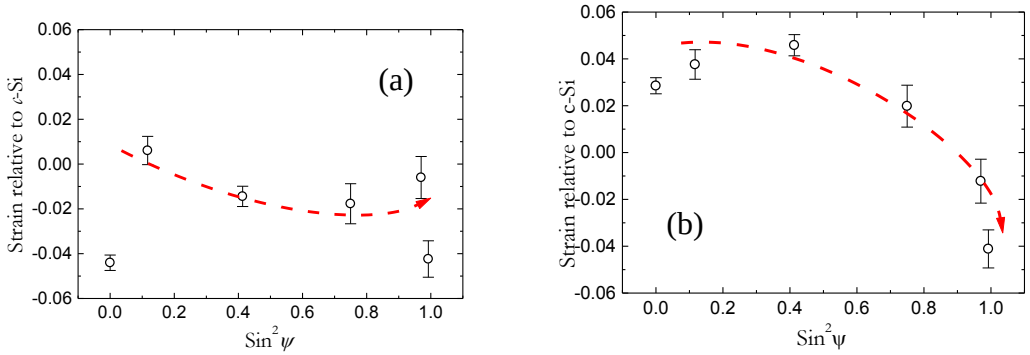

Fig 47: The sin²ψ plot illustrating the ψ-splitting strain variation in a-Si:H sample deposited at 150 ^{0}C (a) ϕ =120^0, and (b) ϕ =300^0.

The second peak in the pair correlation function for the same sample yields almost flat sin$^2\psi$ plots with an almost zero slope, similar to the second diffraction peak in reciprocal space.

b) Residual Stress in Real Space

A similar procedure to the one used to analyse the stress state in reciprocal space was applied to the real space data.

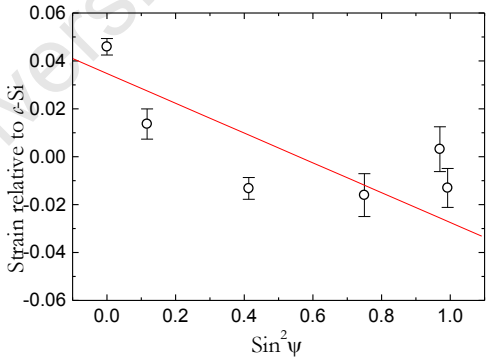

Fig. 48: A linear fit to obtain the gradient used to calculate the stress in the sample deposited at 500^{0}C.

A straight line was fitted to the sin$^2\psi$ plots and the slope values were used to calculate the stress using the appropriate elastic constants. Figure 48 illustrates the fit for the sample deposited at 500 ^{0}C.

The values of σ_ϕ are shown as polar plots, for the first diffraction peak, at the three deposition temperatures in figure 49.

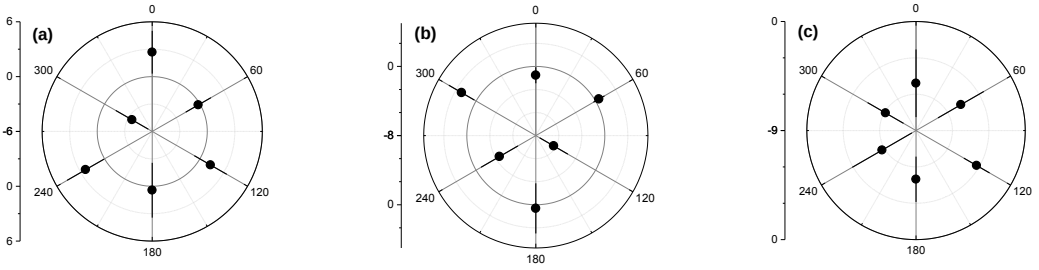

Fig. 49: Stress component σ_ϕ derived from the $\sin^2\psi$ analysis of the first pair correlation peak for *a*-Si:H deposited on Corning glass substrates at: (a)150 ^{0}C , (b) 300 ^{0}C, and (c) 500 ^{0}C.

Due to the large scatter in the data, the anisotropy seen in the projected stress for the diffraction peaks is not clear, but similar trends can be observed. The stress is compressive in general, but for the sample deposited at a low temperature significant tensile stresses were recorded. From the first nearest neighbour peak, the stress is slightly tensile at a low deposition temperature and changes to highly compressive for the sample deposited at 500 ^{0}C.

Similar polar plots, obtained from the second diffraction peak in reciprocal space are displayed in figure 50 below.

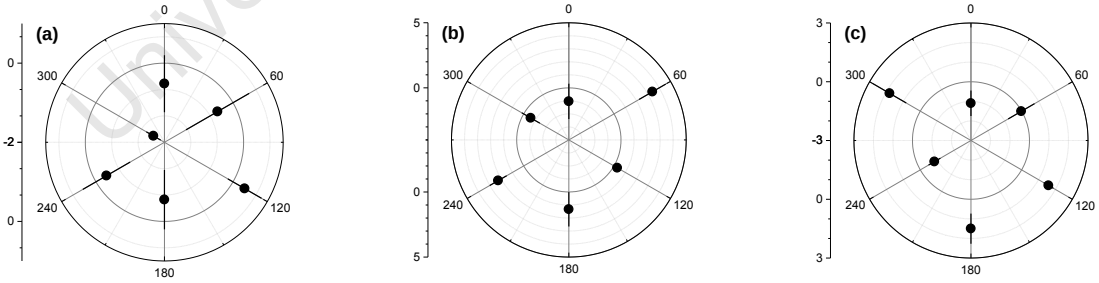

Fig. 50: Stress component σ_ϕ derived from the $\sin^2\psi$ analysis of the second pair correlation peak for *a*-Si:H deposited on Corning glass substrates at: (a)150 ^{0}C , (b) 300 ^{0}C, and (c) 500 ^{0}C.

All samples exhibit a compressive stress, which changes with deposition temperature, and the stress distribution is ϕ dependent. It generally appears that, as for the second diffraction peak in reciprocal space, the stress is compressive and increases with deposition temperature.

Despite the obvious curvature in some of the $\sin^2\psi$ plots, for the same reasons discussed for the direct diffraction data, it was not possible to obtain a meaningful fit to two stress regions. Similarly, because of the even larger errors on the normal strain (ψ=0) as discussed in chapter 2.4.3, the intercept of the $\sin^2\psi$ plots could not be used to resolve the stress component and the depth profile. We fitted equation 4.55 to get the stress components, and finally these components were combined to get the normal and principal stresses using equations 4.56, 4.57 and 4.58. These results are shown in Table 3

Biaxial stress in GPa	First nearest neighbour peak in RDF			Second nearest neighbour peak in RDF		
	Mw170 at 150 ^{0}C	Mw172 at 300 ^{0}C	Mw173 at 500 ^{0}C	Mw170 at 150 ^{0}C	Mw172 at 300 ^{0}C	Mw173 at 500 ^{0}C
σ_{11}	+3.23±2.48	+0.50±0.15	-0.89±0.61	-0.53±0.26	-0.68±0.25	0.04±0.87
σ_{22}	-0.72±1.19	-1.54±0.30	+0.56±0.37	+0.11±0.21	-0.35±0.18	-1.38±1.06
σ_{12}	-0.52±0.74	+0.14±0.26	-0.18±0.27	-0.36±0.17	+0.050±0.13	-0.19±0.88
$\sigma_{11}+\sigma_{22}$	+2.51±2.76	-1.03±0.34	-0.33±0.71	-0.42±0.34	-1.03±0.30	-0.94±1.38
σ_1	+3.29±2.02	+0.51±0.28	+0.59±0.54	+0.27±0.47	-0.34±0.22	+1.03±1.93
σ_2	-0.78±2.02	-1.55±0.28	-0.92±0.54	-0.69±0.47	-0.69±0.22	-1.97±1.93

Table 3: Residual stresses, in as deposited samples, estimated from the position of the first and second nearest neighbour peak in reciprocal space for all ϕ rotations.

Because of the obvious non-linear dependence of strain on $\sin^2\psi$, the errors in the fitted parameters are large. Nevertheless, certain trends are apparent. The bond stress, given by the first peak, appears to be tensile and highly anisotropic in contrast to the stress as determined from the direct diffraction peak for *a*-Si:H deposited at low temperature. As the temperature is increased it becomes compressive and then relaxes as the growth temperature is further increased. This relaxation is most clearly seen in the anisotropy of the principal stresses. For the second peak, there is a continuous increase in compressive stress, in both the normal or principal stresses, as the deposition temperature is increased. We recall that the same trend was seen for the second diffraction peak, which represents the same interatomic distance. However, there is a significant discrepancy in the magnitude of the stress. This may be the result of an incorrect length scale caused by the mixing of the (220) diffraction peak with nearby reflections in reciprocal space. These results are in good agreement with the work of Conde *et al.* [131] the maximum compressive stress occurs

during the amorphous to crystalline transition. Agreement is also found with the work of Han *et al.* [132] for the changes of the compressive stress and H content and light soaking, but disagrees for the temperature dependence.

2.4.5 Strain Relaxation, Residual Stress and Light Soaking in *a*-Si:H

The effect of light soaking on strain variation in *a*-Si:H was investigated on three different samples previously analyzed and cut into four pieces. The illumination periods were 12 and 48 hrs. The choice of soaking intervals was based on our previous results [113]. The analysis took into account the changes in the strain, and therefore the stress, as reflected by the shift in the first and second diffraction peaks and the first two correlation peaks in real space. Figure 51 below shows the $\sin^2\psi$ plot from the first diffraction peak in reciprocal space for the sample deposited at 500 ^{0}C and illuminated for 12 hrs.

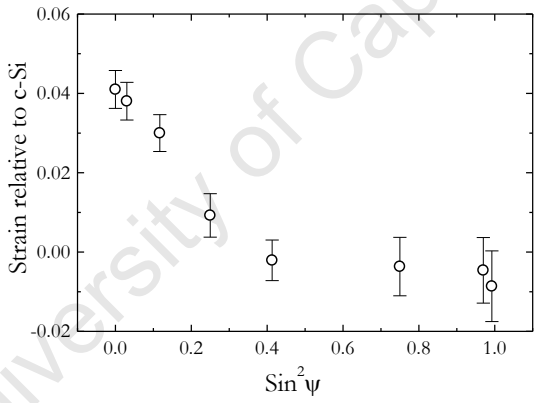

Fig. 51: Typical sin$^2\psi$ plot from the first diffraction peak for an *a*-Si:H sample deposited on a glass substrate at 500 ^{0}C and illuminated for 12 hrs.

This plot shows a clear non-linear dependence of the strain with $\sin^2\psi$ and the behaviour is consistent for all the different ϕ rotations analyzed. As concluded previously, this is a clear indication of non biaxial stress, and hence a stress gradient in the sample analyzed. The plot shows a strong change in the strain at low ψ resulting in strong negative gradient. This is seen as an indication of high compressive strain at the interface between the layer and the substrate. At higher ψ the plot indicates an almost constant strain for increasing $\sin^2\psi$. This low gradient is associated with a low compressive strain at the sample surface. The next step was to compare the behaviour of the as deposited samples and

illuminated ones. Figure 52 below highlights the changes induced during the short illumination time.

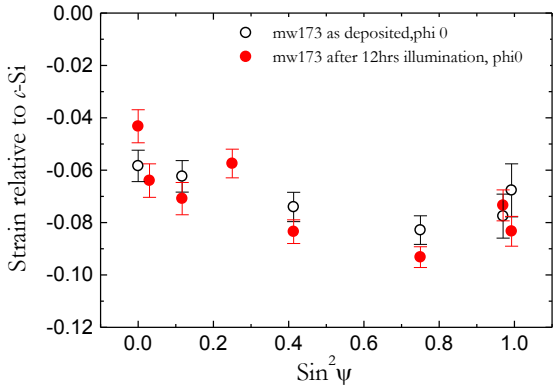

Fig. 52: $Sin^2\psi$ plots from the second diffraction peaks in reciprocal space for an *a*-Si:H sample as deposited and after 12 hrs illumination. The sample is deposited on a glass substrate at 500 ^{0}C.

The plot of the as deposited sample shows less compressive strain at the interface compared to the illuminated sample, but in the near surface region the as deposited sample shows a higher compressive strain. This is consistent with models proposed for the light induced degradation mechanism [31,32,80], and shows a relaxation of the intrinsic stress near the surface following Si-Si bond breaking and hydrogen motion in the illuminated sample. The relaxation of the near surface region will result in an increased thermal mismatch contribution in the interface region, as this compressive stress is no longer balanced by the less compressive stress in the near surface region. This argument is supported by the fact that, on further illumination the stress relaxation which started from the sample surface proceeds deeper into the sample, and the stress at the interface decreases with further illumination. This effect is shown in figure 53, where the sample is illuminated for 12 and 48 hrs.

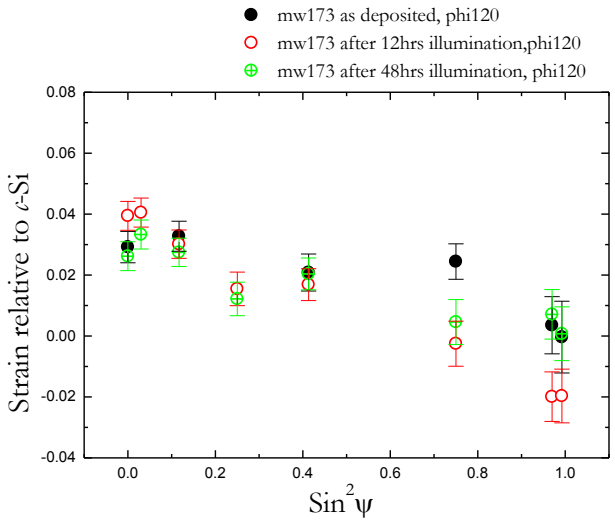

Fig. 53: Sin²ψ plots from the 1st diffraction peak in reciprocal space for an a-Si:H sample in as deposited condition and after 12 and 48 hrs illumination. The sample is deposited on glass substrate at 500 ^{0}C.

It can be seen from the above plot that the as deposited sample and the longer illuminated samples have similar gradients, while the intermediate sample shows a more pronounced gradient. This effect is clearer at a higher ψ, while at a low ψ the strain does not change significantly. This is an indication that the observed effect starts from the sample surface, and cannot be a thermal effect. The illumination time intervals are long enough for the sample to reach thermal equilibrium, and therefore allow changes to occur throughout the layer. Due to the fact that the samples analysed are only a few microns thick, the demarcation between the near surface and the bulk of the sample is not easy to draw. The change in the near surface strain may easily be affected by the induced change in the bulk of the sample. This can be seen when, what is supposed to be a decrease in the strain gradient in the near surface region changes to a slight increase, because it is compensated by the thermal mismatch contribution from the interface, which is no longer balanced by the surface stress. The same overall behaviour is seen in a quantitative analysis of the principal and normal stresses. For the reason outlined in the previous section, only a single linear fit to $\sin^2\psi$ curves has been performed. From the ϕ dependent slopes, the normal and principal stresses, given in table have been determined as described above. The following tables highlight the effect of illumination on the stress state in the sample deposited at 500 ^{0}C.

Biaxial stress in GPa	1st peak (111)			2nd peak (220)		
	As deposited.	After 12hrs illum	After 48hrs illum	As deposited	After 12hrs illum	After 48hrs illum.
σ_{11}	-1.80±0.29	-4.03±0.46	-1.64±0.42	-2.05±0.25	-1.97±0.24	-1.67±0.22
σ_{22}	-2.24±0.25	-3.80±0.55	-2.49±0.37	-2.47±0.40	-2.06±0.22	-1.53±0.14
σ_{12}	-0.54±0.20	+0.67±0.46	+0.45±0.29	-0.01±0.34	+0.21±0.18	+1.06±0.18
$\sigma_{11+}\ \sigma_{22}$	-4.03±1.00	-7.84±0.38	-4.13±0.72	-4.52±0.56	-4.03±0.47	-3.20±0.33
σ_1	-1.43±2.24	-3.24±0.78	-1.44±2.81	-2.05±0.67	-1.80±0.34	-0.54±0.94
σ_2	-2.60±2.24	-4.59±0.78	-2.68±2.81	-2.47±0.67	-2.23±0.34	-2.66±0.94

Table 4: Reciprocal biaxial stress state in GPa obtained from a-Si:H layer deposited at 500 ^{0}C

Biaxial stress in GPa	First nearest neighbour peak in RDF			Second nearest neighbour peak		
	As deposited.	After 12hrs illum	After 48hrs illum	As deposited	after12hrs illum	After 48hrs illum.
σ_{11}	-5.04±0.90	-0.20±0.83	+0.35±0.29	-0.19±0.89	-1.19±0.09	-0.11±0.03
σ_{22}	-4.32±0.84	-3.98±1.68	-1.68±0.79	+1.17±0.85	-1.04±0.08	-0.86±0.22
σ_{12}	-0.75±0.68	-0.23±1.43	+1.31±0.67	-0.98±0.69	0.20±0.07	+0.38±0.20
$\sigma_{11+}\ \sigma_{22}$	-9.36±1.23	-4.19±1.87	-1.34±0.84	+0.98±1.23	-2.23±0.13	-0.97±0.23
σ_1	-3.85±1.82	-0.19±1.36	+0.99±1.68	+1.69±1.64	-0.91±0.29	0.046±0.45
σ_2	-5.51±1.82	-4.00±1.36	-2.32±1.68	-0.70±1.64	-1.33±0.29	-1.02±0.45

Table 5: Real biaxial stress state in Gpa obtained from a-Si:H layer deposited at 500 ^{0}C

For the sample deposited at 500 ^{0}C, the normal stress estimated from the first peak in reciprocal space, stays compressive, but increases on short illumination before dropping back to the initial value stress value. The principal stress follows a similar pattern, and the anisotropy is also reduced on longer illumination. The same behaviour is reflected in the second reciprocal peak, where the as deposited sample showed a slightly compressive stress which becomes more compressive on short illumination time, and on longer illumination time the stress is seen to be slightly tensile.

Biaxial stress in GPa	1st peak (111)			2nd peak (220)		
	As deposited.	After 12hrs illum	After 48hrs illum	As deposited	After 12hrs illum	After 48hrs illum.
σ_{11}	0.37±0.32	-1.99±0.26	-3.32±0.49	-1.05±0.21	-1.61±0.59	-2.05±0.56
σ_{22}	0.36±0.47	-1.86±0.42	-2.41±0.48	-1.48±0.28	-0.50±1.05	-0.97±0.83
σ_{12}	-0.12±0.40	-0.52±0.35	-0.48±0.39	-0.02±0.23	-0.27±0.89	+1.29±0.70
$\sigma_{11+}\sigma_{22}$	0.73±0.57	-3.86±0.49	-5.73±0.69	-2.52±0.35	-3.09±0.66	-2.11±1.21
σ_1	0.49±9.78	-1.41±2.90	-2.20±0.80	-1.05±0.25	-1.47±0.48	-0.43±1.00
σ_2	0.24±9.78	-2.45±2.90	-3.53±0.80	-1.48±0.25	-1.61±0.48	-1.67±1.00

Table 6: Reciprocal biaxial stress state in GPa obtained from a-Si:H layer deposited at 300 ^{0}C

Biaxial stress in GPa	First nearest neighbour peak in RDF			Second nearest neighbour peak		
	As deposited.	After 12hrs illum	After 48hrs illum	As deposited	After 12hrs illum	After 48hrs illum.
σ_{11}	+0.21±0.48	-1.96±1.10	-0.18±0.10	-0.14±0.71	+0.03±0.03	-1.33±0.48
σ_{22}	+0.93±1.56	+0.50±0.38	-7.16±2.11	+1.55±1.13	-0.12±0.08	-1.50±0.56
σ_{12}	-0.43±1.34	+0.08±0.08	+0.81±1.83	+1.70±0.95	+0.12±0.07	+0.76±0.46
$\sigma_{11+}\sigma_{22}$	1.15±1.63	-1.47±1.17	-7.34±2.12	1.41±1.34	0.15±0.08	-2.82±0.74
σ_1	1.96±6.03	0.50±0.82	-0.08±1.78	2.61±2.74	0.21±0.26	-0.65±0.4.25
σ_2	-0.82±6.03	-1.96±0.82	-7.26±1.78	-1.20±2.74	-0.06±0.26	-2.18±4.25

Table 7: Real biaxial stress state in GPa obtained from a-Si:H layer deposited at 300 ^{0}C

The sample deposited at 300^{0}C, shows a tensile normal and principal stresses, in as deposited sample from the first and second diffraction peak (Table 6). Upon illumination, the stress gradually changes to compressive stress on short illumination time. On long illumination time the first peak shows a continuous increase in the compressive stress while the second peak becomes less compressive. The same behaviour is seen in pair correlation peaks (Table 7) except that the stress changes to tensile on longer illumination time.

Biaxial stress in GPa	1st peak (111)			2nd peak (220)		
	As deposited.	After 12hrs illum	After 48hrs illum	As deposited	After 12hrs illum	After 48 hrs illum.
σ_{11}	-2.12±1.91	-1.84±0.18	-1.18±0.80	-0.004±0.21	-0.77±0.44	0.06±0.60
σ_{22}	-0.86±1.29	-2.74±0.19	-3.02±0.68	-0.36±0.32	-0.43±0.56	0.08±0.53
σ_{12}	-1.18±0.98	-0.12±0.16	0.11±0.54	0.003±0.27	+0.50±0.47	0.36±0.42
$\sigma_{11+}\ \sigma_{22}$	-2.99±2.31	-4.59±0.26	-4.20±1.05	-0.37±0.39	-1.21±0.71	0.14±0.80
σ_1	-0.15±2.74	-1.83±0.23	-1.17±0.75	-0.004±0.27	-0.08±1.57	0.43±12.91
σ_2	-2.84±2.74	-2.76±0.23	-3.02±0.75	-0.36±0.27	-1.13±1.57	-0.29±12.91

Table 8: Reciprocal biaxial stress state in GPa obtained from a-Si:H layer deposited at 150 ^{0}C.

Biaxial stress in GPa	First nearest neighbour peak in RDF			Second nearest neighbour peak		
	As deposited.	After 12hrs illum	After 48hrs illum	As deposited	after12hrs illum	After 48hrs illum.
σ_{11}	+3.23±2.48	+0.50±0.15	-0.89±0.61	-0.53±0.26	-0.68±0.25	0.04±0.87
σ_{22}	-0.72±1.19	-1.54±0.30	+0.56±0.37	+0.11±0.21	-0.35±0.18	-1.38±1.06
σ_{12}	-0.52±0.74	+0.14±0.26	-0.18±0.27	-0.36±0.17	+0.050±0.13	-0.19±0.88
$\sigma_{11+}\ \sigma_{22}$	+2.51±2.76	-1.03±0.34	-0.33±0.71	-0.42±0.34	-1.03±0.30	-0.94±1.38
σ_1	+3.29±2.02	0.51±0.28	0.59±0.54	0.27±0.47	-0.34±0.22	1.03±1.93
σ_2	-0.78±2.02	-1.55±0.28	-0.92±0.54	-0.69±0.47	-0.69±0.22	-1.97±1.93

Table 9: Real space biaxial stress state in GPa obtained from a-Si:H layer deposited at 150 ^{0}C.

For the sample deposited at the lowest temperature (Tables 8 and 9), the compressive stress also increases on short illumination time but changes to less compressive on further illumination. Taking the results for all three samples together, to form a general picture, the effects of illumination on the residual stress can be summarised as follows. For short illumination times, there is a relaxation of tensile, probably intrinsic, stress, particularly nearer the surface. This leads to the overall stress value, and the principal stresses, becoming more negative. As the illumination time is increased, the stress relaxation progresses, with an overall reduction in the magnitude of the residual stress.

3. OPTICAL AND CHEMICAL CHARACTERIZATION

Important results from different experimental techniques, used to gain insight on the a-Si:H behaviour in either as deposited samples, or after illumination, are presented in this chapter. They are presented separately in 3 categories, depending on the nature of techniques used and the properties investigated: optical characterization using UV-visible absorption spectroscopy; and chemical characterization using Fourier infrared spectroscopy (FTIR) and elastic recoil detection analysis (ERDA).

3.1 Ultraviolet-Visible absorption spectroscopy

Ultraviolet and visible spectroscopy (UV-vis) is a common analytical technique for quantitative and qualitative analysis of solid, liquid, or gas samples. This technique is easy to perform, relatively inexpensive, non-destructive, and rapid. When light, which is an electromagnetic wave, passes through a material it interacts with electrons or atoms of the target. Photons with energy higher than the energy band gap will be absorbed while those with lower energy will be transmitted. The intensity of light absorbed by a sample can be calculated, and the technique provides a very sensitive and reproducible means for determining the concentration of absorbing species.

Figure 54 illustrates the principle of operation of a typical UV-visible spectrometer. Polychromatic light is separated into its component wavelengths λ_i by a prism or diffraction grating. Each monochromatic beam is then split into equal beam intensity by a half silvered mirror. The first beam passes through the test sample and the transmitted intensity $I(\lambda)$ is recorded. The second beam also passes through a reference sample and yields the reference intensity $I_0(\lambda)$. The path length of the two beams is otherwise kept the same.

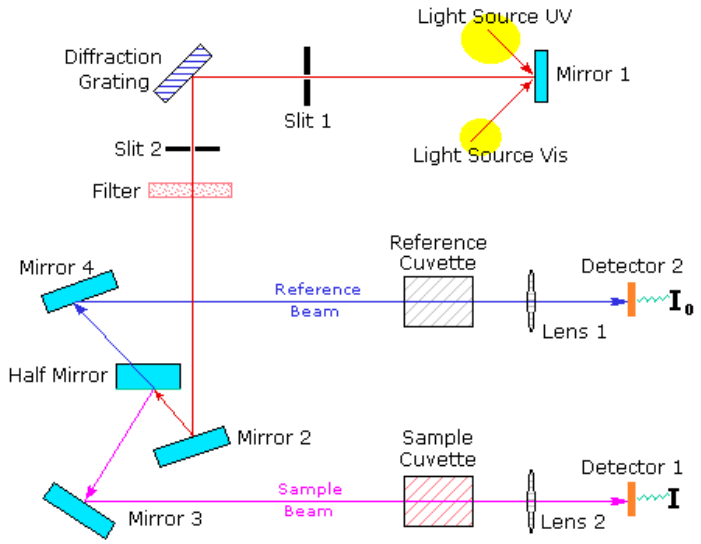

Fig 54: The principle of Uv-Visible absorption spectrometer [133].

The spectrometer automatically scans all the component wavelengths in the same manner, and the ratio of I to I_0 for each wavelength is calculated to give the absorption spectrum of the sample analyzed. The detector is typically photomultiplier or a photodiode which is sensitive in the near ultraviolet and visible range.

3.1.1 Theoretical Background on the Determination of *a*-Si:H Layer Thickness and Optical Parameters

The measured transmittance $T=I/I_0$, which is the ratio between the intensity of the reference beam I_0 and the sample beam I reaching the detector, depends on the wavelength and the sample thickness d. From Lambert's law, the relative intensity losses is proportional to the travelled thickness x [134]

$$\frac{dI(x)}{I(x)} = -\alpha dx \tag{4.59}$$

where α is the absorption coefficient. The absorbance χ, defined as the logarithm of the inverse transmittance,

$$\chi = \log_{10}\frac{1}{T}, \tag{4.60}$$

is the most commonly used experimental parameter. The absorption coefficient is also related to the absorbance via the following expression, obtained by combining the solution to the differential equation III.4.59 the equation III.4.60:

$$A = \frac{-\log_{10} x}{d \log_{10} e}, \tag{4.61}$$

where d is the optical thickness of the sample.

To determine the optical parameters and the thickness of the layers involved in this work, we used Swanepoel's envelope method [135,136], based on the idea pioneered by Manifacier [137]. This experimental method allows us to determine the film thickness and the optical constants from the wavelength dependent transmission spectrum at a normal incidence $T(\lambda)$ collected from the UV-visible spectrophotometer. The method, which is applicable to any transmission spectrum showing appreciable interference fringes, is based on using the computer generated envelope around the upper and lower part of the spectrum as shown in figure 55.

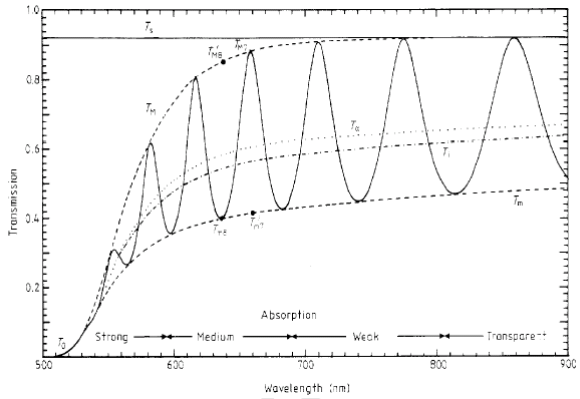

Fig.55. Simulated transmission spectrum (full curve) for 1μm film of a-Si:H on a finite thickness glass substrate[135].

The interferences fringes observed in the transmission spectrum, in the region of transparency or weak absorption, result from multiple reflections in the layer and can be used to calculate the optical constants of the film. First, let us assume a transparent substrate with a refractive index n_{sub} and with a thickness of several orders of magnitude larger than the layer thickness, so that there are no coherent multiple reflections taking place in the substrate. For a uniform and homogeneous film, with a thickness d, deposited on a thick transparent glass substrate the complex refractive index is $n_c = n - ik$ where, n is the real refractive index and k is the extinction coefficient. If λ is the wavelength of the light used, the extinction coefficient can be related to the absorption coefficient α by the following relation

$$\alpha = \frac{4\pi k}{\lambda}. \tag{4.62}$$

As the sample is surrounded by air with a refractive index $n_{air} = 1$, the analysis of the transmitted spectrum must take into account all the multiple reflections at the three interfaces: air and film, film and substrate, and substrate and air,

$$T = T(\lambda, n, d, n_{sub}, \alpha).$$

But as n_{sub} is known, the expression for transmission *T,* assuming normal incidence, and taking *k=0*, can be written in convenient way as a function of the refractive index and the absorbance $\chi(\lambda)$ of the layer as follows [135]

$$T(\chi, n) = \frac{A\chi}{B - C\chi\cos\varphi + D\chi^2}, \tag{4.63}$$

where

$$\begin{aligned} A &= 16n^2 n_{sub} \\ B &= (n+1)^3 (n + {n_{sub}}^2) \\ C &= 2(n^2 - 1(n^2 - {n_{sub}}^2) \\ D &= (n-1)^3 (n - {n_{sub}}^2) \\ \varphi &= 4\pi nd / \lambda \\ \chi &= \exp(-\alpha d) \end{aligned} \tag{4.64}$$

The transmitted spectrum oscillates within an envelope defined by two extrema of interference fringes T_M and T_m, corresponding to $\cos\varphi = +1$ and $\cos\varphi = -1$ respectively (see fig. 55),

$$T_M = \frac{A\chi}{B - C\chi + D\chi^2}, \tag{4.65}$$

$$T_m = \frac{A\chi}{B + C\chi + D\chi^2}. \tag{4.66}$$

The basic equation for interferences fringes can be deduced from the boundary conditions for a maximum and minimum in the transmission spectra. By taking $\cos\varphi = +1$ for a maximum, and $\cos\varphi = -1$ for a minimum,

$$2nd = (m + \frac{1}{2})\lambda, \tag{4.67}$$

with m being an integer for a maximum, and a half integer for a minimum. This important relation, also called the interferometric equation, defines the relation between the refractive index of the film and the film thickness. Eliminating χ from the equations for T_M and T_m an expression of the refractive index can be deduced

$$n = \left[N + (N^2 - {n_{sub}}^2)^{\frac{1}{2}} \right]^{\frac{1}{2}}, \tag{4.68}$$

where

$$N = 2n_{sub}\left(\frac{T_M - T_m}{T_M T_m} \right) + \frac{\left({n_{sub}}^2 + 1 \right)}{2}. \tag{4.69}$$

Here T_M and T_m are the maximum transmission, and the corresponding minimum, at a particular wavelength. Hence, one of these values is directly determined, while the other is derived from the corresponding position on the envelope curve.

a) ***Refractive Index***

The refractive index of the *a*-Si:H layer can be determined from the optical transmission spectrum by using equation III.4.68 order to obtain an accurate result, especially in the region of weak and medium absorption, accurate values of T_M and T_m are required as input. The values reported here were calculated using the following fitting function [138],

$$n(\lambda) = \frac{a}{\lambda^p} + n_0 \tag{4.70}$$

where *a* is a constant related to the film thickness and *p* is the order of the best polynomial fit. In our case *p* ranged between 2 and 5, but the procedure is not very sensitive to the actual value.

The procedure used to estimate the refractive index is an iterative calculation, with an estimated value for the film thickness. The values of the extrema (read off from the transmission spectrum) and the extrapolated order of the first extremum are required as input. Once the values of wavelength at the extrema are obtained with their corresponding *m* from the interferometric equation, a graph of wavenumber $\nu = 1000/\lambda$ vs $m = 0, 1/2, 1, 3/2$ can be plotted. The first observable extremum at low wavenumber is

initially assigned $m = 0$ or ½, depending on if it is a maximum or a minimum. By drawing a best straight line through the first point and extrapolating it back to $\nu = 0$, the value of the intercept gives the required order number of the first extremum. An illustrative example is shown in fig 56(a) below.

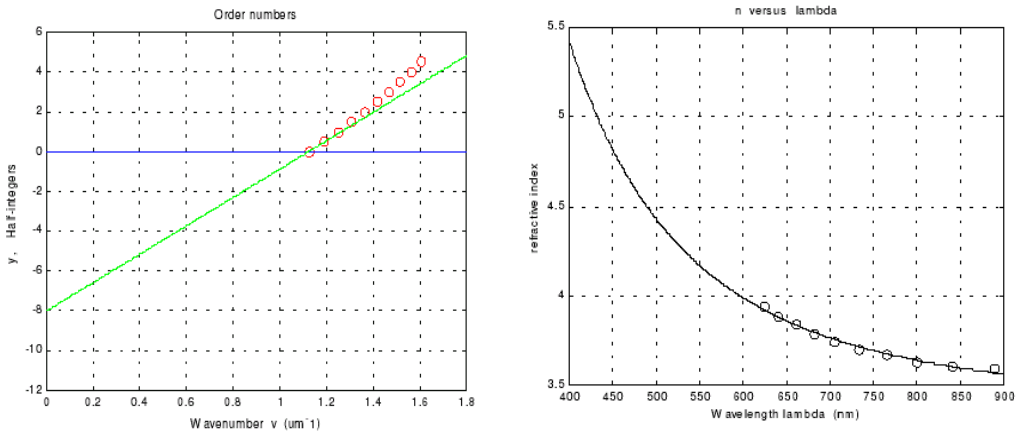

Fig.56: (a) determination of the order number for the first extremum and (b) refractive index as a function of the wave number for an a-Si:H layer deposited at 450°C on a Corning glass 7059 substrate.

By adjusting the thickness of the sample and the parameter *p*, a good fit through the points of $n(\lambda)$ versus the wavenumber ν (see figure 56(b)) can be achieved, and therefore values of the layer thickness d and the refractive index at zero energy n_o are obtained. Thicker samples yield an accumulated number of points due to a large number of extrema and it becomes difficult to draw a best fit through the first points. This can lead to inaccurate determination of the order number of the first extremum. The method is therefore more accurate for thin samples, with thicknesses less than a micron.

b) ***Film Thickness***

Knowing the refractive index of the substrate s, and reading T_M and T_m from the transmission spectrum, the refractive index of the film $n(\lambda)$ can be calculated, and the film thickness can be obtained using the interferometric equation as follows. Eliminating *m* from the interferometric equation III.4.67 for two adjacent maxima or minima yields

$$d = \frac{\lambda_1 \lambda_2}{2\left(n_2 \lambda_1 - n_1 \lambda_2\right)}, \tag{4.71}$$

where n_1 and n_2 are the refractive indices at two adjacent points, and λ_1 and λ_2 the corresponding wavelengths. The values obtained may depend on the peaks chosen, and a

best result may be the average of those individual thicknesses. To achieve this, the interferometric equation is expressed as follows

$$\frac{l}{2} = 2d\frac{n(\lambda)}{\lambda} - m_1, \tag{4.72}$$

where m_1 is the order number of the first extremum and $l = 1, 2, 3...$ Plotting $l/2$ as a function of $n(\lambda)/\lambda$ will yield a straight-line graph, with a slope that is twice the average thickness of the sample. While fitting the straight line, we must keep in our mind that the intercept is the negative of the order number of the first extrema, and therefore it must be an integer if the first extremum is maximum or a half integer it is minimum. The line should therefore be drawn in such way that it passes exactly through the nearest integer or half integer.

c) ***Absorption Coefficient***

One of the most important advantages of amorphous silicon over its crystalline counter part is a much larger absorption coefficient in the usable visible range of the solar spectrum. Once $n(\lambda)$ is known all the constants in equation (4.63) can be calculated. Solving equation III.4.63 for the absorbance χ, yields an important expression for absorbance

$$\chi = \left(\frac{\frac{A}{T} - C\cos\varphi}{2D}\right) \pm \left[\left(\frac{\frac{A}{T} - C\cos\varphi}{2D}\right) - \frac{B}{D}\right], \tag{4.73}$$

From which the absorption coefficient can be deduced using

$$\alpha = \left|\frac{\ln\chi}{d}\right|. \tag{4.74}$$

Once $\alpha(\lambda)$ is known the extinction coefficient can be calculated by inversion of equation III.4.62.

(4.75)

Figure 57 shows a typical plot of the absorption coefficient as a function of the photon energy, from which the band gap can be estimated as described below.

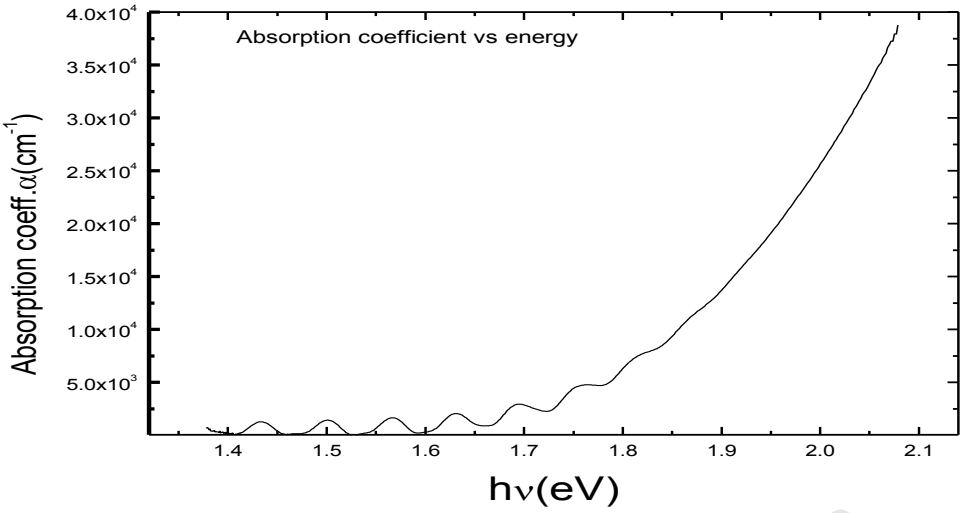

Fig.57: Dependence of the absorption coefficient on the photon energy for an *a*-Si:H sample deposited at 500°C.

d) ***Optical Energy Band Gap***

In practice the optical band gap is extracted from the Uv-Visible transmission spectrum, and Tauc's empirical relationship between the absorption coefficient and the optical band gap. In the region of medium absorption in an amorphous solid this is expressed as [138]

$$\left[\alpha(\lambda)n(\lambda)E(\lambda)\right] = c\left[E(\lambda) - E_g^{opt}\right]^{r+s+1}, \tag{4.76}$$

where c is a constant, and r and s are parameters describing the shape of the band edges. In the original literature, Tauc's convention assumed the density of states to be parabolic in both the valence and conduction bands, *i.e.* $r = s = \frac{1}{2}$. The Tauc band gap can then be determined by an extrapolation of the linear part of the plot $\left[\alpha(\lambda)n(\lambda)E(\lambda)\right]^{\frac{1}{2}}$ versus $E(\lambda)$ to $\alpha(\lambda)=0$. However, Klazes *et al.* [139] proposed a similar relationship, but assuming linear band edges with $r = s = 1$, in which case the so-called cubic band gap is obtained by extrapolating the linear part of the plot $\left[\alpha(\lambda)n(\lambda)E(\lambda)\right]^{\frac{1}{3}}$ versus $E(\lambda)$ to $\alpha(\lambda)=0$. The cubic band gap is typically about 0.2eV lower than the Tauc band gap.

.

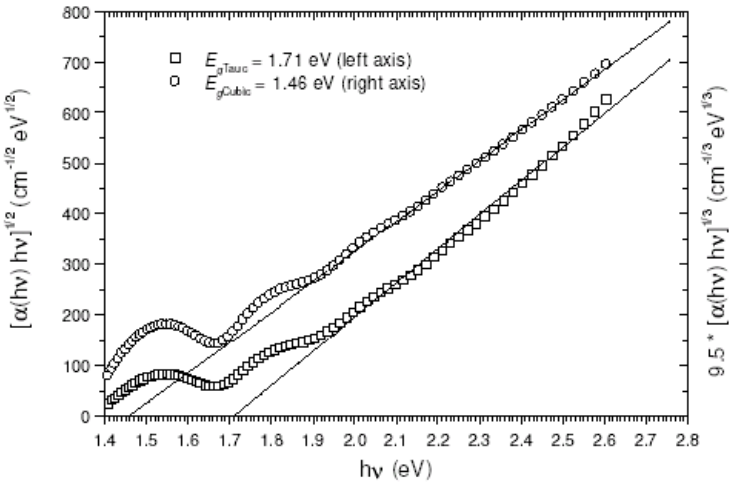

Fig.58. Tauc and cubic energy band gaps from an *a*-Si:H sample deposited at 450°C [138].

3.1.2 Ultraviolet-Visible experimental set up

The UV-Visible measurements were conducted on a Cary/1E/UV-Vis Spectrophotometer with a monochromated light in the energy range between 1.2 and 2.4eV, and an energy resolution of 30 meV. A veil was placed on the top of the machine to shield light from interfering with the measurement. The optical parameters were calculated from the transmission spectrum using the envelope method described above. The film thickness was estimated from the interference fringes arising when the layer thickness is comparable to the wavelength of the light used. The samples analyzed were *a*-Si:H layers deposited on Corning 7059 glass substrates deposited at a varied temperatures between 150 and 500 °C as described in chapter II.1. A set of twelve samples was divided into 3 categories depending on the deposition time and the tantalum wire used:

- 3 thicker samples deposited for 20 minutes using a filament which was allowed to age by not being treated with Hydrogen between depositions.
- 6 thin samples deposited for 11 minutes using a new filament which was treated by flowing hydrogen in the chamber for 5 minutes after each deposition.
- samples deposited with an old filament which had been treated with hydrogen. These were the same samples studied by synchrotron radiation diffraction.

3.1.3 Ultraviolet-Visible Absorption Spectroscopy Results and Discussions

As mentioned before the samples investigated with the UV-vis technique were classified into three classes, depending on the deposition time and the filament used. The results will also be presented in the same manner, but the discussion will bring them together in a coherent picture. We recall that the results presented here were obtained using the method proposed by Swanepoel from the wavelength dependent transmission spectra recorded with a UV-visible spectrometer.

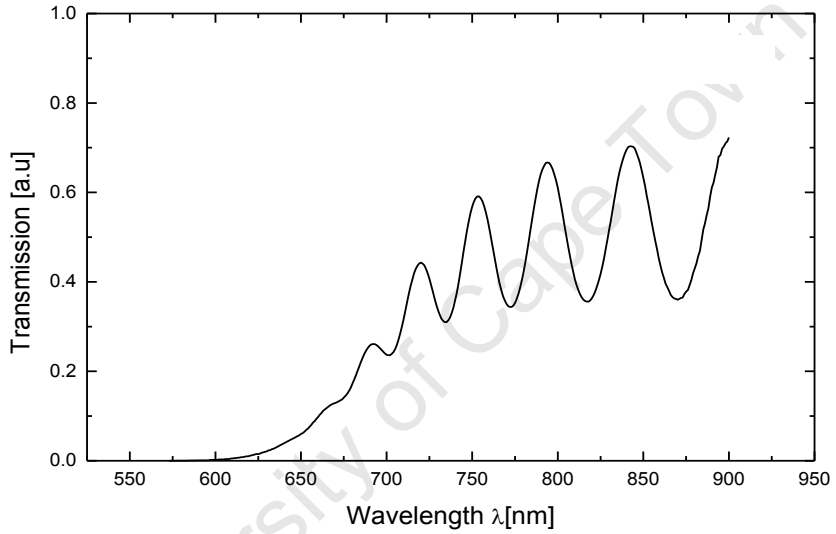

Fig 59: Transmission spectrum for an a-Si:H layer of about 1.5μm deposited on a thick corning glass (300μm).

The spectral dependence of the optical transmission of one of our samples deposited on Corning 7059 glass substrate is shown for illustration if figure 59. The layer can be seen to be uniform in thickness; otherwise the interference fringes would have shrunk giving way to a smooth transmission spectrum.

a) Effect of Deposition Temperature on Refractive Index

Figure 60 below shows the dependence of the refractive index for the three sets of *a*-Si:H layers on the deposition temperature. For each set, with the exception of growth temperature, the deposition conditions were kept constant.

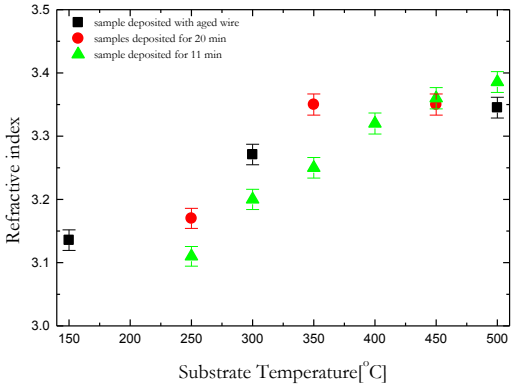

Fig.60: Dependence of the refractive index on deposition temperatures for a-Si:H samples grown on glass substrates.

As can be seen in the figure 60, in all cases the refractive index increases with the deposition temperature. Samples deposited with an aged wire, which had been treated with hydrogen after each deposition seem to have a high refractive index, compared to ones deposited with the same wire when it was still new. As the deposition conditions were the same for both sets of samples, the only difference may result from the catalytic effect at the sample surface, given that the plasma is assumed not to have changed. The thicker samples also seem to show the same effect especially at a low deposition temperature. This can only be explained by the change in the composition of the plasma resulting in different deposition rates, because the thickness of the sample itself does not affect the refractive index, but the density of the sample does. The refractive index gives a measure of the film density as the light bends more when it travels through a dense material, and consequently presents a higher refractive index. The general increase in the refractive index with the growth temperature is, therefore, an indication that the samples become denser as the growth temperature is increased, which also indicates a kind of relaxation of the structure towards the *c*-Si refractive index of 3.42.

The low density at a low deposition temperature was associated with the presence of vacancies or voids in the sample. The densification of the *a*-Si:H sample at a higher deposition temperature can be understood by taking into account two factors:

- At a higher temperature, the diffusion of hydrogen is fast and can redistribute between alternate bonding sites. This creates equilibrium between Si-Si and Si-

H bonds, thus minimizing weak bonds, and therefore dangling bonds, which result from the breaking of the weak Si-Si bonds by mobile hydrogen [140,141].

- The mobility of the species adsorbed on the surface of the growing sample determines the properties of the network structure. If these species can diffuse over an adequate distance, their probability of finding energetically favourable sites rises as a result of relaxation of the amorphous structure. The surface diffusion length l of the radicals is given by [140,141]

$$l = \sqrt{2D_s\tau_s}\,, \tag{4.77}$$

$$\text{where } D_s = \nu a_0^2 \exp(-\frac{E_s}{kT})\,, \tag{4.78}$$

is the surface diffusion coefficient of the radicals, t_s the surface residence, ν the frequency factor, a_o the distance between sites, and E_s the thermal activation energy of hopping. Thus a higher deposition temperature increases the lifetime of the SiH_3 radicals, considered as the dominant radicals in the *a*-Si:H growth, so that they can diffuse longer at the surface of the growing sample before they may find reactive sites which are mainly dangling bonds.

b) Effect of Growth Temperature on the Absorption Coefficient.

The calculated absorption coefficient of the three sets of the samples analysed are plotted in fig.61 as a function of the photon energy.

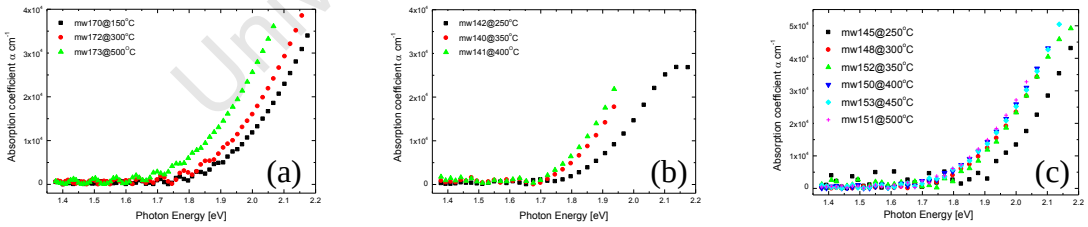

Fig.61: The effect of the deposition temperature on dependence of the absorption coefficient and the photon energy for the three set of a-Si:H sample analysed.

In all cases the absorption coefficient decreases with decreasing photon energy, but as mentioned before there is no sharp extinction when reaching the energy band edge as seen for crystalline material. Instead low values are observed due to the presence of native intrinsic defects. This is an indication that all our samples are still amorphous within the range of deposition temperatures adopted. It also transpires that increasing the deposition

temperature leads to an increased absorption. Figure 62 below shows how the absorption coefficient changes with increased growth temperature.

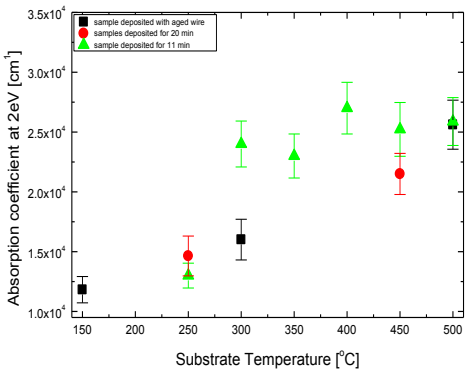

Fig.62: Dependence of the absorption coefficient, at an energy of 2eV, on the substrate temperature of the a-Si:H samples used in this study.

The void-associated dangling bonds contribute to the mid-gap density of states, while the weak reconstructed bonds contribute to the band tails. This behaviour is in line with the decrease in the band gap, which allows more photons to be absorbed.

c) Energy band gap and deposition temperature

Figure 63 below shows the effect of the deposition temperature on the dependence of the Tauc and cubic energy band gaps.

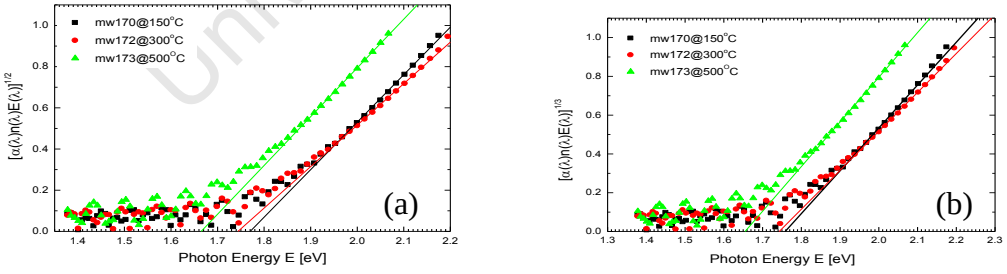

Fig.63: shows the effect of the deposition temperature on dependence of (a) the Tauc and (b) cubic energy band gap for one set of *a*-Si:H sample analyzed.

In the figure 64 the Tauc band gap energy is plotted against the deposition temperature for all the samples studied.

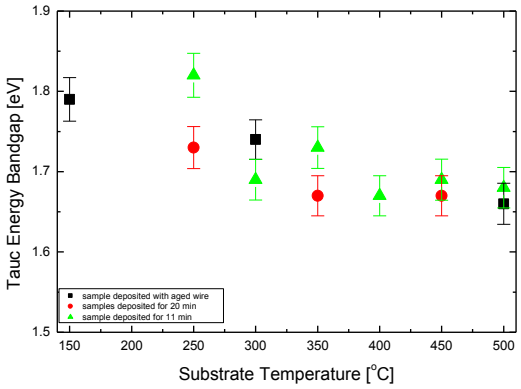

Fig.64: Dependence of the Tauc energy band gap with increasing the *a*-Si:H sample's deposition temperatures.

There is a continual decrease in the energy band gap as the deposition temperature increases reaching saturation as the deposition temperature approaches 350°C. In line with the refractive index, the decrease in the energy band gap is associated with the relaxation of the network towards structure as the deposition temperature increases, but the value of 1.12eV for C-Si is not reached, as our samples remain amorphous within the range of temperatures used for this study. Above 350^{0}C the band gap saturates at approximately 1.66eV. High band gap energy is also associated with the presence of microvoids and other defects in the sample, as suggested by Berntsen [141], so that the band gap can be related to the order of the amorphous network. A highly strained network has a lower band gap than a relaxed one, although their bonding configurations may be similar. The energy band gap is also related to the bond strength in the amorphous network. The higher the strength of the bonds, the larger will be the band gap. Since the Si-H bond is stronger than the Si-Si bond, increasing H alloying will increase the energy band gap. A lower band gap results in more photons being absorbed, and consequently in higher current production. However a low band gap implies that the potential energy difference between the generated electron-hole pairs is low and thus results in a lower voltage.

To summarize this section we have shown that the optical properties of *a*-Si:H can be affected by the temperature of the substrate. An optimum deposition temperature of the substrate can be reached at 350°C where a further increase in the deposition temperature does not change the optical parameters. The optical characterization also shows a continual relation of the amorphous network and an increased order as the deposition temperature is increased, but also highlighted the presence of intrinsic native defects in the material.

Optically the samples grown at higher temperatures are, of good quality with the absorption coefficient above $1x10^4 cm^{-1}$and an optical band gap around 1.66 eV, which compares favourably with PECVD samples for high quality devices[142].

3.2 Fourier Transform Infrared Spectroscopy

Infrared spectroscopy has proven to be a useful technique in the study of local bonding configurations [82]. It is based on the fact that chemical bonds in a solid can absorb electromagnetic radiation when the excitation frequencies are the same as the vibrational frequencies of the bond. Fourier transform infrared spectroscopy is commonly used to determine the bonding configuration and concentration of hydrogen in *a*-Si:H layers. However, the bond must also possess a dipole moment in order to be detected [143], and therefore molecular hydrogen will not be detected. Other properties such as the refractive index of the thin film, the film thickness, and the sample density can also be determined from the FTIR transmission spectrum.

The principle of operation of an FTIR spectrophotometer is based on the Michelson interferometer [144]. As illustrated in the figure 65 below radiation from a broad monochromatic source is split into two rays by a transparent parallel-sided plate, so that half is transmitted, and half is reflected. The reflected beam is once again reflected by a movable plane mirror, and directed towards the detector through the beam splitter. The transmitted beam is also reflected by a second mirror toward the detector through a compensating plate of the same material and thickness as the beam splitter. The two reflected rays, reaching the detector after travelling different paths, will interfere constructively or destructively depending on the wavelength and position of the movable mirror. The relation between the position of the mirror and the wavelength is calibrated by using a monochromatic source of known wavelength. With a continuous light source those interferences happening simultaneously result in a very complex interferogram, which is recorded by the detector, which must have a good response to a wide range of infrared frequencies, with wavenumbers ranging from 5000 to 30 cm^{-1}. If a sample is placed between the beam splitter and the detector, the transmittance or absorbance spectrum of the sample can then be obtained by computing the Fourier transform of the interferogram.

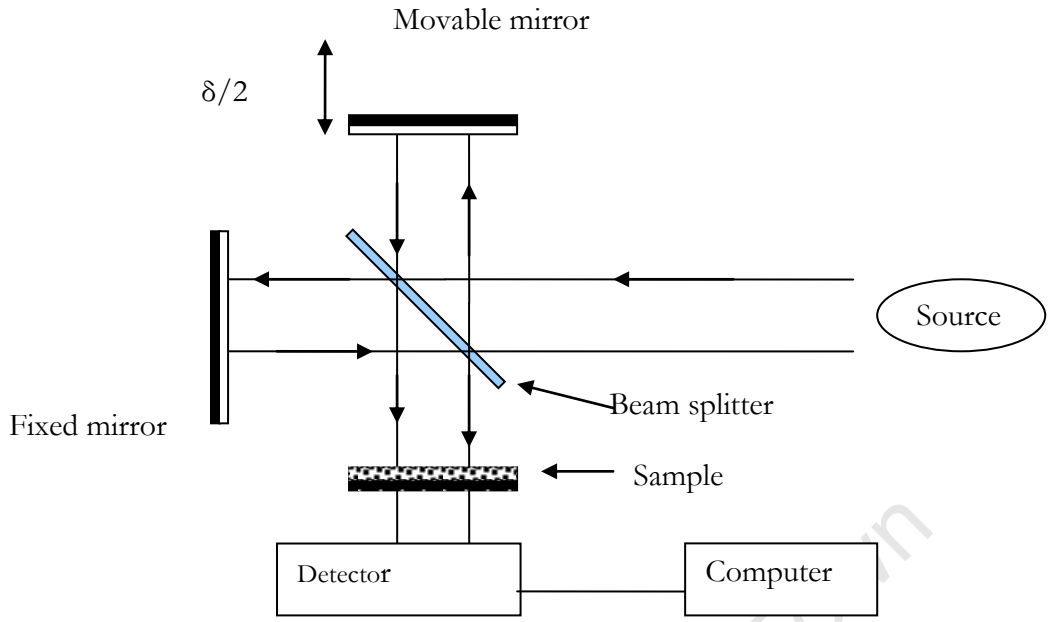

Fig.65: The principle of a Michelson interferometer in FTIR spectrometer [144].

3.2.1 Theoretical Considerations of Hydrogen Content and Bonding Configuration in *a*-Si:H

Hydrogen introduced during the deposition of hydrogenated amorphous silicon thin films plays an important role in shaping the structural properties of devices produced with those thin layers. Many authors have confirmed the double role played by hydrogen in *a*-Si:H. On one hand, it was reported to saturate dangling bonds, and hence reduce the numbers of defects acting as recombination centers [20]. On the other hand, hydrogen was implicated in the light induced degradation of *a*-Si:H [21], where structural changes and defect formation may be caused by photo-induced breaking of weak Si-Si bonds in the vicinity of Si-H bonds. A microscopic analysis of the structure and dynamics around the Si-H bonds in amorphous matrix becomes, therefore, extremely important.

a) Hydrogen Bonding Configurations

The frequencies of different molecular vibrations can be used to identify the various types of bonds and functional groups present in a material. By assuming that the atoms are rigid bodies connected together by springs, the frequency of vibration of two

atoms can be expressed, according to the Hookes' law, in a simple harmonic oscillator model of molecular vibrations by [143]

$$\upsilon = \frac{1}{2\pi c}\sqrt{\frac{K}{\mu}}, \tag{4.79}$$

where c is the speed of light, K the force constant of the vibrating bond, and μ the reduced mass of the vibrating system given by

$$\mu = \frac{m_1 m_2}{m_1 + m_2} \tag{4.80}$$

for a rigid diatomic molecule, where m_1 and m_2 are masses of individual atoms. The frequencies of most molecular vibrations lie in the infrared region of the electromagnetic spectrum. For the particular mode to be infrared active, the electric dipole moment of the vibrating molecule must change during the vibration Thus FTIR will only give us information about the bonded hydrogen, and molecular hydrogen cannot be detected.

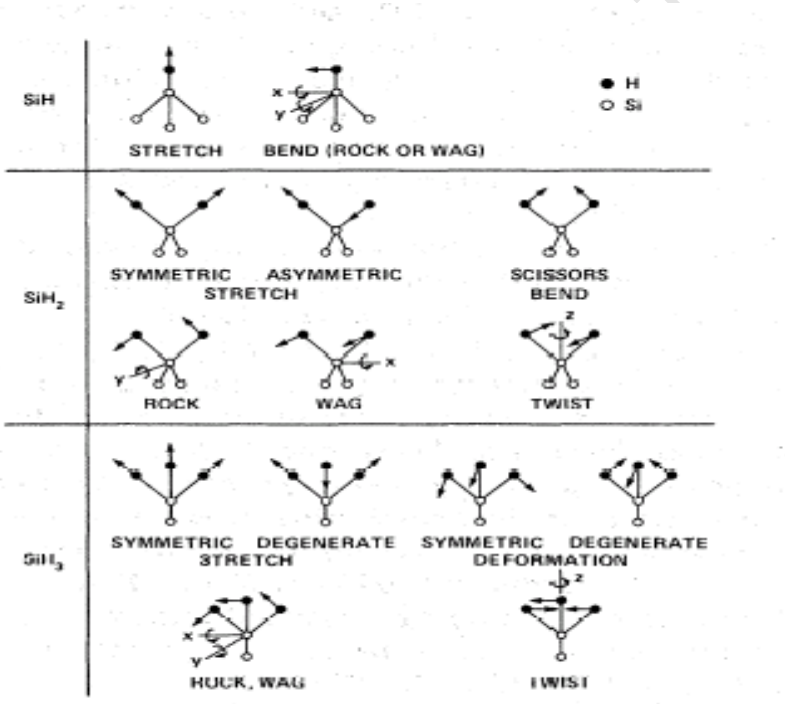

Fig.66: local Si-H vibrations for SiH, SiH_2 and SiH_3 groups [82].

Figure 66 shows the possible molecular vibrations of Si bonded to 1, 2 or 3 hydrogen atoms. The different Si-H environments in *a*-Si:H leads to the FTIR spectrum being characterized by three energy bands [1]:

a) a bond bending mode with broad band around 640 cm^{-1} associated to Si-H bond oscillating in the direction normal to the bond;

b) a bond bending mode with a band in frequency range 800-950 cm^{-1}as well as in the bond stretching modes between 2050 and 2150 cm^{-1}; and

c) a bond stretching mode with a band at 2000-2100 cm^{-1} related to the Si-H bond and Si-H_x complex vibrating in the direction of the bond.

Table 10 gives the generally accepted assignments of hydrogen-bonding configuration to infrared absorption energies as summarized by Lucovsky [82]. It can be noted that not all those modes, in particular the SiH_3 stretching mode, have been observed experimentally in a-Si:H sample.

Wavenumber [cm^{-1}]	**Bonding configuration**	**Vibration mode**
640	Si-H, Si-H_2, $(Si-H_2)_n$, Si-H_3	rocking
845	$(Si-H_2)_n$	bending
880	Si-H_2	bending
890	$(Si-H_2)_n$	bending
2000	Si-H (isolated)	stretching
2070-2100	Si-H (on voids), Si-H_2, $(Si-H_2)_n$	stretching
2130	$(Si-H)_3$	stretching

Table 10 the generally accepted assignments of the Silicon Hydrogen vibration modes in *a*-Si:H.

As can be seen in this table all types of silicon hydrogen bonds contribute to the 640cm^{-1} band, and therefore the integrated absorption mode of this band is a good measure of the total bonded hydrogen in the sample. An empirical correlation exists between the 2090 cm^{-1} stretching band and the film inhomogeneity, such as microvoids dispersed throughout the layer, or that associated with a columnar microstructure [76]. The microstructure fraction parameter R^* which can be obtained from the infrared absorption measurements gives important empirical information about the film inhomogeneity such as multivacancies, small voids, columnar growth morphology, *etc.* in the material [145,146,147.]

$$R^* = \frac{I_{2090}}{I_{2000} + I_{2090}}$$

where I_{2000} and I_{2090} are integrated band intensity of the infrared mode centered at 2000 and 2090cm^{-1}. The increase in 2090cm^{-1} contribution increases the ratio R^* which is the indication of poor quality. Thus high quality materials are the ones having the absorption peak at 2000cm^{-1} significantly exceeding the one at 2090 cm^{-1}.

b) ***Hydrogen Content in a-Si:H***

The hydrogen content C_H is estimated from the integrated absorption intensity I_{640} of the rocking mode of each sample according to the following expression [148]:

$$C_H = \frac{A_{640} I_{640}}{\left(N_{Si} + A_{640} I_{640}\right)}, \tag{4.81}$$

where

$$I_{640} = \int \left(\frac{\alpha(w)}{w} \right) dw, \tag{4.82}$$

is obtained by integrating over the absorption band. A_{640} is a proportionality constant, also called the bond strength, depending on the frequency of the vibrating bond, and N_{Si} is the average number density of *a*-Si:H. In our case we used $N_{Si} = 5.3 \times 10^{22} cm^{-3}$ [148]. Different authors have proposed different values for the proportionality constant, but the most widely used is the one proposed by Langford *et al.* [148], $A_{640} = (2.1 \pm 0.2) \times 10^{19} cm^{-2}$. The band-stretching mode can also be used to calculate the hydrogen content in the sample according to the model proposed by Ouwens *et al.* [149]. In this case,

$$C_H = \frac{A_{2000} I_{2000} + A_{2100} I_{2100}}{N_{Si}}, \tag{4.83}$$

where A_{2000}, A_{2100} are the bond strengths for the peak at 2000 and 2100 cm^{-1} respectively, and I_{2000} and I_{2100} are their respective integral intensities.

3.2.2 FTIR Experimental Set up

All our FTIR experiments were conducted on a Perkin-Elmer Pentagon 1005 FTIR spectrometer, in a direct transmission sampling technique. The samples used were deposited on crystalline silicon, which has a good infrared transparency. Prior to deposition the substrate was cleaned in an ultrasonic bath for 5 minutes each in ethanol and acetone and also etched for 1 minute in HF acid to get rid of any kind of native oxide. The FTIR measurements were mainly conducted immediately after the deposition, except for the illuminated samples, to avoid the possibility of hydrogen escaping from the sample. In

order to obtain the infrared spectrum of the amorphous layer only, it was necessary to subtract the background spectrum caused by other infrared absorptions in the optical beam path. This was done by recording the spectrum of the uncoated crystalline substrate only. The Fourier transform of its interferogram was stored in the computer as the background spectrum. Then the spectrum of the coated sample on identical substrates was recorded in exactly the same way, Fourier transformed, and then ratioed against the background spectrum to get a transmittance spectrum. The wave number range was between 400 and 4000 cm^{-1}, with a resolution of 4 cm^{-1}.

Once the spectrum was collected different corrections discussed below, were performed in order to obtain reliable information regarding peak positions, intensity of the peak, and the shape of the baseline. Figure 67(a) below shows the infrared transmittance intensity $I(\omega)$ measured as function of the vibrational frequency (ω) for an *a*-Si:H sample deposited on a crystalline silicon substrate at 400°C

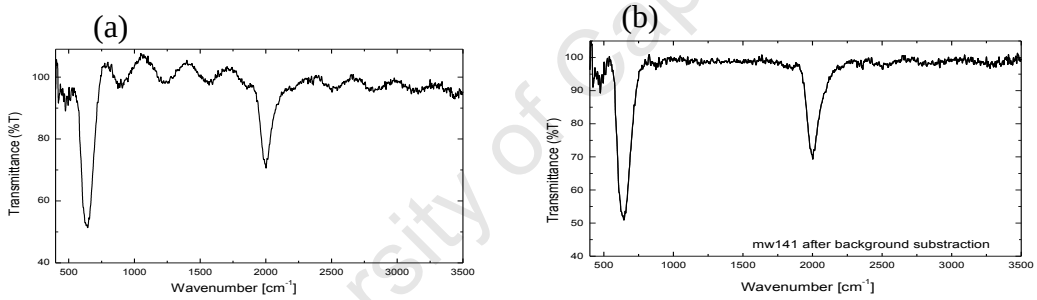

Fig.67: example of infrared transmittance spectrum from an amorphous layer deposited on *c*-Si substrate at 400°C: (a) raw data, (b) corrected intensity after the background subtraction showing well-defined peaks and a quite flat baseline in the region of interest.

The oscillating behaviour in the background is related to multiple reflection and interference in the thick layers. We recall that the thickness of our sample ranged between 1.5 and 4μm. These interference fringes may impact negatively on the exact localization of the peaks, or on the estimation of the intensity of the peaks, or, even worse, it may overshadow small peaks or small changes in peak position or peak intensity. This can lead to an over- or underestimated absorption in the film, and therefore an incorrect estimate of hydrogen content. A sinusoidal function taking into account the thickness of the measured sample, and sometimes tilted to match the slope of the background to be corrected, was adopted using the following phenomenological form

$$I_{background} = a + bx + c\sin(2\pi d - \theta), \tag{4.84}$$

where *a, b, c,* θ are constants and *d* is the layer thickness.

Figure 67(b) above shows the corrected intensity of the previous spectrum after background subtraction. It shows well-defined peaks and a quite flat baseline in the region of interest.

Multiple reflections from both the substrate (incoherent scattering) and the coated layer (coherent scattering) due to a slight difference in the refractive index of the substrate and the amorphous layer also cause an increase in the absorption in the film. The result of this is an increased effective absorption coefficient of the sample. To overcome this effect, a procedure introduced by Brodsky et al [150], known as the Brodsky-Cardona-Cuoma (BCC) correction helps to minimize the effect of incoherent scattering in the substrate. This method assumes that the amorphous layer and the substrate have the same refractive index, in which case the absorption coefficient can be corrected and related to the measured transmission *T(w)* by the following expression

$$T(\omega) = \frac{4T_0 e^{\alpha_{bcc} d}}{[(1+T_0)^2 - (1-T_0)e^{-2\alpha_{BCC} d}]}, \tag{4.85}$$

where α_{BCC} is the corrected absorption coefficient, *d* is the layer thickness and T_o is the baseline transmission, which is 0.54 for *c*-Si.

To account for the effect of coherent reflections in the *a*-Si:H layer we used the method proposed by Maley et al [151]:

$$\alpha_{true} = \alpha_{BCC} \text{ if } \omega d \geq 0.06,$$

$$\alpha_{true} = \frac{\alpha_{BCC}}{1.72 - 12\omega d} \text{ for } \omega d \leq 0.06. \tag{4.86}$$

3.2.3 FTIR Results and Discussion

a) Bonded Hydrogen in as-Deposited Samples

The infrared absorption spectra collected at room temperature for three samples deposited at 150, 300 and 500 °C are shown in figure 68. Except that the substrate heater temperature was varied, all other deposition conditions were kept constant. It appears that two strong absorption bands, one at 2000 cm^{-1} and the second at 640 cm^{-1}, mainly dominate the spectra. These bands are associated with the wag and stretch modes of vibration of monohydride (Si-H) bonded species respectively. There is also a very weak absorption band at approximately 880 cm^{-1} attributed to dihydrides $(Si\text{-}H_2)_n$ bonded species or polyhydride complexes $(Si\text{-}H_2)_n$ (isolated or clustered).

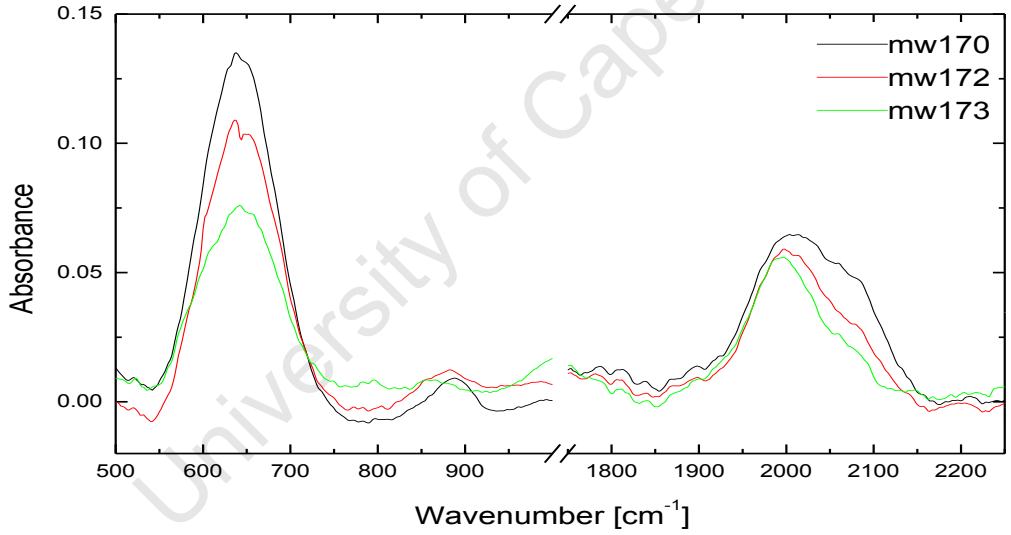

Fig.68: FTIR absorption spectra highlighting changes in hydrogen configuration is a-Si:H deposited on glass substrate as the deposition temperature increases from 150 °C (MW170), through 300°C(MW172), to 500°C (MW173).

From figure 68, it can be noticed that increasing the deposition temperature from 150 to 500 °C produces important changes in the absorption spectra. There is a noticeable decrease in the peak intensities as the deposition temperature increases. This change in the peak intensity can be related to the decrease in hydrogen content as the substrate temperature is increased. Furthermore, the suppression of the peak at 880 cm^{-1} indicates a

change in the configuration of hydrogen in the amorphous silicon matrix at a higher deposition temperature. Samples deposited at high substrate temperature do not exhibit any other peaks related to dihydrides ($Si-H_2$), polyhydrides $(Si-H_2)_n$ (isolated or clustered) or clustered monohydrides. This observation is in agreement with the literature [110] suggesting that such samples represent good electronic quality material, with only more stable Si-H bonds present.

There is a peak centred at around 2000 - 2100 cm^{-1}. This peak is both more pronounced and broader for samples deposited at lower substrate temperatures, and can be decomposed into two separate peaks. The peak centred at around 2000 cm^{-1}, associated with stretching mode of monohydride species, seems to increase with deposition temperature, while the one around 2100 cm^{-1} associated with the stretching mode of vibrations of the polyhydrides, dihydrides or clustered monohydrides, decreases with increased deposition temperature. As mentioned above, the ratio of the integral intensity of these peaks gives indication about the microstructure of the analysed sample. The behaviour of these peaks is therefore consistent with an increase in monohydride configuration, and therefore increasing network order as the deposition temperature is increased.

At this stage, our samples did not show any kind of oxidation expected, especially from the samples deposited at a lower substrate temperature, which was seen from the optical characterization to have a void rich micro-structure. This can be explained by the fact that FTIR measurements were performed immediately after deposition, and that the oxidation appears to be predominantly a post deposition process.

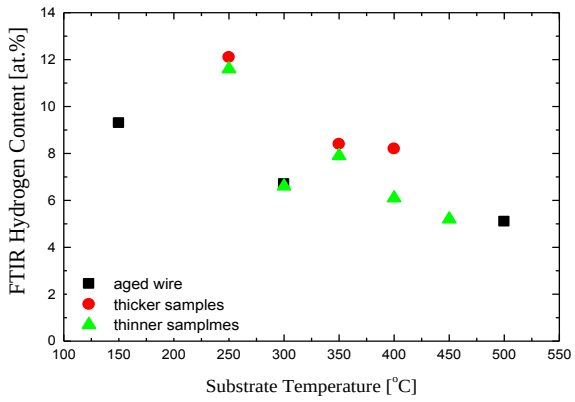

Fig.69: show the estimated bonded hydrogen content as a function of the deposition temperature as determined from FTIR spectroscopy.

Fig.69 shows that for all sets of samples, there is a general decrease in hydrogen content, from 12.1 at. % to 5.1 at. %, as the deposition temperature is increased from 150 to 500°C. Thicker samples deposited for 20 minutes possess more hydrogen compared to other samples deposited under otherwise identical conditions. This may be an artefact resulting from an overestimated sample thickness (see equation III.4.82). The Uv-vis methods used to estimate the sample thickness work better for thin layers, with thicknesses below 1μm, whereas ours are around 4μm.

b) Bonded hydrogen and light soaking

The idea of illuminating the samples for 12 and 48 hrs was based on our previous studies [107] where we have found out, from electron momentum spectroscopy, that the concentration or the size of defects in *a*-Si: H increases with illumination time within the first 16hrs, and then decreases on further illumination time reaching the initial value at around 40hrs.

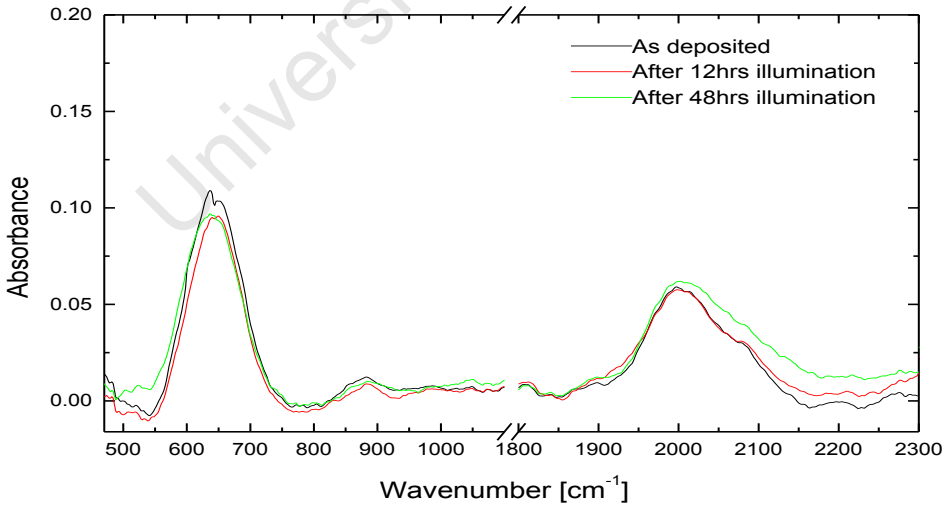

Fig.70: FTIR absorbance spectra of *a*-Si:H sample deposited at 300°C and illuminated at 0, 12 and 48hrs respectively

It should be noted that the samples were stored under ambient conditions in the dark for 2 years prior to the illumination studies and no significant changes were observed in the FTIR measurements and therefore the changes observed on illumination are entirely due to illumination. It can be observed in fig. 70 that there is a systematic decrease in the intensity of the 640 cm^{-1} band associated with the increase of illumination time. This result implies a decreasing hydrogen content as the illumination time is increased. However, the shoulder of the peak centered at 2000 - 2100cm^{-1} seems to become smoother and more intense as the illumination time is increased, suggesting that there are changes in the individual peak intensities. However no clear trend is seen for longer illumination for the sample deposited at 150°C although there is a similar increase for 12hrs illumination. It can therefore be concluded that the dihydride or polyhydride bonded species are not stable under illumination, and change to monohydride with increased illumination time.

3.3 Elastic Recoil Detection Analysis

As mentioned above, only the bonded hydrogen is infrared active, and therefore can be detected with FTIR technique. Hydrogen in *a*-Si:H can also be present in a molecular form. To get a clear picture of the amount of hydrogen in the samples studied, and to monitor its evolution with respect to the change in the substrate temperature or illumination time, another technique such as ERDA was needed to supplement the FTIR findings. ERDA is an ion beam analysis technique based on analysing collisions between high energetic incident ions and the atoms in the sample. In the case of *a*-Si:H layers this technique will give us information on the total hydrogen in the as-deposited sample, and after different illumination time intervals.

3.3.1 Basics of ERD Analysis

L'Ecuyer [152] first introduced the ERDA technique, which is now the most commonly used non-destructive ion beam analysis technique for depth profiling of light elements. The technique use an incident beam of energetic charged particles (^{4}He particles in our case) with mass m_1 and energy E_1, which are focused onto the target. The atoms in the target have mass m_2 and are initially at rest. As the incident heavier projectile ions collide with the lighter nuclei of the target, they scatter these due to the repulsive coulomb interaction. By analysing the recoil particles, which are scattered in the forward direction,

information regarding the mass, and therefore the atomic number, the depth distribution and concentration of the light elements in the sample can be obtained.

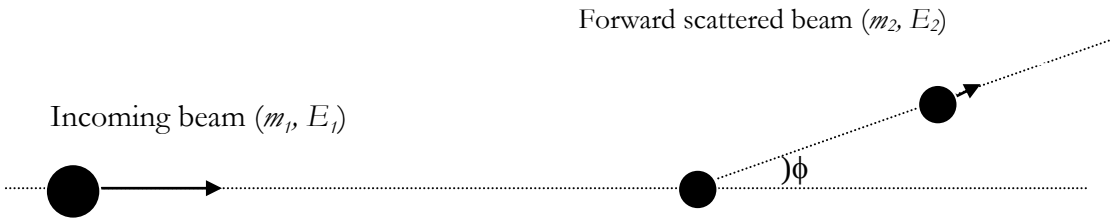

Fig.71: Schematic representation of the ERDA scattering experiment.

If an atom in the target recoils with energy E_2 in the direction making an angle φ with the incident beam, as shown in Fig 71, and the interaction between the incident ions and the nuclei of the target are assumed to be an elastic collision, the energy of the recoiled particles can be related to the energy of the incident ions by the kinematic factor K [153]

$$E_2 = KE_1. \tag{4.87}$$

The kinematic factor, defined as the ratio of the energy of the recoiled ions to that of the incident ions, is given by the following expression in the laboratory system and taking into account the conservation of energy and momentum [153]

$$K = \frac{E_2}{E_1} = \frac{4m_1m_2}{\left(m_1 + m_2\right)^2}\cos^2\varphi \tag{4.88}$$

where m_1 and m_2 are the incoming particle mass and the target nucleus mass respectively. From this equation it transpires that the kinematic factor depends not only on the masses of the incident beam ions and the atoms in the target, but also depends on the scattering angle φ. Knowing the kinematic factor allows mass determination, and hence element identification in the target, as the only unknown quantity is the target nucleus mass m_2.

Obviously all the incident particles may not scatter the atoms in the target, and even so the scattered atoms may not be scattered in the direction of the detector. Therefore the probability that one incident particle ejects a recoil atom in the direction of the detector can be described by the Rutherford differential scattering cross section. The Rutherford differential cross section $\frac{d\sigma}{d\Omega}$ gives an indication of detecting a scattered particle with the

detector spanning a finite solid angle Ω, situated at an angle φ with respect to the direction of the incident beam. Assuming an elastic Coulomb collision, the differential cross-section is expressed as [153]

$$\frac{d\sigma}{d\Omega} = \left(\frac{Z_1 Z_2 e^2 (1 + m_1 / m_2)}{2E_1} \right)^2 \frac{1}{\cos^3 \varphi}, \tag{4.89}$$

where e is the elemental charge, and Z_1 and Z_2 the atomic numbers of the incident and target atoms respectively. This equation shows clearly that the heavy projectiles scatter target atoms more efficiently than light ions.

In a more realistic situation we do not assume that the recoiled atoms are at the surface, but at an arbitrary depth x. In this case we need to take into account the energy loss of the incident ions along the inward path and the energy loss of the recoiled ions along the outward path. As illustrated schematically in fig 72, the incident ion with mass M_1 and energy E_0 enter the surface at an angle θ_1 with respect to the surface normal. It then penetrates the sample on nearly straight trajectory and loses energy before colliding with a target atom of mass M_2 at a depth x. At this depth the incident ion has energy E_0' and transfers energy E_2 to the recoiled atom. The recoiled atom scatters at an angle φ relative to the incident beam direction and loses energy while moving back to the surface, where it leaves with energy E_3 at an angle θ_2 relative to surface normal before entering the range foil, where it will also lose energy before being finally detected with an energy E_d.

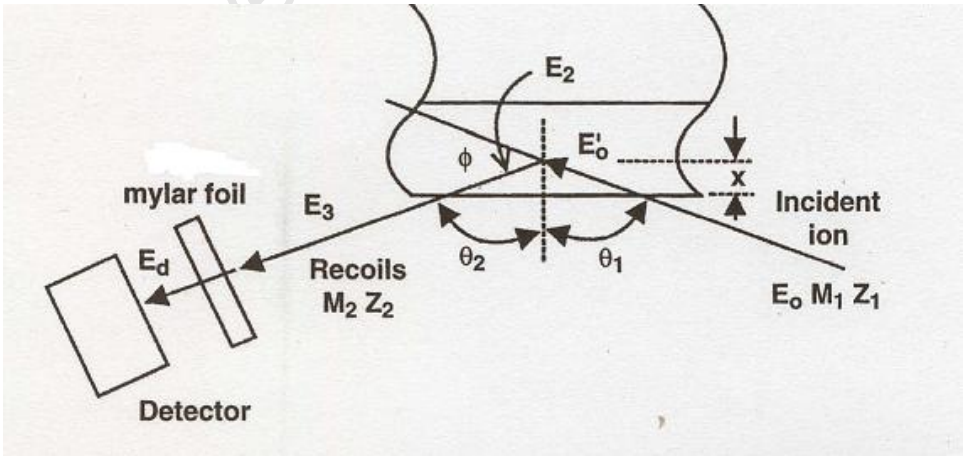

Fig.72: Schematic diagram of experimental setup of ERD showing the geometry of the incident ion and recoiled particle [146].

Taking the average energy losses $\left[\frac{\partial E}{\partial x}\right]_{in}$ and $\left[\frac{\partial E}{\partial x}\right]_{out}$ for the incident ions, along the entering path, and the recoiled particle leaving the sample respectively, the energy of the recoiled atom from a depth x can be given by the following expression [153]

$$E_3 = K\left(E_0 - \frac{x}{\cos\theta_1}\left[\frac{\partial E}{\partial x}\right]_{in} - \frac{x}{\cos\theta_2}\left[\frac{\partial E}{\partial x}\right]_{out}\right). \tag{4.90}$$

If we choose the incident angle to be identical to the exit angle, and name it θ, a linear relationship can be established between the energy of the recoil atom at the sample surface and the depth where the atom is ejected:

$$E_3 = KE_o - Cx, \tag{4.91}$$

where the constant C is given by

$$c = \frac{1}{\cos\theta}\left[K\left(\frac{\partial E}{\partial x}\right)_{in} + \left(\frac{\partial E}{\partial x}\right)_{out}\right]. \tag{4.92}$$

The detected energy is therefore a function of the depth of the scattering atoms in the sample. Atoms near the sample surface will exit with a high energy, as they are not subjected to stopping in the sample.

For a constant concentration of the target atoms, the number of detected particles is related to the number of target atoms per cm^2 by the following formula [153]

$$Y = Q\Omega N\int_0^{E_1}\frac{d\sigma}{d\Omega}(E,\varphi)\left(\frac{dE}{dx}\right)^{-1}dE, \tag{4.93}$$

where Q is the total flux of ions in the incident beam. A plot of yield as a function of energy gives the information about the elemental concentration and its distribution. In our study we were interested primarily in the total concentration of hydrogen in the *a*-Si:H samples.

3.3.2 ERDA Experimental Set up

The ERDA measurements were conducted using the facility at iThemba LABS, with a 3 MeV mono-energetic beam of He ions accelerated by a single ended van de Graaff accelerator. The samples were mounted on a sample holder oriented at an angle of 15° with respect to the direction of the incident beam, and placed in an evacuated chamber at

approximately 1.52×10^{-4} mbar. The sample holder, with a capacity for ten samples is fixed on a ladder which moves vertically up and down in the chamber.

After the collision the recoiled atoms are detected by a silicon surface barrier detector positioned symmetrically in the direction making an angle φ of 30° with the incident beam direction. A total charge of 5000 nC was collected each time with the current between 9 and 20 nA. In order to prevent any alpha particles, scattered by the Si atoms from the target, from reaching the detector and interfering with the normal layer response, a Mylar range foil of approximately 12.5μm thick was placed in front of the detector so that only hydrogen was detected.

The data output from the detector is collected by a multichannel analyser as a number of counts recorded in each channel corresponding to an energy interval. As the aim of the ERDA measurement is to obtain a depth profile of hydrogen and its content in our sample, we had to convert these data from the channel number to particle energy. It should be noted that because ERDA is an energy loss spectroscopy, recoils from near the surface, which have lost less energy occur at a higher channel number. A reference sample of known hydrogen concentration was measured in the same condition as the sample at 3 different energies, for energy and geometry calibration. In this study a 12.7 μm thick Kapton ($C_{22}H_{10}N_2O_4$) sample was used at beam energies of 2, 2.5 and 3 MeV. The following figure shows the energy calibration used in the experiment.

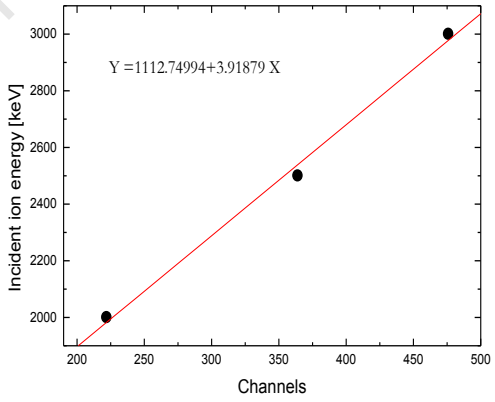

Fig.73: The energy-channel calibration for the ERDA experiment.

3.3.3 ERDA Results and Discussion

a) Total Hydrogen Content in as Deposited Samples

Illustrative ERDA spectra from three samples deposited on glass substrates at 300, 400 and 500°C are shown in figure 72 below.

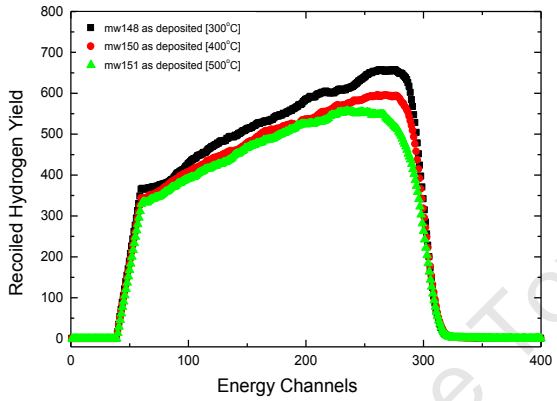

Fig.74: Typical ERDA spectra for three samples deposited at different substrate temperatures.

It is apparent from the spectra that in principle the hydrogen was recoiled, and detected, uniformly from throughout the sample thickness. The graphs show a general increasing hydrogen yield from the bulk to the sample surface, even if for certain samples the slope may vary around an average value, indicating a certain inhomogeneity in hydrogen distribution around an average hydrogen content in that particular sample. It can also be noticed that the amount of hydrogen at the sample surface, and throughout the first few monolayers, particularly for samples deposited at relatively low temperature, is higher than the amount of hydrogen in the bulk. These samples can be described as porous, with a significant concentration of microvoids where the detected hydrogen may be accommodated.

As the substrate temperature is increased, the slope of the hydrogen yield decreases. This can be interpreted as the hydrogen concentration decreasing as the growth temperature is increased. This agrees with the increase in refractive index with the deposition temperature, indicating a denser material produced at elevated temperature. The FTIR results also show that the hydrogen in these samples is present mainly in a monohydride configuration. We

recall that dihydrides or polyhydrides are mainly trapped in voids, or between grain boundaries for samples comprising partly crystalline structures [82].

It can also be noticed that by increasing the growth temperature, a hydrogen-depleted near surface region appears that accentuates with increased temperature. This effect may be associated with denser samples that do not leave paths for water vapor molecules, but also to the desorption-diffusion process, which is temperature dependent [154].

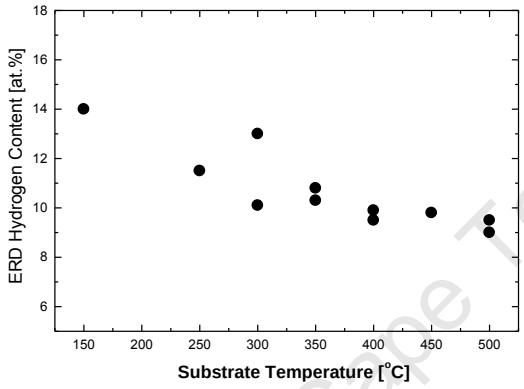

Fig.75: Hydrogen content estimated from the ERD measurements as a function of the deposition temperature.

Figure 75 shows the estimated total hydrogen content for all samples. From the figure it can be seen that there is a general decrease in the total hydrogen content as the growth temperature is increased. Samples deposited at the same substrate temperature generally contain a similar amount of hydrogen, except for two samples deposited at 300 °C. Figure 76 below compares the concentration of bonded hydrogen, measured with FTIR, with the total hydrogen in the same samples as the substrate temperature was varied from 150 to 500°C.

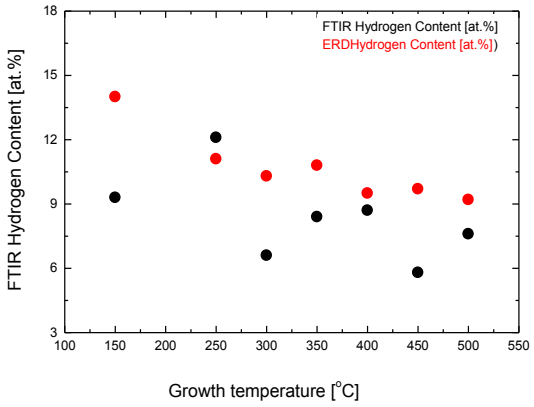

Fig.76: changes in bonded hydrogen compared to changes in total hydrogen as the substrate heat temperature varies from 150 to 500°C.

b) Total Hydrogen and Light Soaking

The degradation in electrical and optical properties of devices, fabricated out of *a*-Si:H, after a prolonged illumination has been associated with the change in hydrogen content [21]. The breaking of weak Si-Si bonds in *a*-Si:H and therefore the creation of dangling bonds, acting as recombination centres, is triggered by the presence of hydrogen in the vicinity of the of the weak bond. On the other hand hydrogen is reported to passivate the dangling bonds and therefore minimizing the defects in the material [24]. It is not yet established if it is the bonded or the total hydrogen which is involved in the degradation process, and therefore the changes in both need to be monitored, and eventually associated with the change in other parameters. Figure 75 below illustrates the changes in hydrogen yield for three different *a*-Si:H samples as the illumination time is increased.

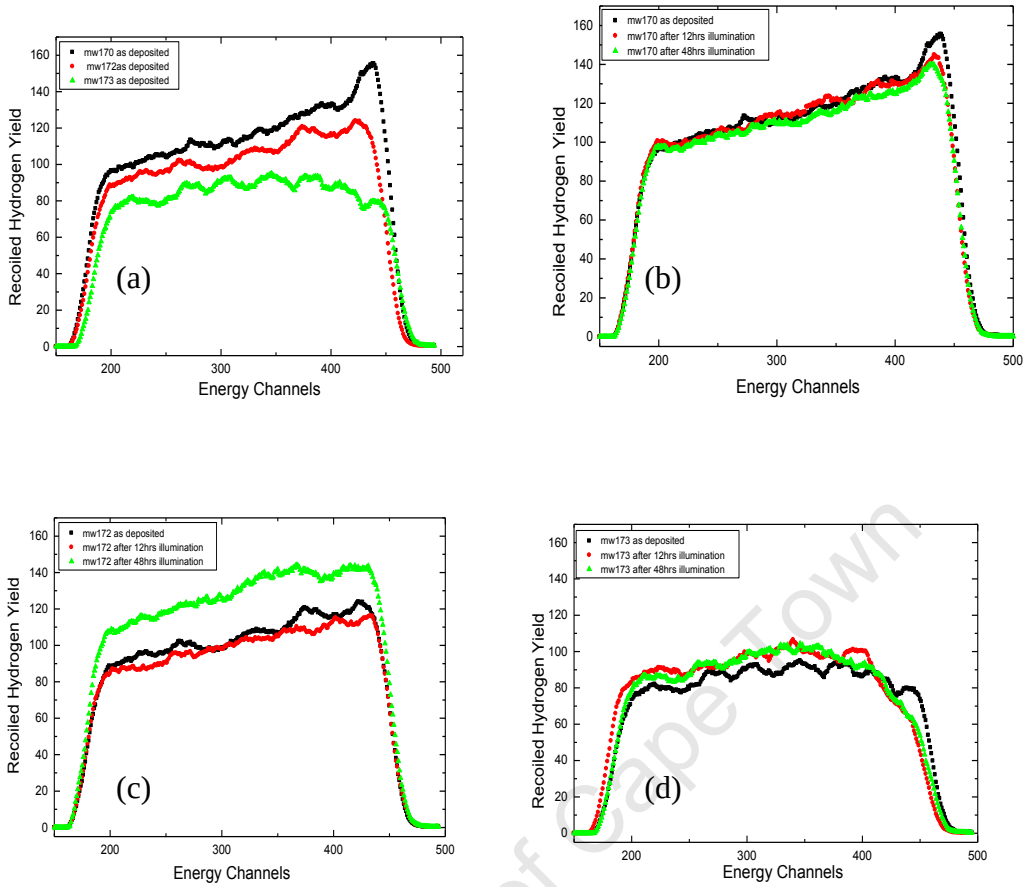

Fig.77: ERD spectra for *a*-Si:H layers deposited at different temperature and at different illumination time: (a) As deposited Td_1, Td_2, Td_3; (b) Td_1=150°C, illumination time 0, 12, 48hrs; (c) Td_2=300°C, illumination time 0, 12, 48hrs; (d) Td_3=500°C, illumination time 0, 12, 48hrs.

All the spectra show an increasing hydrogen yield moving from deep in the bulk towards the sample surface. This is indicative of a generally uniform hydrogen concentration deep in the sample, with the loss in yield being solely due to stopping of the recoiled H. In the as-deposited state (fig 77(a)), for the sample deposited at 150°C (mw170) there is an obvious enhancement of H near the surface. As discussed before, this is probably due to increased porosity in the near surface region. In contrast the surface H concentration appears to be depleted in sample mw173, deposited at 500°C. A close look at figures 77 (b), (c) and (d) shows that for each sample the average slope of the hydrogen yield, as a function of the energy, decreases as the illumination time is increased. Changes are more significant in the near surface region where the hydrogen-depleted region seems to increase with illumination time. Another observation concerns the oscillations around the average slope, associated with inhomogeneity in the hydrogen distribution, which seem

to move from the surface into the bulk as the illumination time is increased. This is a clear indication of the hydrogen migration and must be seen as an effect of illumination rather than any heating, as it is more pronounced in the near surface region. The amount of light reaching the surface is greater than the amount reaching the bulk due to absorption in the layer. It can also be noticed that the irregularities in the hydrogen distribution flatten with increasing illumination time.

The elastic recoil spectra have been simulated with a two zone model of the hydrogen profile using the program RUMP. The results of this analysis are summarised in Table 11, and the surface hydrogen concentration plotted in fig 78.

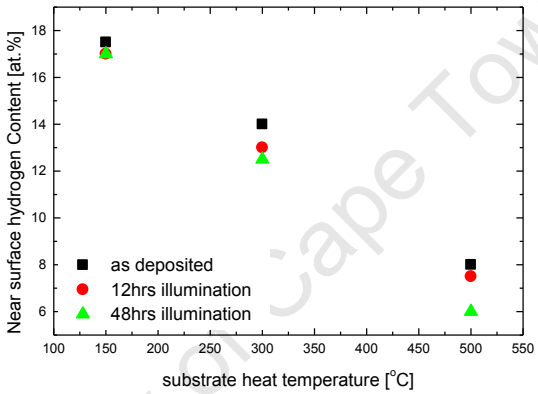

Fig.78: Effect of illumination time on the near surface hydrogen concentration for different temperatures

From figure 78 it can be noticed that, in general, there is a consistent decrease in the near surface hydrogen as the illumination time is increased. The magnitude of this decrease seems to increase with the growth temperature. This can be explained by the fact that the effective thickness of the layer, we are interested in, is a function of the deposition temperature and increases with a decrease in deposition temperature. Thus for the sample deposited at rather a low temperature the small change in hydrogen content is compensated by the change in the layer thickness as it changes from 150nm to 110nm after illumination. In contrast, there is little or no change in the bulk hydrogen concentration on illumination, confirming that this a light induced, and not a thermal effect.

Sample ID	Near surface H [at. %]	Bulk H [at. %]	Near surface layer thickness [nm]
Mw170-ohrs	17.5	14	150
Mw170-12hrs	17	14	130
Mw170-48hrs	17	14	110
Mw172-ohrs	14	13	100
Mw172-12hrs	13	13	-
Mw172-48hrs	12.5	12.5	-
Mw173-ohrs	8	10	210
Mw173-12hrs	7.5	9	230
Mw173-48hrs	6	10	320

Table 11: highlighting the changes in near surface and the bulk hydrogen of the illuminated samples as the deposition temperature varies from 150^{o}C to 500^{o}C.

IV. DISCUSSION

1. DISCUSSION

In the preceding chapters, *a*-Si:H deposited at different substrate temperatures has been characterized with respect to its structure and hydrogen content. The influence of growth temperature and the effect of illumination, on the residual stress, hydrogen concentration, and the opto-electronic properties have been investigated independently. As the main objective of this study was the investigation of the interdependence of microstructure, stress and defects, and their evolution under illumination, it is the aim of this section to bring these independent observations together in a consolidated discussion. The first chapter will discuss the mutual relationship between intrinsic stress and the hydrogen related defect configuration, and their influence on the optical parameters. In the second chapter the evolution of the material characteristics under illumination will be discussed.

1. Effect of the Deposition Temperature on *a*-Si:H

From the optical measurements, the direct bandgap, of the *a*-Si:H layers analysed, decreases with increasing deposition temperature, and somehow saturates at around 1.66 eV above 300 ^{0}C. Both the observed decrease and the saturation are in agreement with the literature [107]. In [46] the bandgap behaves in similar way to that measured in this work and does not decrease further below 1.65eV for a sample with a hydrogen concentration of 0.1 at. %. Similarly, the absorption coefficient and the refractive index both increase and saturate at around 350 ^{0}C, which is also in agreement with observations in the literature. It can be concluded from these measurements that the optimum growth temperature is between 300 and 350 ^{0}C, as there seems to be no significant increase of the densification, or improvement of the structure of the layer beyond this deposition temperature.

The effect of the deposition temperature on the hydrogen content and bonding arrangement was analysed using a combination of FTIR and ERD techniques. It appears from these measurements that the bonded hydrogen concentration decreases with increasing deposition temperature, but unlike the optical properties does not seem to saturate in the temperature range studied. Also, the relative fraction of the monohydride, compared to

polyhydride configuration increases systematically and continuously with the deposition temperature. Both of these trends are consistent with observations made by other authors [20]. As previously observed, the ERDA measurements showed that the total hydrogen content in the layer decreases with the deposition temperature, and does saturate at around 350 ^{0}C. It can be deduced, from both measurements, that the relative fraction of free hydrogen may increase slightly with the deposition temperature, as the total hydrogen concentration remains constant, while the bonded hydrogen continuously decreases for further increase in deposition temperature. This, combined with the decrease in the bandgap, as the deposition temperature is increased, leads to the question of where the non-bonded hydrogen could be located. Because of the increased densification, and therefore less open volume in the layer, and reduced polyhydride content, this non-bonded hydrogen cannot reside at small voids or dangling bond clusters. Large voids, with a low surface to volume ratio, would be visible in electron micrographs. However, we do not know of such observations in similar samples. At high temperature the non-bonded hydrogen may either be present in interstitial form in the amorphous matrix [74], or be confined to domain boundaries.

Diffraction measurements, on the other hand, showed better resolved peaks at high deposition temperature. The same trend was also seen in the pair correlation function, where less scatter in the nearest neighbour distances is observed. This means that *a*-Si:H with improved structural order is grown at higher temperature. The largest difference occurs between 150 ^{0} and 300 ^{0}, while the structure at 500 ^{0}C is broadly similar to that 300 ^{0}C. All these observation are in agreement with our general expectations and previous observations in the literature [122].

In general the residual stress, estimated from the first diffraction peak using the $\sin^2\psi$ method, was compressive at a low deposition temperature, became slightly tensile at intermediate temperature, and finally became compressive again as the deposition temperature was increased to 500 ^{0}C. The stress estimated from the second peak in reciprocal space and the second nearest neighbour peak, showed a compressive stress, which increased with the deposition temperature. While the bond stress, estimated from the nearest neighbour peak in the pair correlation function, was tensile for low temperature growth and changed to compressive at a high temperature, the anisotropy in the layer, estimated from the difference in the principal stresses, decreased with deposition temperature. In all cases the $\sin^2\psi$ plots indicate a nonlinear behaviour compatible with a

two stress zone model. These two zones become more pronounced at higher deposition temperature.

The generally increasing compressive stress with the deposition temperature is due to the thermal mismatch contribution to the total stress in the sample. The coefficient of thermal expansion of *a*-Si:H is small compared with that of glass. Therefore the thermal mismatch stress in the layer will always be compressive, and will increase with the deposition temperature. A compressive stress observed at low deposition temperature, from the first diffraction peak in reciprocal space equivalent to the tetrahedron height, therefore suggests that polyhydrides and high disorder at a low temperature give rise to compressive intrinsic stress. Similarly the tensile stress, dominant in the structure of the layer deposited at 300 ^{0}C, suggests that the monohydride configuration is a cause of tensile intrinsic stress. This is in contradiction to macroscopic observations [44], where monohydride is associated with compressive stress, and polyhydrides with tensile.

This dilemma can be resolved, if we consider the macroscopically determined stress as describing the stress in the bond length r_1, and the edge of the tetrahedron r_2, as shown in figure 77. In the figure, the white points represent the initial unstrained configuration, and the black represent the strained configuration. If r_1 is shortened, r_2 will necessarily also be reduced as shown in the figure. However, if there is also an increase in the bond angle, in the plane of the stress, the height of the tetrahedron d_{111} may increase. The expected observation would then be: compressive strain for r_1, r_2, and d_{220} (which is equivalent to r_2); and a tensile strain in d_{111}. We recall, that the bond angle changes normally recorded are for the complementary angle, perpendicular to the plane of the layer, which is generally observed to decrease [74], as would be expected from the figure. It should also be noted that the relative change in r_2 is small compared to the changes in r_1 and d_{111}. This situation is exactly what is reported in chapter III.2.5 for increasing deposition temperature, and hence for an increasing fraction of Si-H bonds, or decreasing fraction of Si-H_n.

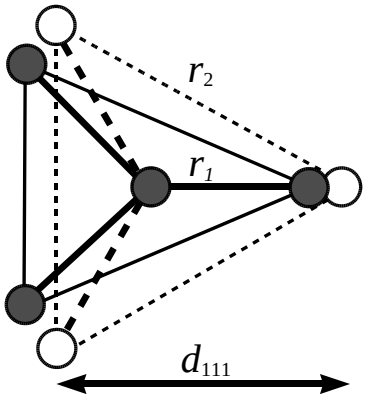

Fig.79: Sketch showing that a compressive strain in the bond r_1, and the edge of the tetrahedron r_2, can result in a tensile strain of the height of the tetrahedron d_{111}, if the bond angle strain is positive.

It can therefore be concluded that polyhydride bonds and voids are sources of tensile stress for the bond length, and that the presence of Si-H bonds relax this strain. It is also possible that monohydrides are sources of compressive stress, but this is not necessary to account for the observations.

The structure of samples deposited beyond a temperature of 300 ^{0}C has reached an optimum for electronic and optical properties. Higher temperatures result in only slight changes in the structure, but increase the thermal mismatch stress. As the compressive extrinsic stress is increased, hydrogen is forced away from bonds, and this leaves questions as to where it goes.

2. Effect of Illumination on *a*-Si:H

In this study, the effect of illumination was also investigated. The optical measurements, conducted on this set of samples did not show any significant changes in the bandgap, or other optical parameters after 12 or 48 hrs illumination. We can therefore suggest that these changes are related to the network structure, and not to the defect states.

If the measurements are insensitive to details of defect states in the band tails, this observation could have been expected from general consideration of any crystalline semiconductor.

Upon illumination, FTIR showed a decrease in the total bonded hydrogen, and ERD measurements similarly showed a near surface depletion of hydrogen, for samples grown at high temperature. This suggests that the hydrogen migration is activated by illumination. It was also shown that the relative monohydride to polyhydride ratio increased continuously over the 48 hrs illumination, and that the relative free to bonded hydrogen ratio decreased at the surface for growth above 300^0C. Under these conditions, it can be suggested that molecular hydrogen is immobilised in voids at a low deposition temperature, but resides elsewhere for high deposition temperature. Interstitial molecular hydrogen is suggested to be the diffusing species. It can dissociate at single dangling bonds resulting in relatively immobile monohydride, but could also desorbed from dangling bond complexes to produce polyhydrides. The latter reaction may be probable as it provides two H near to each other, which can form the mobile H_2.

The $\sin^2\psi$ plots from the illuminated samples clearly show two regions. This observation is consistent with the near surface changes of the hydrogen configuration, which are associated with increased compressive stress on illumination. The overall stress becomes more compressive over short illumination, and a general relaxation may be observed on longer illumination, as the depth affected by hydrogen migration increases.

V. CONCLUSION

1.CONCLUSION

Hydrogenated amorphous silicon is a widely used thin film semiconductor material which is still incompletely understood. The structure of *a*-Si:H is assumed to form a CRN of Si-Si_4 tetrahedra which are highly strained with a high concentration of dangling bond defects, which are passivated by hydrogen. Upon illumination the electronic properties of this material degrade, but the mechanism behind this effect is not yet fully understood and is still a challenge to physicists and engineers. The aim of this study was first to investigate the relation between the structure, the stress and hydrogen distribution in *a*-Si:H, and secondly to investigate the influence of illumination on hydrogen evolution and its relationship with strain in the material.

The *a*-Si:H samples used in this study were deposited simultaneously on both *c*-Si and Corning glass substrates at different temperatures, between 150 and 500 ^{0}C, using a HWCVD technique with pure silane as reactive gas. The optical parameters, band gap, refractive index, and absorption coefficient were estimated using UV-Visible absorption spectroscopy, which also allowed us to estimate the thickness of the deposited layers. Bonded hydrogen content, and its configuration, in *a*-Si:H were analysed using FTIR spectroscopy, while the total hydrogen was estimated from ERDA. The structure and the stress were investigated using synchrotron radiation diffraction on a set of selected samples. These results were analysed in two approaches: either as direct diffraction patterns in reciprocal space, or after being Fourier transformed as a pair correlation function in real space.

To investigate the influence of illumination, the selected set of samples was illuminated for a period of 12 and 48 hrs each, using a metal halide lamp, housed in a mirrored chamber. The illuminance at the sample stage was 110 Wm^{-2}. The changes in stress, hydrogen content and bonding and optical properties were monitored using the above mentioned techniques.

The effect of the deposition temperature on optical properties of the samples analysed shows that the best sample is grown between 300 and 350 ^{0}C, as there seems to be no significant changes in the band gap, absorption coefficient or refractive index above this deposition temperature. Similarly, diffraction measurements showed an improved structural

order with increasing deposition temperature, with most changes happening between 150 and 300 ^{0}C. Both the bonded hydrogen and the total hydrogen content decreased with increased deposition temperature. However the relative fraction of free hydrogen was seen to increase with the deposition temperature. Taking into account the increased densification of the sample, it was suggested that the hydrogen may be present in the sample either as an interstitial [74] or in the domain boundaries.

In general the stress, estimated from the first diffraction peak, is compressive at a low deposition temperature, becomes slightly tensile for intermediate temperatures, and finally becomes compressive again as the deposition temperature is increased to 500 ^{0}C. The stress estimated from the second peak in reciprocal space and the second nearest neighbour peak, show a compressive stress increasing with the deposition temperature. The bond stress, estimated from the nearest neighbour peak in the pair correlation function, is tensile at a low temperature, but changes to compressive at a high temperature. This behaviour suggests that the native defects for low temperature deposition, which are multiply passivated dangling bond clusters with a polyhydride configuration, are a source of tensile intrinsic stress. For higher temperature deposition Si-H bonds may either be sources of compressive stress, or simply serve to relax the existing stress.

There were no significant changes in the optical properties of the *a*-Si:H after 48 hrs of illumination. We assume that the techniques used were not sensitive to details of defect states in the band tails. From the FTIR measurements, a decrease in total bonded hydrogen is observed with increased illumination. ERD measurements show a near surface depletion of hydrogen, with illumination time, for samples deposited at temperatures above 300 ^{0}C. This was seen as an indication that the hydrogen migration is activated by illumination. It was also shown that the relative monohydride to polyhydride ratio increases continuously over the 48 hrs illumination, and that the relative free to bonded hydrogen ratio decreases at the surface for growth above 300 ^{0}C. Under these conditions, it can be suggested that the H is immobilised in voids at a low deposition temperature, and located elsewhere for high deposition temperature. Interstitial molecular hydrogen is therefore suggested to be the diffusing species [155]

The overall stress becomes more compressive over short illumination, and a general relaxation may be observed on longer illumination as the depth affected by

hydrogen migration increases overall. This is consistent with the main sources of intrinsic stress being tensile, and probably multiply hydrogenated dangling-bond clusters [156].

This study could not provide definite answers to a certain number of questions, such as the location of the free hydrogen in the samples deposited at high temperature. Also, as the compressive stress observed at a high deposited temperature may result from the thermal mismatch compressive stress, this study could not explain if the intrinsic stress for high temperature growth is compressive, or even if there is any intrinsic stress at all.

As the $\sin^2\psi$ plots indicated that there is a stress gradient, future work should focus on the determination of the depth triaxial stress [129]. However this will require a significant extension of the synchrotron diffraction techniques, including determination of the true diffraction elastic constants, under applied load, for all peak studies. Further future work could also focus on separation of intrinsic and extrinsic stress by temperature dependent measurements. This would need a narrow temperature range below the room temperature to avoid thermally activated changes to the metastable structure, which have been seen to occur between room temperature and the deposition temperature [9]. Additional complementary techniques such as positron annihilation spectroscopy could also be used to gain insight on defect structure and defect evolution with illumination, while TEM can be used to gain information on local structure and possibly the strain in the *a*-Si:H layers.

REFERENCES

[1] K. Tanaka, E. Maruyama, T. Shimada, and H. Okamoto, *Amorphous Silicon*, John Wiley & Sons, New York, USA (1999).

[2] J.S. Blakemore, *Solid State Physics*, W.B. Saunders Company, Philadelphia (1969).

[3] S.R. Elliott, *Physics of amorphous materials* (2nd edition), Longman group limited, London, UK (1990).

[4] S.R. Elliott, Adv. Phys., Vol. **38** (1989) 1 - 88.

[5] A.C. Wright, J. Non-Cryst. Solids **179** (1994) 84 - 115.

[6] P.M. Voyles, J.R. Abelson, Solar Energy Materials and Solar Cells **78** (2003) 85 – 113

[7] D.L. Williamson, in *Amorphous and Heterogeneous Silicon Thin Films: Fundamentals to Devices—1999*, edited by H. M. Branz, R. W. Collins, H. Okamoto, S. Guha, and R. Schropp, MRS Symposia Proceedings No. **557** (Materials Research Society, Pittsburgh, 1999), p. 251.

[8] K. Morigaki, *Physics of Amorphous Semiconductors*, World Scientific, Singapore (1999).

[9] D.T. Britton, A. Hempel, M. Härting, G. Kögel, P. Sperr, W. Triftshäuser, C. Arendse, and D. Knoesen, Phys. Rev. B **64** (2001) 075403.

[10] S.C. Moss and J.F. Graczyk, Phys. Rev. Lett. **23** (1969) 1167 - 1171.

[11] R. Bellisent, A. Menelle, W.S. Howells, A.C. Wright, T. M. Brunier, R. N. Sinclair and F. Jansen, Physica B **156 - 157** (1989) 217 - 219.

[12] A.D. Krawitz, *Introduction to Diffraction in Materials Science and Engineering*, John Wiley & Sons, New York, USA (2001).

[13] D.E. Polk, J. Non-Cryst. Solids **5** (1971) 365 - 376.

[14] R. Grigorovici, and R. Mănăilă, J. Non-Cryst. Solids **1** (1969) 371 - 387.

[15] W. H. Zachariasen, J. Am. Chem. Soc. **54** (1932) 3841 - 3851.

[16] D.E. Polk, Phys. Rev. Lett. **31** (1973) 92 - 95.

[17] R.A. Street, *Hydrogenated Amorphous Silicon*, Cambridge University Press, Cambridge, UK (1991).

[18] A. Madan and M.P. Shaw, *The Physics and Applications of Amorphous Semiconductors*, Academic Press, San Diego, USA (1988).

[19] G. Ganguly, A. Matsuda, Phys. Rev. B **47** (1993) 3661 - 3670.

[20] H. Fritzsche, Ann. Rev. Mater. Res. **31** (2001) 47 - 79.

[21] J.D. Cohen, Sol. Energy Mater. Sol. Cells **78** (2003) 399 - 424.

[22] D. Adler and E.J. Yoffa, Phys. Rev. Lett. **36** (1976) 1197 - 1200.

[23] W.B. Jackson and C.C. Tsai, Phys. Rev. B **45** (1992) 6564 - 6580.

[24] R. Biswas and B.C. Pan, Sol. Energy Mater. Sol. Cells **78** (2003) 447 - 467.

[25] Y. Hishikawa, K.Watanabe, S. Tsuda, S. Nakano, M. Ohnishi, and Y. Kuwano, J. Non-Cryst. Solids **97 - 98** (1987) 399 -402.

[26] P. Danesh, B. Pantchev, I. Savatinova, E. Liarokapis, and B. Schmidt, Vacuum **69** (2003) 83 - 86.

[27] D.E. Carlson and C.R. Wronski, Appl. Phys. Lett. **28** (1976) 671 - 673.

[28] A.F. Meftah, A.M. Meftah, and A. Merazga, J. Phys.: Condens. Matter. **16** (2004) 3107 - 3116.

[29] S. Michaelson, A. Hoffman, Diamond and Related Materials, **15** (2006) 486 - 497.

[30] M. Stutzmann, W.B. Jackson, and C.C. Tsai, Phys. Rev. B **32** (1985) 23 - 47.

[31] H.M. Branz, J. Non-Cryst. Solids **266 - 269** (2000) 391 - 396.

[32] E. Minani, Z. Sigcau, T.P. Ntsoane , D. Knoesen, C.M. Comrie, D.T. Britton, and M. Härting, Mat. Sci. Forum **445 - 446** (2004) 147 - 149.

[33] S. Yamasaki, H. Okushi, A. Matsuda, K. Tanaka, and J. Isoya, Phys. Rev. Lett. **65** (1990) 756 - 759.

[34] P. O'Connor and J. Tauc, Phys. Rev. B **25** (1982) 2748 - 2766.

[35] W.B. Jackson and N.M. Amer, Phys. Rev. B **25** (1982) 5559 - 5562.

[36] J.I. Pankove, M.A. Lampert, and M.L. Tarng, Appl. Phys. Lett. **32** (1978) 439 - 441.

[37] S.B. Zhang and H.M. Branz, Phys. Rev. Lett. **87** (2001) 105503.

[38] W.E. Carlos and P.C. Taylor, Phys. Rev. B **26** (1982) 3605

[39] J.W. Corbett, S.N. Sahu, T.S. Shi, and L.C. Snyder, Phys. Lett. A **93** (1983) 303 - 304.

[40] W.M.M. Kessels, A.H.M. Smets, D.C. Marra, E.S. Aydil, D.C. Schram, and M.C.M van de Sanden, Thin Solids Films **383** (2001) 154 - 160.

[41] J. Robertson, J. Appl.Phys. **87** (2000) 2608 - 2617.

[42] B. Pantchev, P. Danesh, B. Schmidt, Appl. Phys. Lett. **87** (2005) 023104.

[43] P. Danesh and B. Pantchev, Semicond. Sci. Technol. **15** (2000) 971 - 974.

[44] K.S. Stevens and N. M. Johnson, J. Appl. Phys **71** (1992) 2628 - 2631

[45] K.L. Choy, Progr. Mater. Sci. **48** (2003) 57 - 170.

[46] A.H. Mahan, J. Carapella, B.P. Nelson, R.S. Crandall, I. Balberg, J. Appl. Phys. **69** (1991) 6728 - 6730.

[47] A.R. Middya, J-J. Liang, and K. Ghosh, J. Non-Cryst. Solids **352** (2006) 1008 - 1010.

[48] E.A..G. Hamers, A. Fontcuberta i Morral, C. Niikura, R. Brenot, and P. Roca i Cabarrocas, J. Appl. Phys. **88** (2000) 3674 - 3688.

[49] R. Dewarrat and J. Robertson, Thin Solid Films **427** (2003) 11 - 15.

[50] H.Wiesmann, A.K. Ghosh, T. McMahon, and M. Strongin, J. Appl. Phys. **50** (1979) 3752 - 3754.

[51] H. Matsumura and H. Tachibana, Appl. Phys. Lett. **47** (1985) 833 - 835.

[52] H. Matsumura, Jpn. J. Appl. Phys. **25** (1986) L949 - L951.

[53] J. Doyle, R. Robertson, G.H. Lin, M.Z. He, and A. Gallagher, J. Appl. Phys. **64** (1988) 3215 - 3223.

[54] N. Honda , A. Masuda , and H. Matsumura, J. Non-Cryst. Solids **266** (2000) 100 - 104.

[55] S Tange, K Inoue, K. Tonokura, and M Koshi, Thin Solid Films **395** (2001) 42 - 46

[56] J. Perrin, O. Leroy, and M.C. Bordage, Contrib. Plasma Phys. **36** (1996) 3 - 49.

[57] W. Zheng, A. Gallagher, Thin Solid Films **516** (2008)929-939.

[58] K. Winer, Phys. Rev. B **41** (1990) 7952 - 7954.

[59] R.A. Street, Phys. Rev. B **43** (1991) 2454 - 2457.

[60] S. Yamasaki, Mater. Res. Soc. Symp. Proc. **609** (2000) A.1.1.

[61] A. Gallagher, Mater. Res. Soc. Symp. Proc. **70** (1986) 3.

[62] A Matsuda and K. Tanaka, J. Appl. Phys. **60** (1986) 2351 - 2356

[63] J. Perrin, Y. Takeda, N. Hirano, Y.Takeuchi, and A. Matsuda, Surf. Sci. **210** (1989) 114 - 128.

[64] A. Matsuda, J. Non-Cryst. Solids **338-340** (2004) 1 - 12.

[65] S. R. Jadkar, J. V. Sali, S. T. Kshirsagar and M. G. Takwale, J. Non-Cryst. Solids **299 - 302** (2002) 168 - 173.

[66] A.H.M. Smets, W.M.M. Kessels, and M.C.M. van de Sanden, Appl. Phys. Lett. **82** (2003) 1547 -1549.

[67] B. Pantchev, P. Danesh, B. Schmidt, Appl. Phys. Lett. **87** (2005) 023104.

[68] S. Gupta, G. Morell, and B.R. Weiner, J. Non-Cryst. Solids **343** (2004) 131 - 142.

[69] N.M. Hwang, J.H. Hahn, and D.Y. Yoon, Journal of Crystal Growth **162** (1996) 55 - 68.

[70] B.G. Yacobi, R.W. Collins, G. Moddel, P. Viktorovitch, and W. Paul, Phys. Rev. B **24** (1981) 5907 - 5912.

[71] J.C. Knights, J. Non-Cryst. Solids **35 - 36** (1980) 159 -170.

[72] W. E. Spear and M. Heintze, Philos. Mag B **54** (1986) 343 - 358.

[73] Y. Hishikawa, J. Appl. Phys. **62** (1987) 3150 - 3155.

[74] F.C. Marques, P. Wickboldt, D. Pang, J.H. Chen, and W. Paul, J Appl.Phys. **84** (1998) 3118 - 3124.

[75] N.F. Mott, F. R.N. Nabarro, Proc. Phys. Soc. **52** (1940) 86 - 89.

[76] P.Wickboldt, S.J. Jones, F.C. Marques, D. Pang, W.A. Turner, A.E. Wetsel, W. Paul, and J.H. Chen, Philos. Mag. B **64** (1991) 655 - 674.

[77] S. Nonomura, N. Yoshida, T. Gotoh, T. Sakamoto, M. Kondo, A. Matsuda, and S.Nitta, J. Non-Cryst. Solids **266 - 269** (2000) 474 - 480.

[78] D.L. Staebler and C.R. Wronski, Appl. Phys. Lett. **31** (1977) 292 - 294.

[79] S. Yamasaki and J. Isoya, J. Non-Cryst. Solids **164-166** (1993) 169 - 174.

[80] H.M. Branz, Phys. Rev. B. **59** (1999) 5498 - 5512.

[81] H.M. Branz, J. Non-Cryst. Solids **266 - 269** (2000) 391 - 396.

[82] G. Lucovsky, R.J. Nemanich, and J.C. Knights, Phys. Rev. B **19** (1979) 2064 - 2073.

[83] L.G. Jacobsohn, R.K. Schulze, L.L. Daemen, I.V. Afanasyev-Charkin and M. Nastasi, Thin Solid Films **494** (2006) 219 - 222.

[84] A. L. B. Neto, T. Dylla, S. Klein, T. Repmann, A. Lambertz, R. Carius and F. Finger, J. Non-Cryst. Solids **338 - 340** (2004) 168 - 172.

[85] Y. Wu, J.T. Stephen, D.X. Han, J.M. Rutland, R.S. Crandall, and A.H. Mahan, Phys. Rev. Lett.**77** (1996) 2049 - 2052.

[86] P. Tzanetakis, Sol. Energy Mater. Sol. Cells **78** (2003) 369 - 389.

[87] T. Sakamoto, N. Yoshida, H. Harada, T. Kishida, S. Nonomura, T. Gotoh, M. Kondo, A. Matsuda, T. Itoh, and S. Nitta, J. Non-Cryst. Solids **266 - 269** (2000) 481 - 485.

[88] H.Y.Hao, G.L.Kong, X.B. Zeng, Y. Xu, H.W. Diao, X.B.Liao, Acta Phys. Sinica **54** (2005) 3327 - 3331.

[89] P.A.T.T. van Veenendaal, R.E.I. Schropp, Curr. Opinion in Sol. State and Mater. Sci. **6** (2002) 465 - 470.

[90] G. Munyeme, J-P.R. Wells, L.F.G. van der Meer, J.I. Dijkhuis, W.F. van der Weg, and R.E.I. Schropp, J. Non-Cryst. Solids **338 - 340** (2004) 291 - 294.

[91] L.D. Landau and E.M. Lifshitz, *Course of Theoretical Physics: Vol 7 Theory of Elasticity*, Pergamon Press, Oxford, UK (1970).

[92] I.C. Noyan and J.B. Cohen, *Residual Stress Analysis*, Springer-Verlag, New York, USA (1987).

[93] V. Hauk (Ed.), *Structural and Residual Stress Analysis by Nondestructive Methods,* Elsevier, Amsterdam, The Netherlands (1997).

[94] D.S. Kim and B.C. Lee, Int. J. Sol. Struct. **31** (1994) 1225 -1240.

[95] Y.C Tsui and T.W. Clyne, Thin Solids Films **306** (1997) 23 - 33.

[96] S. Mukherjee, F. Prokert, E. Richter and W. Moeller, Surf. and Coat. Technol. **186** (2004) 99 - 103.

[97] M. Chinmulgund, R. B. Inturi and J. A. Barnard, Thin Solid Films **270** (1995) 260 - 263

[98] O. Kesler, J. Matejicek, S. Sampath, S. Suresh, T. Gnaeupel-Herold, P. C. Brand and H. J. Prask, Mater. Sci. and Eng. A **257** (1998) 215 - 224.

[99] V. Ramaswamy, W. D. Nix and B. M. Clemens, Scripta Mater. **50** (2004) 711 - 715

[100] V.M. Koleshko, V.F. Belitsky and I.V. Kiryushin, Thin Solid Films **162** (1988) 365 - 374.

[101] W. Ruihua, L. Zhiqiang, L. Li, and L. Jahe, Sol. Energy Mater. Sol. Cells **62** (2000) 193 - 199.

[102] K.F.Feenstra, R.E.I. Schropp, and W.F. Van der Weg, J. Appl.Phys. **85** (1999) 6843 - 6852.

[103] S. R. Jadkar, J. V. Sali, S. T. Kshirsagar and M. G. Takwale, Sol. Energy Mater. Sol. Cells **85** (2005) 301 - 312.

[104] A. Gallagher, Thin Solid Films **395** (2001) 25 - 28.

[105] M. Konagai, T. Tsushima, M.K. Kim, K. Asakusa, A. Yamada, Y. Kudriavtsev, A. Villegas, R. Asomoza, Thin Solid Films **395,** (2001) 152-156

[106] D.T. Britton, Z. Sigcau, C.M. Comrie, D.F. Kanguwe, E. Minani, D. Knoesen, and M. Härting, Thin Solid Films **430** (2003) 149 - 152.

[107] E. Spanakis, E Stratakis, P. Tzanetakis, and Q. Wang, J. Appl. Phys. **89** (2001) 4294 - 4300.

[108] R.W. James, *Optical Principles of the Diffraction of X-rays*, G. Bell & Sons, London, UK (1948).

[109] H.P. Klug and L.E. Alexander, *X-ray Diffraction Procedures: for Polycrystalline and Amorphous Materials*, 2nd Edition, John Wiley & Sons, New York, USA (1974).

[110] B. D. Cullity, *Elements of X-ray Diffraction*, Addson-Wesley, London, UK (1978).

[111] F. Zernike and J.A. Prins, Z. Phys. **41** (1927) 184 - 194.

[112] B.E. Warren, J. Appl. Phys. **8** (1937) 645 - 654.

[113] E. Minani, Z. Sigcau, O. Adegbite, F.L. Ramukosi, T.P. Ntsoane, S. Harindintwari D. Knoesen, C.M. Comrie, D.T. Britton, and M. Härting, Thin Solid Films **501** (2006) 84 - 87.

[114] C. E. Benz and G.W. Stewart, Phys. Rev. **46** (1934) 703 - 706.

[115] G.G. Harvey, Phys. Rev. **46** (1934) 441 - 445.

[116] R. Spangler, Phys. Rev. **46** (1934) 698 - 703.

[117] A. Einstein and N.S. Gingrich, Phys. Rev. **62** (1942) 261 - 270.

[118] A.J. Walton, *Three Phases of Matter*, Clarendon Press, Oxford, UK (1983).

[119] M. Härting, S. Woodford, D. Knoesen, R. Bucher, and D. T. Britton, Thin Solid Films **430** (2003) 153 - 156.

[120] I Halevy, E. Üstündag, S.Salhov, A.F. Yue, A. Broide, and J. Hu, Z. Kristallogr. **219** (2004) 166 - 171.

[121] H.F. Poulsen, J.A. Wert, J. Neuefeind, V. Honkimäki, and M. Daymond, Nature Mater. **4** (2005) 33 - 36.

[122] M. Härting, D.T. Britton, E. Minani, T.P. Ntsoane, M. Topic, T. Thovhogi, O.M. Osiele, D. Knoesen, S. Harindintwari, F. Furlan, and C. Giles, Thin Solid Films **501** (2006) 75 - 78.

[123] C. Genzel, Mater. Sci. Technol. **21** (2005) 10 - 18.

[124] H. Dolle, J. Appl. Cryst. **12** (1979) 489 - 501.

[125] F.F. Ferreira, E. Granado, W. Calvalho Jr., S.W. Kycia, D. Bruno, and R. Droppa Jr., J. Synchrotron Rad. **13** (2006) 46 - 53.

[126] C. Giles, F. Yokaichiya, S.W. Kycia, L.C. Sampaio, D.C. Ardiles-Saravia, M.K.K. Franco, and R. T. Neuenschwander, J. Synchrotron Rad. **10** (2003) 430 - 434.

[127] *International Tables for X-ray Crystallography*, Kluwer Academic Publishers, Dordrecht, The Netherlands (1989).

[128] M. Härting and P. Willutzki, Meas. Sci. Technol. **6** (1995) 276 - 280.

[129] M. Härting, Acta Mater. **46** (1998) 1427 - 1436.

[130] M. Härting, S. Nsengiyumva, A.T. Raji G. Dollinger P. Sperr S.R. Naidoo, T.E. Derry, C.M. Comrie, and D.T. Britton., Surf, and Coat. Technol. **201** (2007) 8237 - 8241.

[131] J.P. Conde, P. Alpuim, M. Boucinha, J. Gaspar, V. Chu, Thin Solid Films **395**(2001)105-111.

[132] D.Han, J. Baugh, and G. Yue, Q. Wang, Phy. Rev. B62 (2000)7169-7178

[133] http://bouman.chem.georgetown.edu/S00/handout/spectrometer.gif, accessed 2007/12/31.

[134] C.N. Banwell and E.M. McCash, *Fundamental of Molecular Spectroscopy* (4th edition), McGraw-Hill, London, UK (1994).

[135] R. Swanepoel, J. Phys. E: Sci. Instr. **16** (1983) 1214 - 1222.

[136] R. Swanepoel, J. Phys. E: Sci. Instr. **17** (1984) 896 - 903.

[137] J.C. Manifacier, J. Gasiot, and J.P. Fillard, J. Phys. E: Sci. Instr. **9** (1976) 1002 -1004.

[138] S. Halindintwali, *A study of Hydrogenated Nanocrystalline Silicon Thin Films Deposited by Hot wire Chemical Vapour Deposition*, PhD Thesis, University of Western Cape, South Africa (2005).

[139] R.H. Klazes, M.H.L.M. van den Broek, J. Bezemer, and S. Radelaar, Philos. Mag. B **45**, (1982) 377 - 383.

[140] R.A. Street, Phys. Rev. **B** 44 (1991) 10610 - 10616.

[141] A.J.M. Berntsen, W.F. van der Weg, P.A. Stolk, and F.W. Saris, Phys. Rev. **B48** (1993) 14656 - 14658.

[142] E. Pincik, H. Kobayashi, J. Mullerova, K.Gmucova, M.Jergel, R Brunner, M. Zeman, M. Zahoran, Acta Phys. Slovaca **53** (1992) 13367 - 13377.

[143] C.N. Banwell and E.M. McCash, *Fundamental of molecular spectroscopy,* Fourth edition, Mc Graw Hill (1994)

[144] W. Schroter, *Material Science and Technology: A comprehensive Treatment, vol.4: Eelectronic Structure and Properties of Semiconductors*, Wiley, New York, USA (1991).

[145] A.H. Mahan, P. Raboisson, R. Tsu, Appl.Phys.Lett. **50**, (1987) 335.

[146] A.H. Mahan, P. Menna, R. Tsu, Appl.Phys.Lett. **51**, (1987) 1167.

[147] E. Bhattacharya and A.H. Mahan, Appl.Phys.Lett. **52**, (1988) 1587.

[148] A.A. Langford, M.L. Fleet, B.P. Nelson, W.A. Lanford, and N. Maley, Phys. Rev. B **45** (1992) 13367 - 13377.

[149] J.D. Ouwens and R. E. I. Schropp, Phys. Rev. B **54** (1996) 17759 - 17762.

[150] M.H. Brodsky, M. Cardona, and J.J. Cuomo, Phys. Rev. B **16** (1977) 3556 - 3571.

[151] N. Maley, Phys. Rev. B **46** (1992) 2078 - 2085.

[152] J. L'Ecuyer, C. Brassard, C. Cardinal, J. Chabbal, L. Deschênes, J.P.Labrie, B. Terreault, J. G. Martel and R.St. Jacques, J. Appl. Phys. **47** (1976) 381 - 382.

[153] L.C. Feldman and J.W. Mayer, *Fundamentals of Surface and Thin Film Analysis*, North Holland, Amsterdam, The Netherlands (1986).

[154] R. Biswas, I. Kwon, and C.M. Soukoulis, Phys. Rev. B **44** (1991) 3403-3406.

[155] C Longeaud, J. Optoelectr. Adv. Mater. **4** (2002) 461 - 479.

[156] D.T. Britton, E. Minani , D. Knoesen , H. Schut , S.W.H. Eijt, F. Furlan , C. Giles, and M. Härting, Appl. Surf. Sci. **252** (2006) 3194 - 3200.

APPENDIX: **Sin$^2\psi$ plots in reciprocal and real space for as deposited samples and after illumination**

Strain variation in reciprocal space

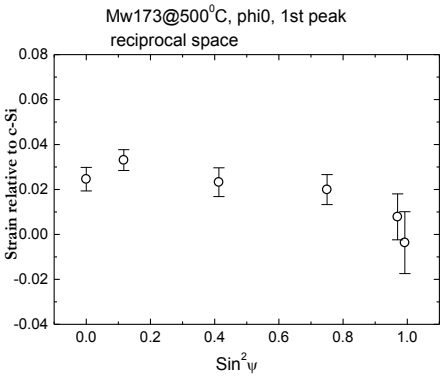

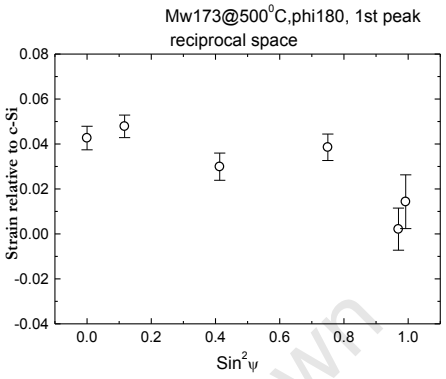

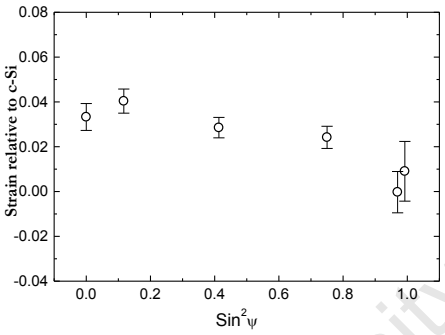

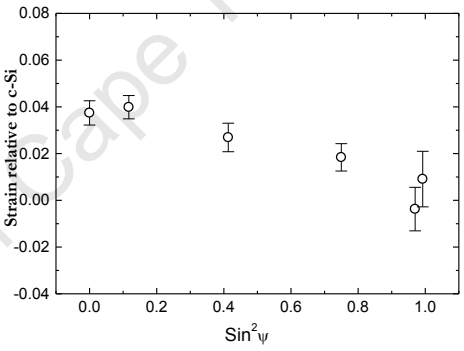

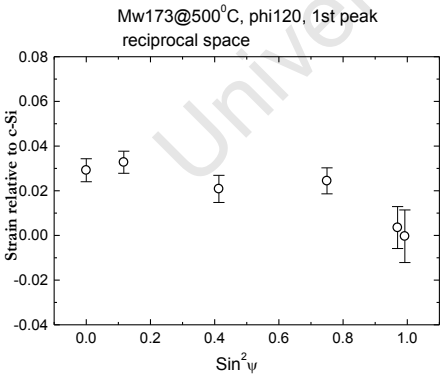

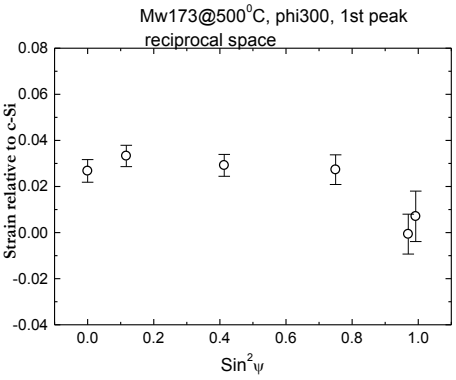

Strain variation in reciprocal space

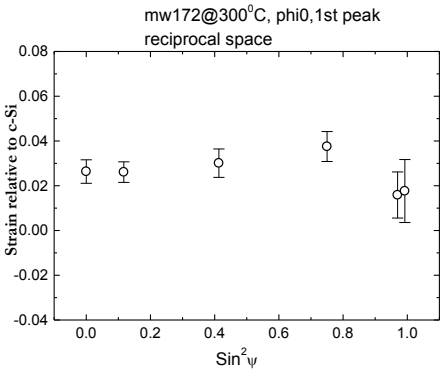

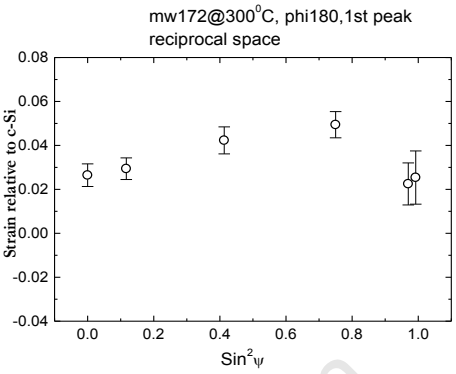

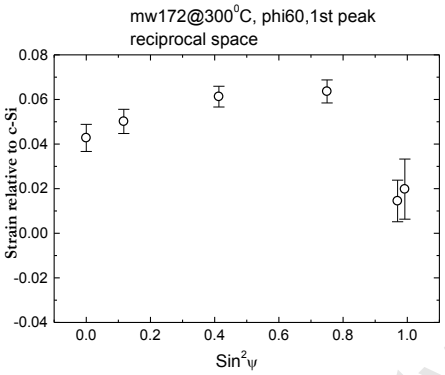

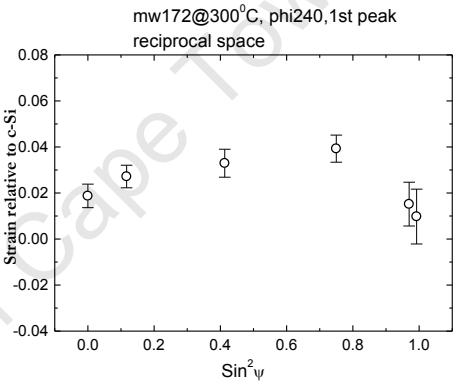

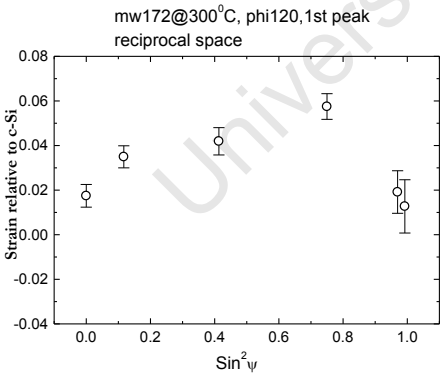

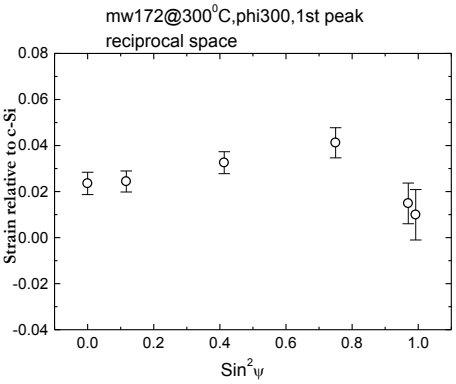

Strain variation in reciprocal space

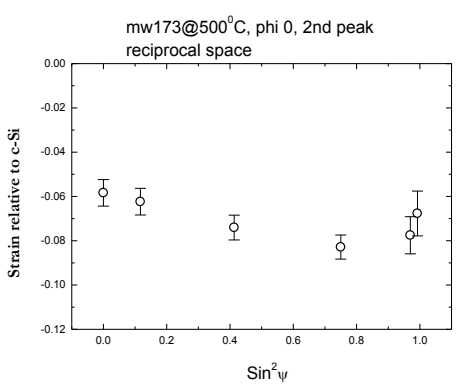

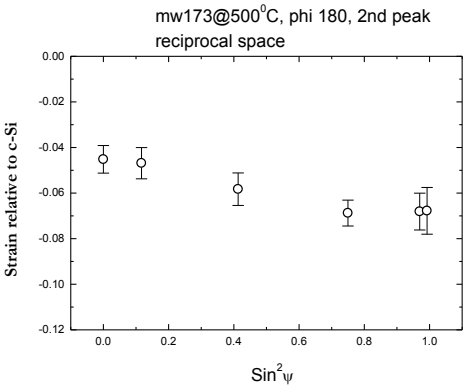

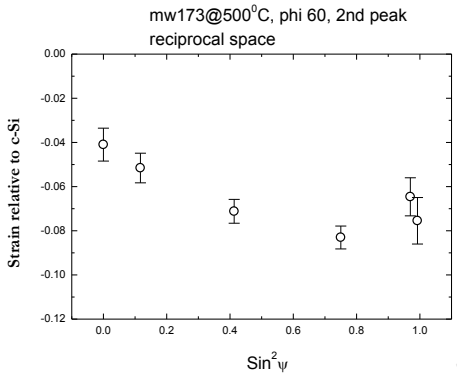

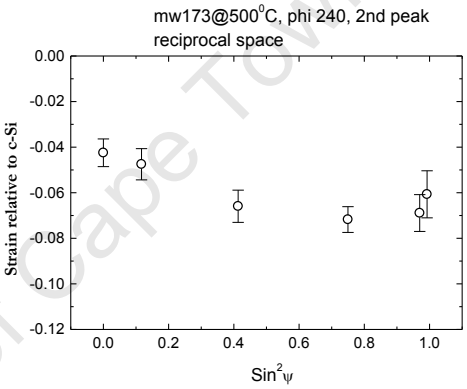

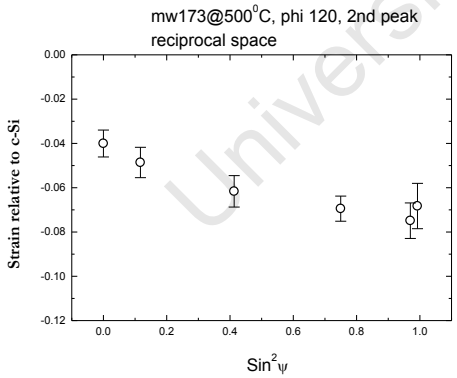

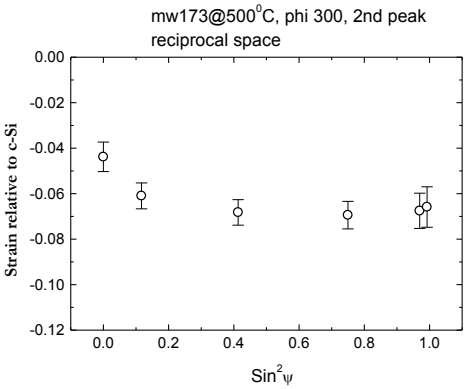

Strain variation in reciprocal space

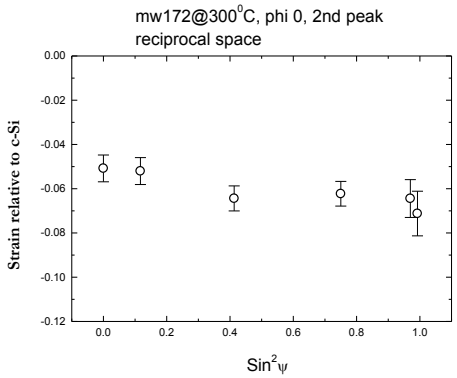

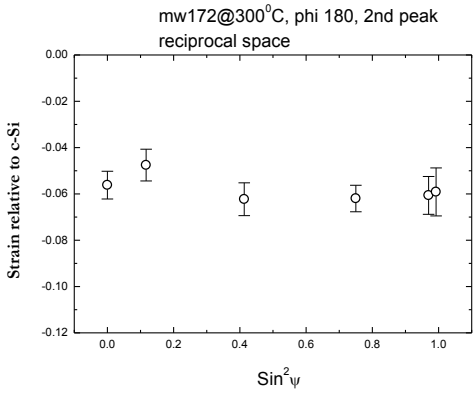

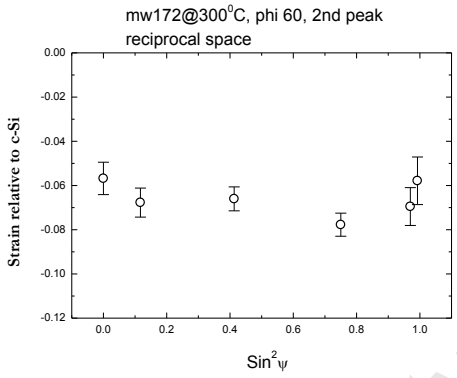

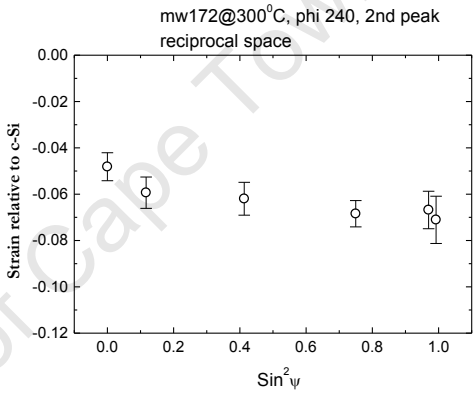

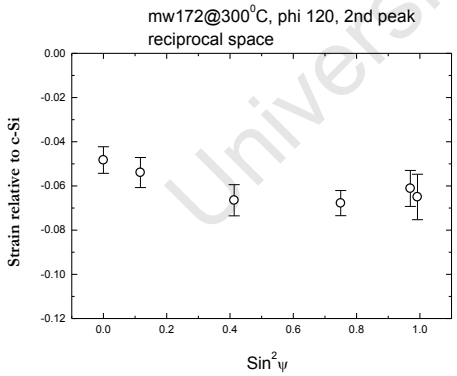

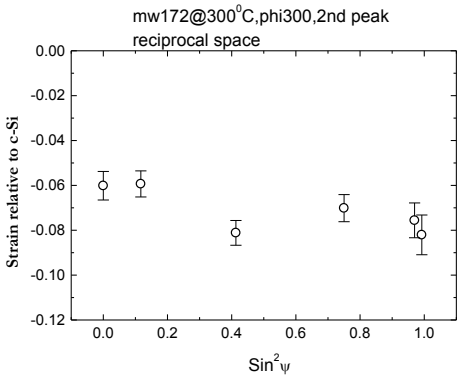

Strain variation in reciprocal space

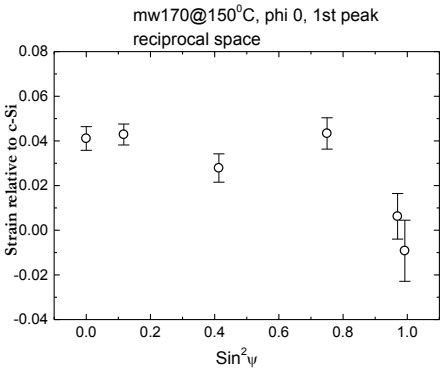

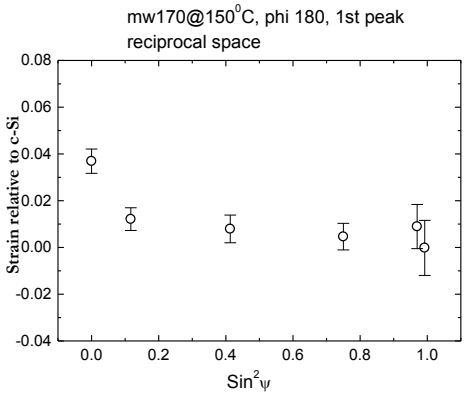

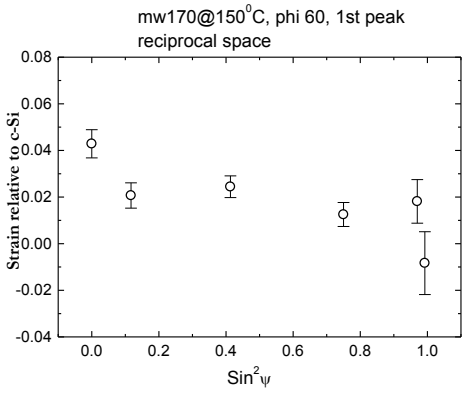

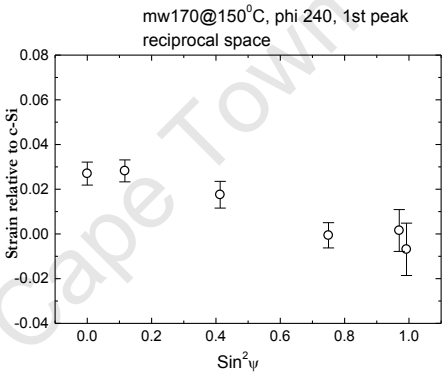

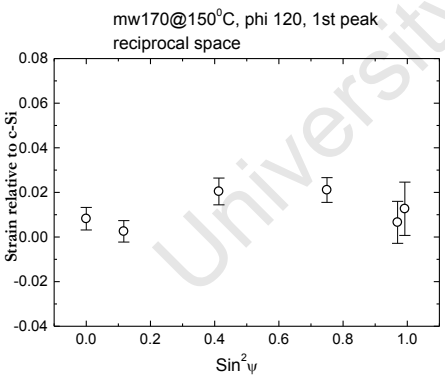

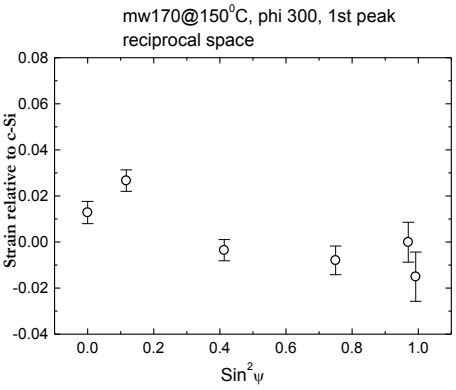

Strain variation in reciprocal space

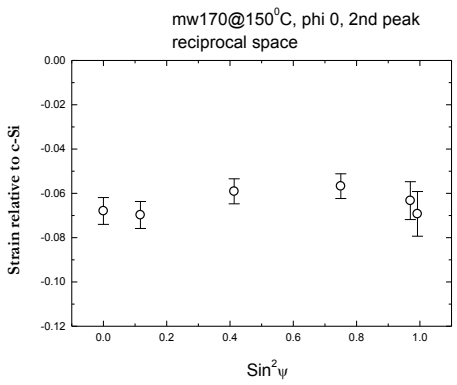

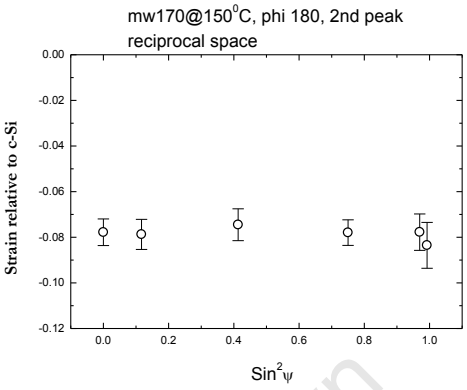

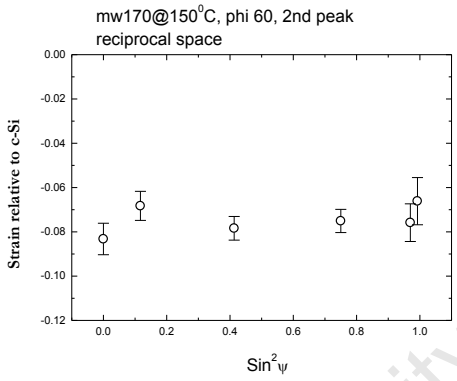

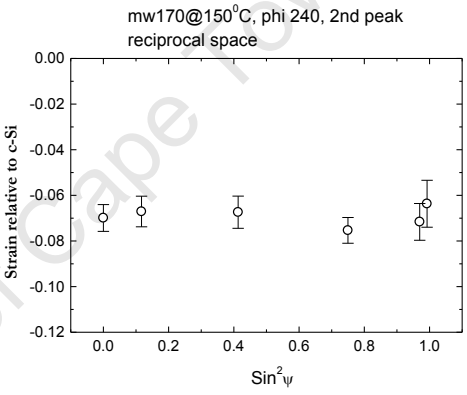

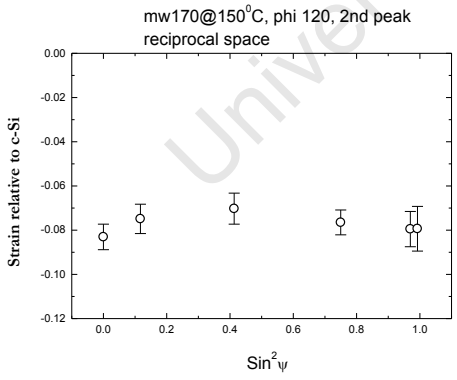

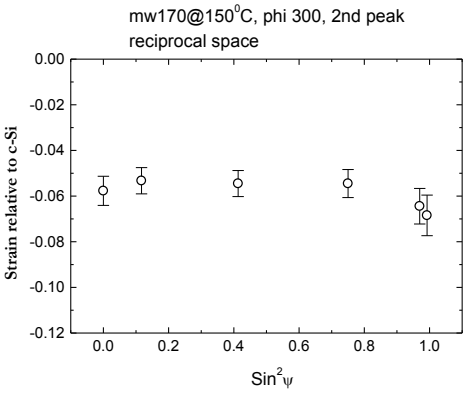

Strain variation in reciprocal space after 12 hours illumination

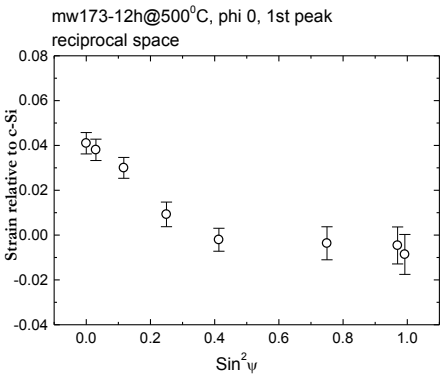

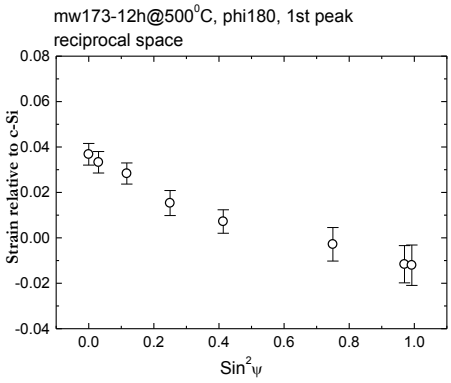

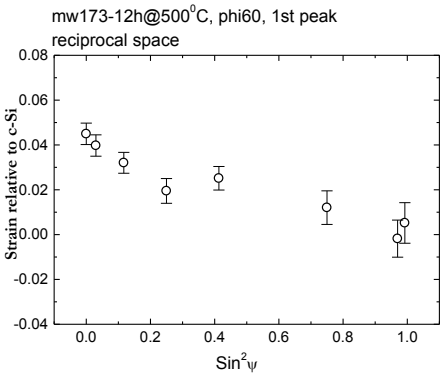

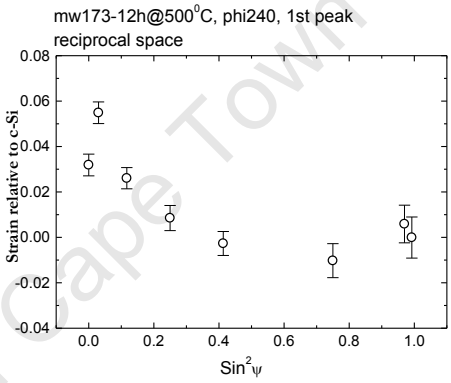

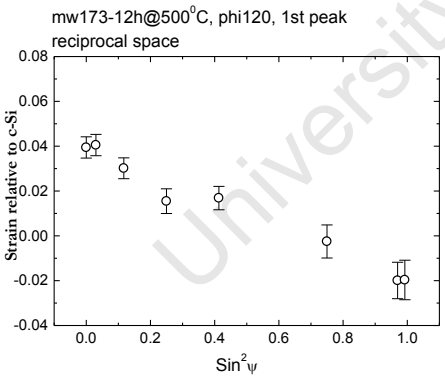

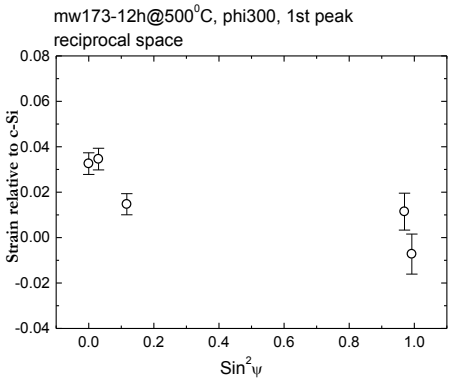

Strain variation in reciprocal space after 12 hours illumination

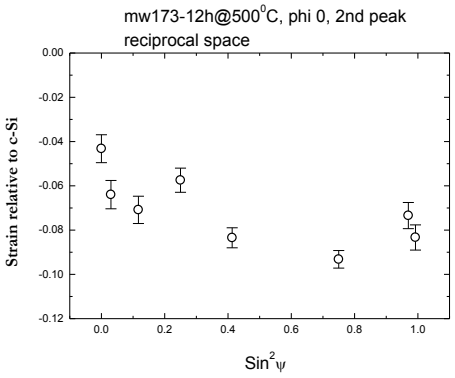

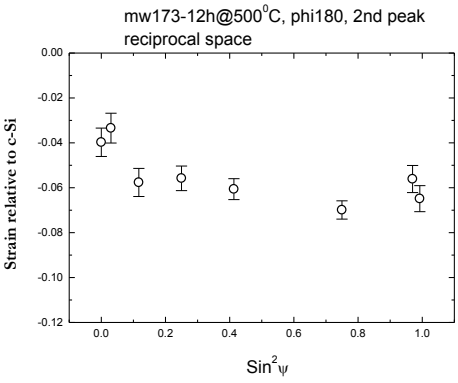

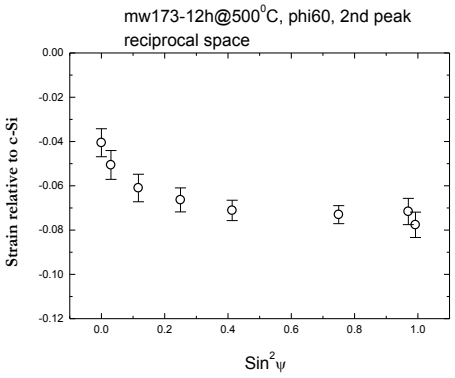

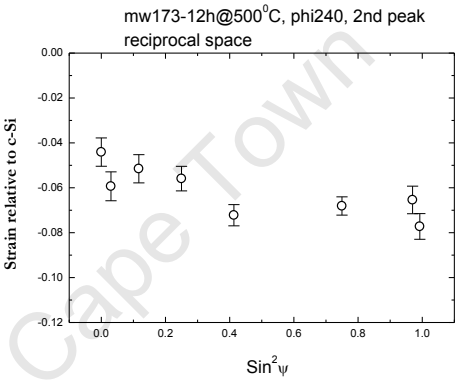

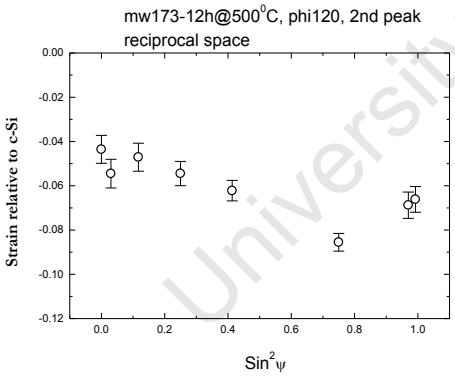

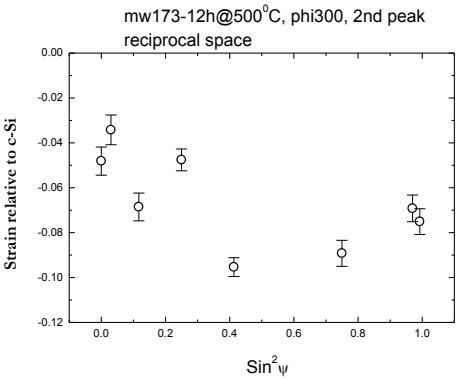

Strain variation in reciprocal space after 48 hours illumination

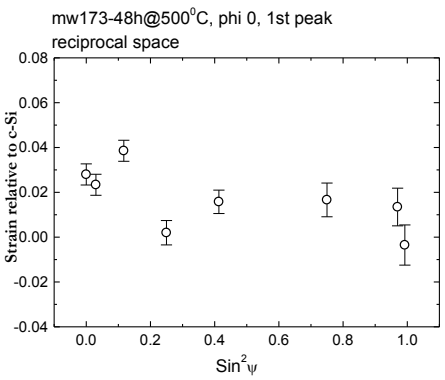

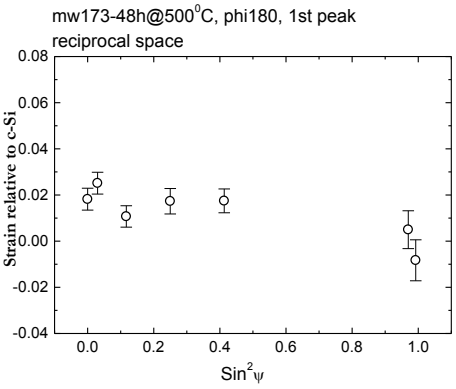

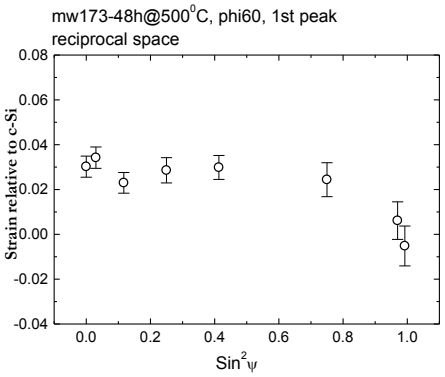

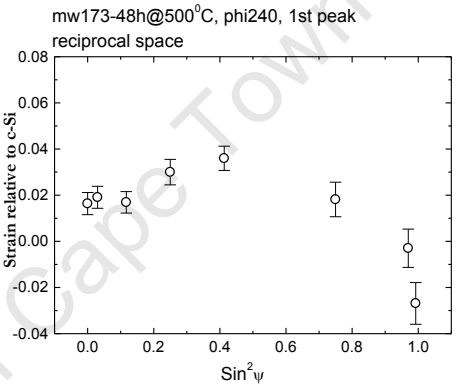

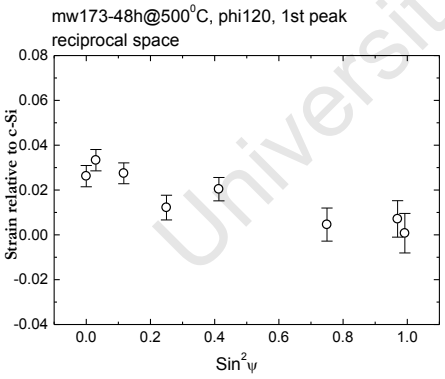

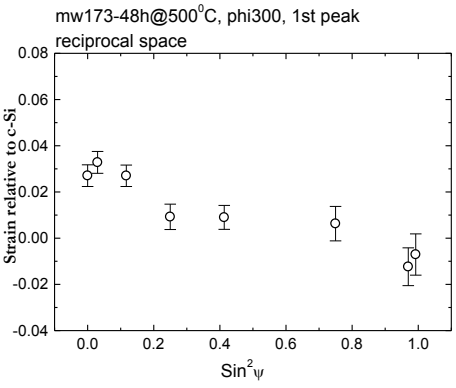

Strain variation, in reciprocal space, after 48 hours illumination

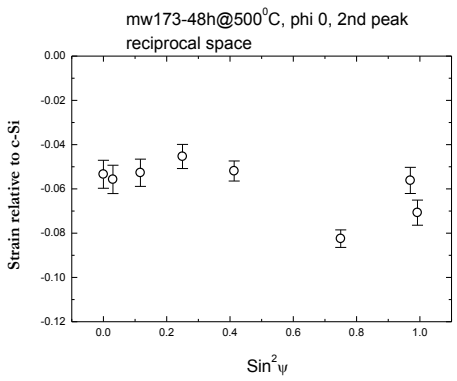

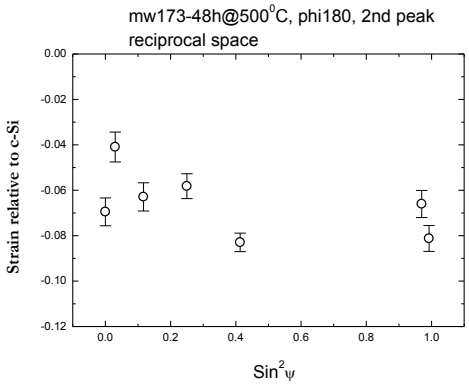

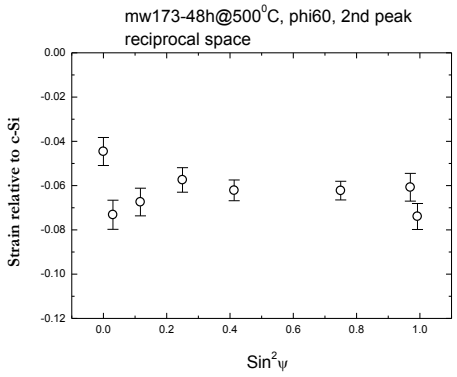

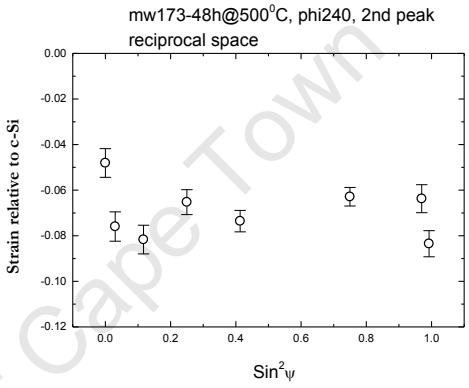

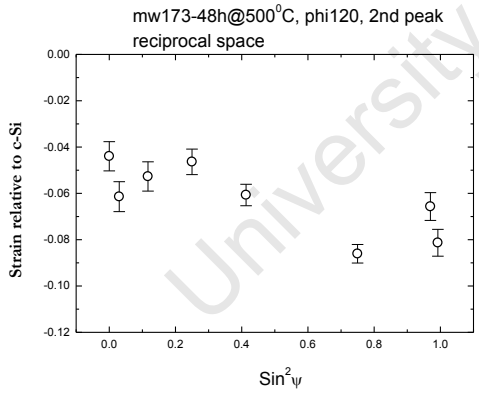

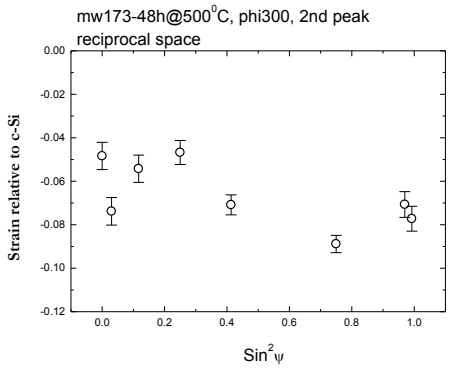

Strain variation, in reciprocal space, after 12 hours illumination

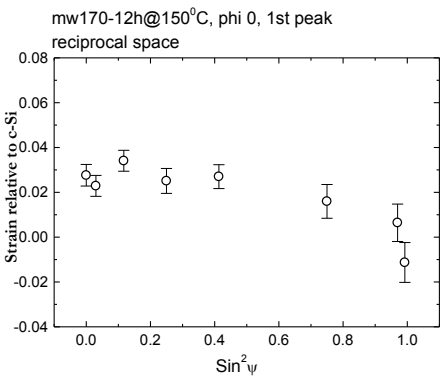

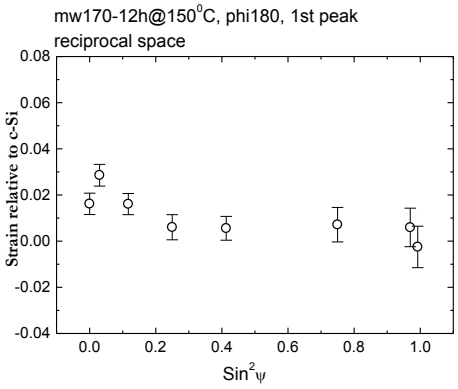

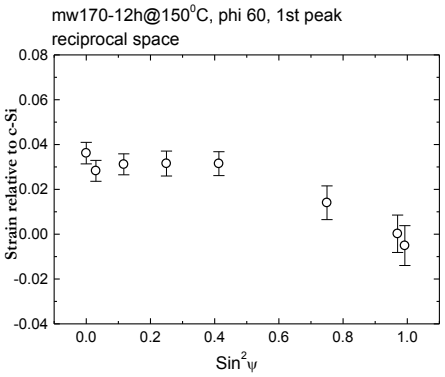

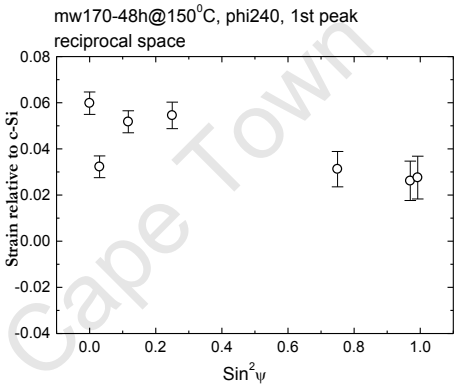

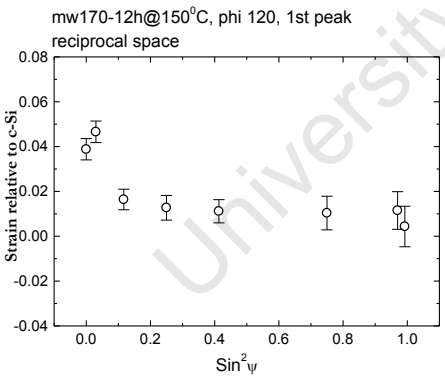

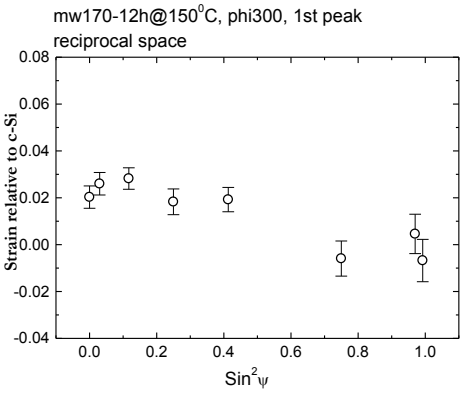

Strain variation, in reciprocal space, after 48 hours illumination

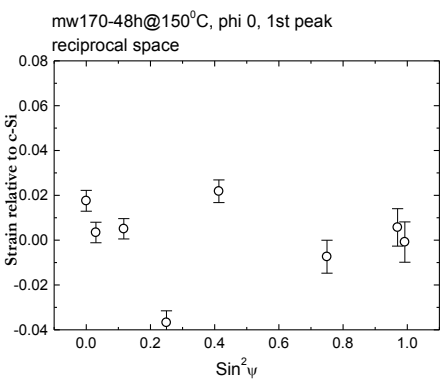

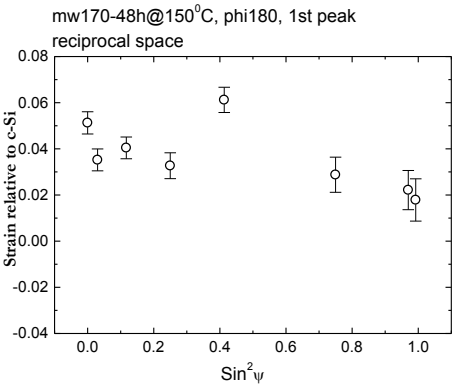

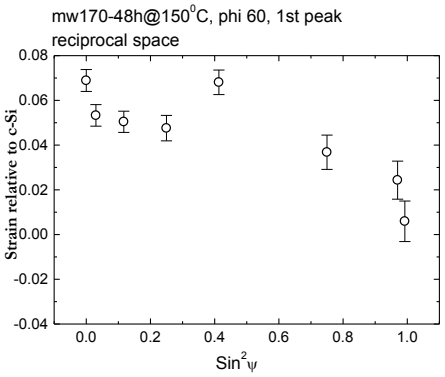

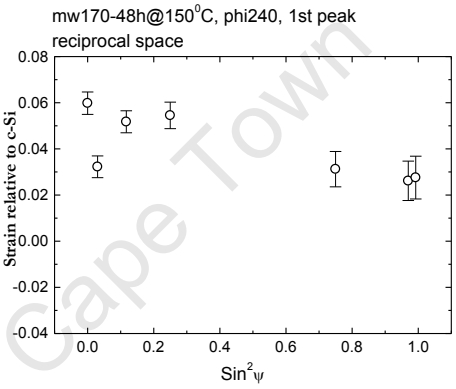

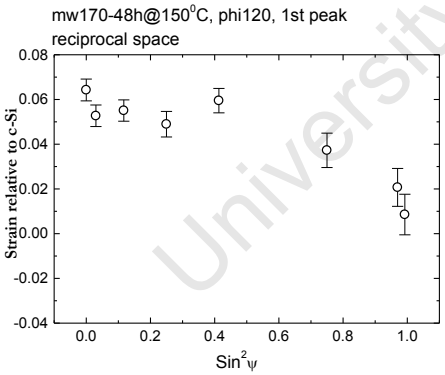

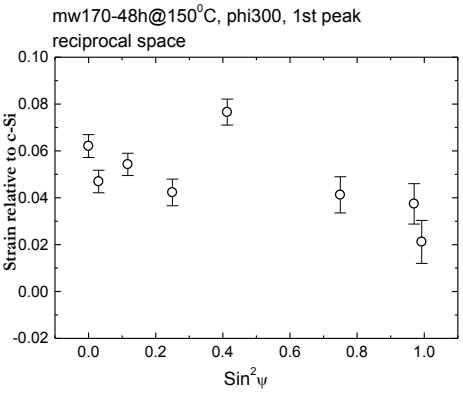

Strain variation, in reciprocal space, after 12 hours illumination

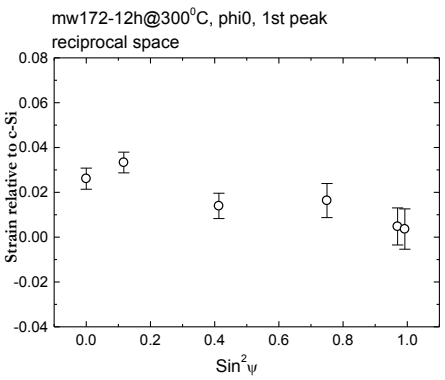

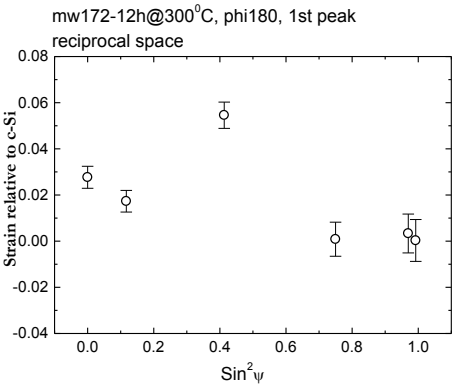

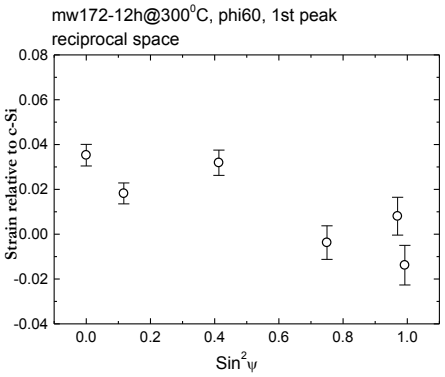

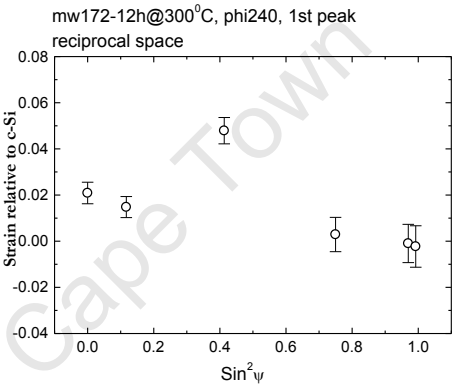

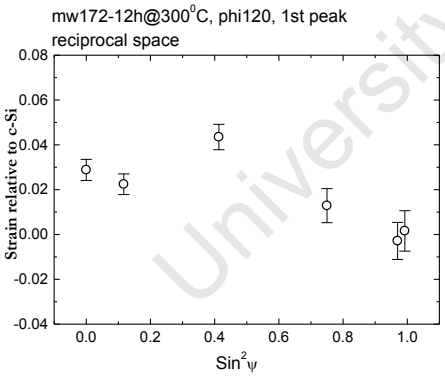

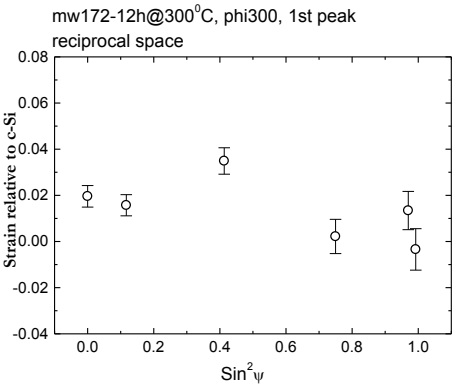

Strain variation, in reciprocal space, after 48 hours illumination

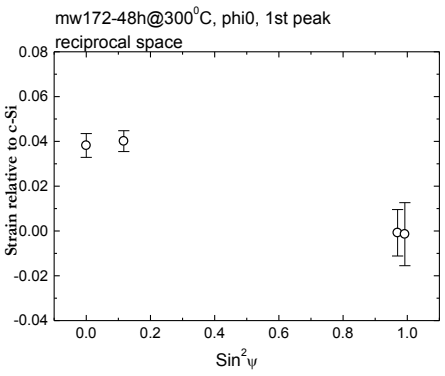

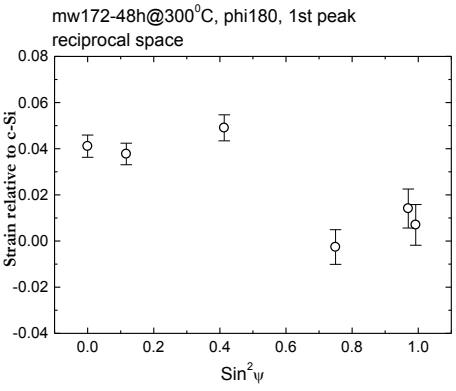

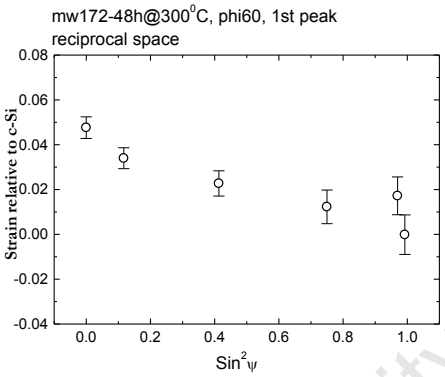

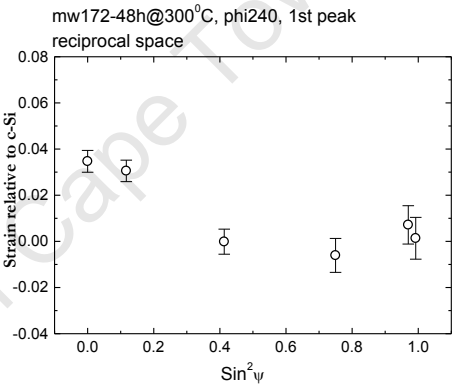

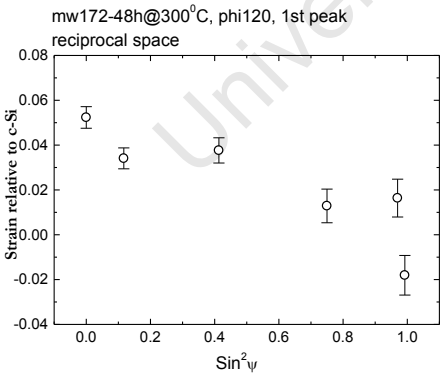

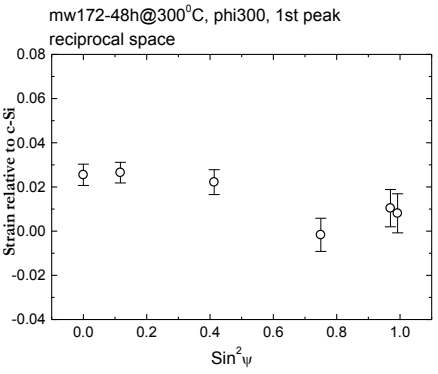

Strain variation, in reciprocal space, after 12 hours illumination

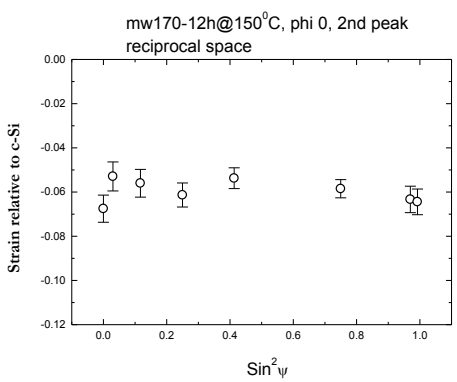

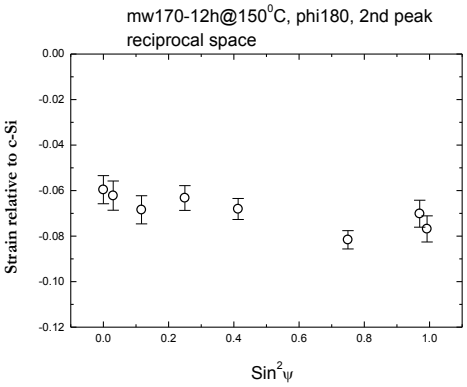

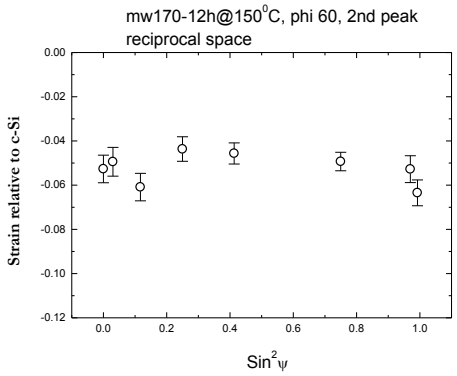

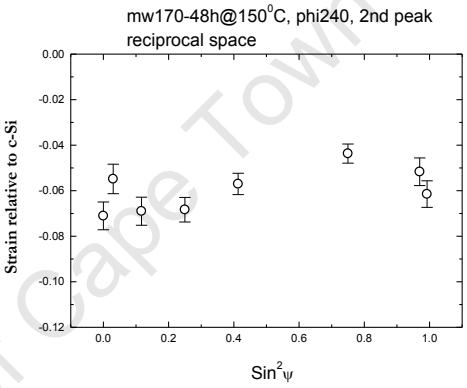

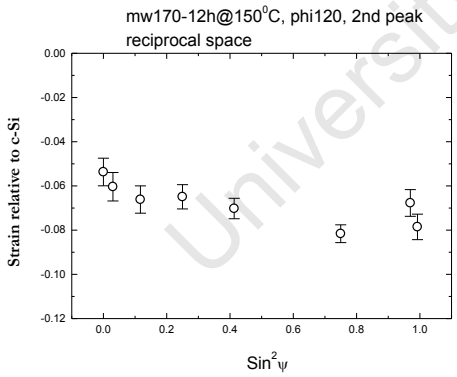

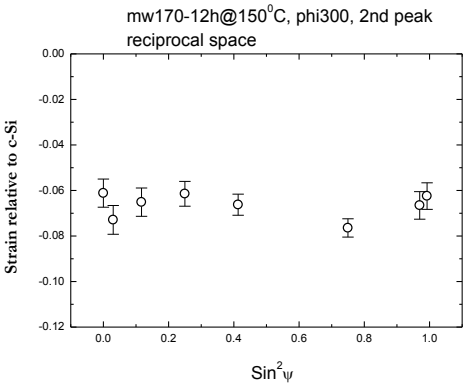

Strain variation, in reciprocal space, after 48 hours illumination

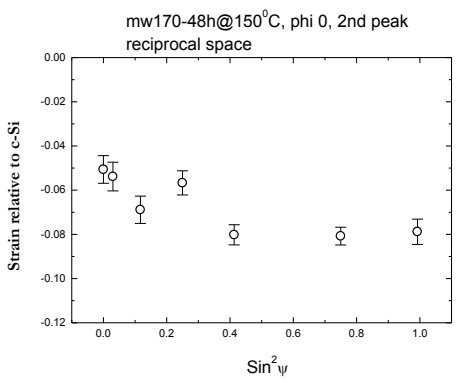

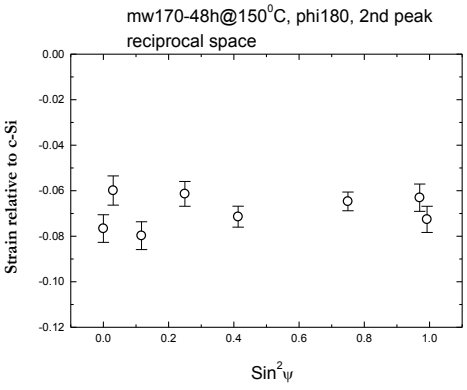

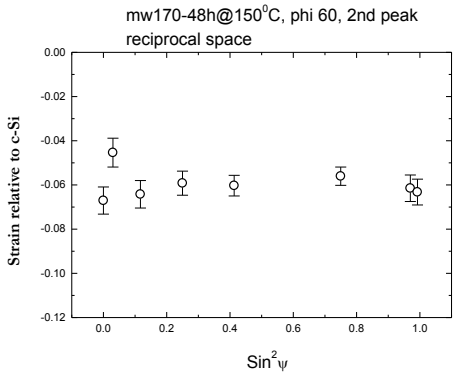

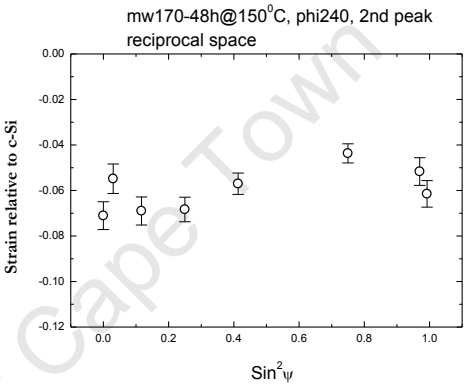

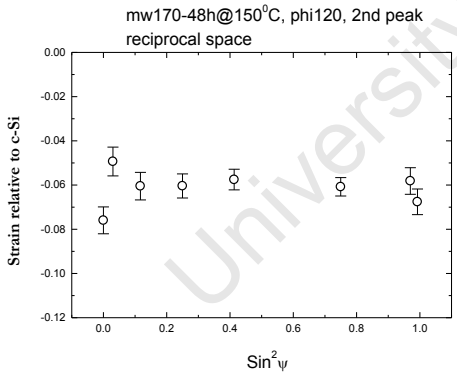

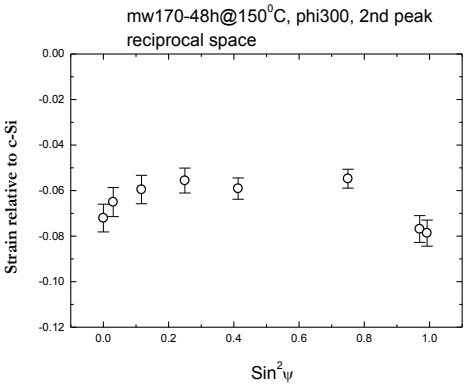

Strain variation, in reciprocal space, after 12 hours illumination

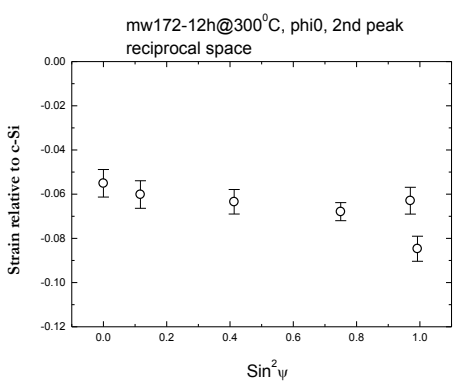

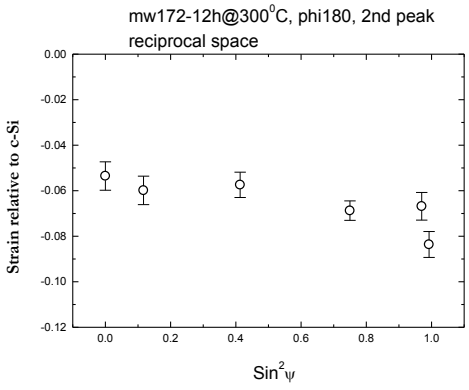

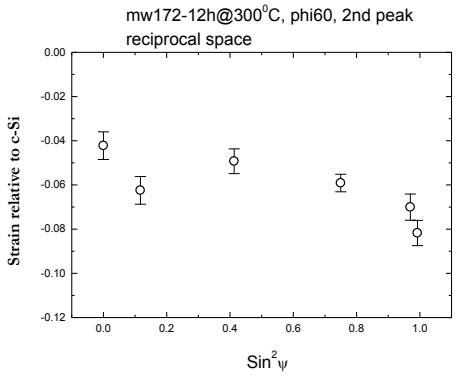

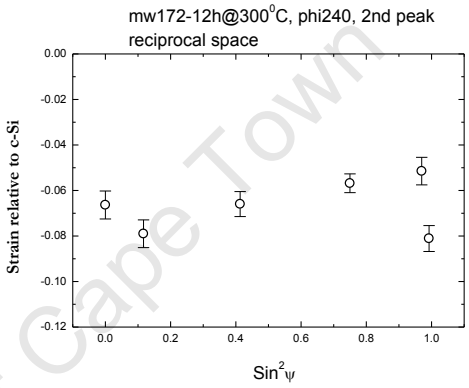

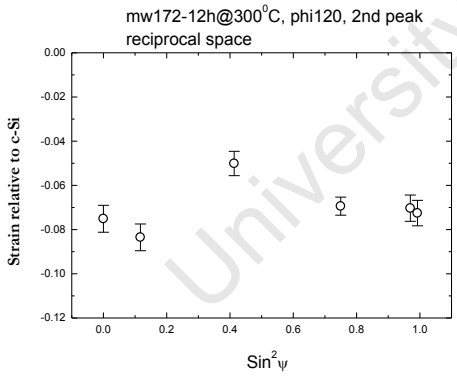

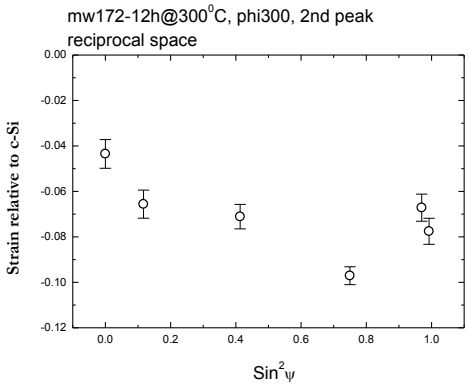

x

Strain variation, in reciprocal space, after 48 hours illumination